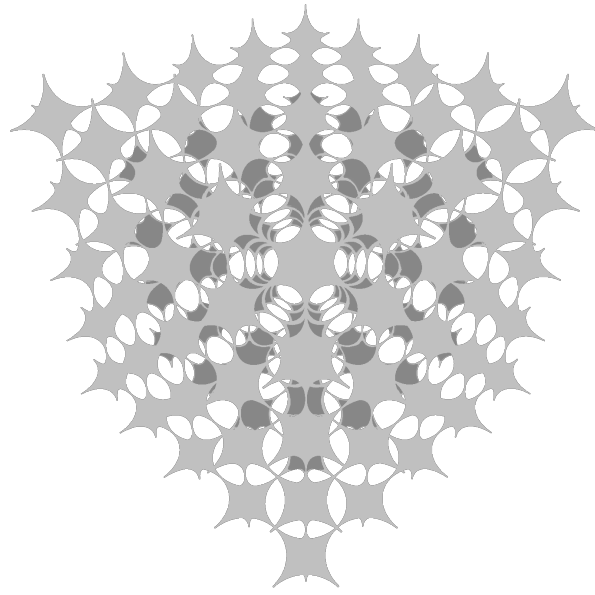


IMPERIAL COLLEGE LONDON

Department of Earth Science and Engineering

Centre for Petroleum Studies



**Directional measures to characterize anisotropy
in pore-scale morphology and permeability**

By

Lukas Mosser

**A report submitted in partial fulfillment of the requirements for
the MSc and/or the DIC**

September 2016

DECLARATION OF OWN WORK

I declare that this thesis

“Directional measures to characterize anisotropy
in pore-scale morphology and permeability.”

is entirely my own work and that where any material could be construed as the work of others, it is fully cited and referenced, and/or with appropriate acknowledgment given.

Signature:

Name of student:

Name of supervisor:

Acknowledgment

I would first like to thank my thesis advisors Professor Olivier Dubrule and Professor Martin J. Blunt of the Department of Earth Science and Engineering, Imperial College London. Their constructive comments, enthusiasm, and knowledge, have greatly inspired this work.

I would also like to acknowledge Dr. Branko Bijeljic and Dr. Ali Qasiminejad Raeini of the Department of Earth Science and Engineering for their support and for sharing their deep technical understanding with me.

To my friends at Imperial College London MSc. 2015/16 for the laughter and the many unforgettable moments we share.

I would like to express my deepest gratitude to Andrea who has supported me throughout the last two years and encouraged me to believe in myself and to persevere in challenging times.

Finally, I would like to express my profound gratitude to my parents Ursula and Jakob and my sister Sophie, who have always believed in me and who have supported me all throughout my education in good and in bad times. Without you, this would not have been possible.

“Nullius in Verba”

Abstract

The ability of fluids to flow through sedimentary rocks is a critical component in the process of recovering oil and gas from subsurface hydrocarbon accumulations. The formation of hydrocarbon bearing reservoirs is attributed to the deposition of siliciclastic grains or carbonate components followed by burial and diagenesis. Their ability to transport fluids is a function of these depositional environments and can be described on a variety of length scales. At the pore-scale, modern solvers for the (Navier-) Stokes equations allow evaluating intrinsic permeability on segmented high-resolution Micro-CT images of individual samples. To integrate pore-scale information in core, sector or field scale studies, upscaling of pore-scale permeability is necessary. Knowledge about the existence of anisotropy in pore-scale flow properties can have critical implications on effective recovery strategies of oil and gas reservoirs.

This thesis aims to evaluate existing anisotropy at the pore-scale by applying directional measures of statistical variation and pore space morphology. High-resolution Micro-CT data of sedimentary sandstone and carbonate samples have been used in an integrated workflow to evaluate directional variation of pore space morphology and the relation to directional single-phase flow properties.

The covariance was estimated directionally to investigate the possible existence of variation in representative elementary volume (REV) size and pore geometry. We introduce a tensorial extension of Minkowski functionals allowing evaluation of orientational characteristics in the grain-void interface. These directional measures are shown to be physically well-defined and are directly related to the seminal work of Kozeny (1927) and Carman (1937, 1939). A number of simple geometric models are used to illustrate the characteristics of these tensorial measures. By extracting triangulated representations of the pore-grain interface, we are able to evaluate tensorial Minkowski functionals for binary Micro-CT images of sedimentary rock.

Our results indicate that directional estimates of the covariance can be used to assess pore-scale variation such as periodicity indicating the possible existence of stratification and gain information about the existence of REVs of different size in different directions. Directional estimates of the characteristic pore and mean grain size allow a qualitative estimate of the principal directions of flow. Evaluation of the anisotropy in surface orientation in the available Micro-CT images using Minkowski tensors allows evaluation of the REV and variation in surface orientation. By comparing numerical estimates of permeability and applying the theory of Bear and Bachmat (1986, 1990) we obtain directional estimates of the tortuosity factors for a variety of siliciclastic and carbonate samples. Our findings show that Minkowski tensors present a sensitive measure of anisotropy in pore morphology and can be applied to gain qualitative information on the existence of anisotropy at the pore-scale as well as the preferred directions of flow.

Table of Contents

Abstract	1
Introduction	1
Literature review.....	2
Methodology.....	3
Micro-CT images and pre-processing.....	3
Covariance	4
Scalar and tensorial Minkowski functionals	5
Anisotropic parametric models as pore-grain analogs	6
Estimation of directional permeability.....	7
Results.....	8
Integrated computational workflow	9
Covariance estimation.....	9
Minkowski tensors as measures of pore space anisotropy	10
Single-phase flow properties.....	11
Prediction of single-phase permeability from directional covariance	11
Minkowski tensors as qualitative indicators of directional permeability	12
Discussion	13
Conclusions	14
Nomenclature.....	14
References	15
Appendices	17
Appendix 1A: Milestones	17
Appendix 1B: Summaries of key milestone publications	18
Appendix 2: Workflow description.....	26
Appendix 3: Parametric pore space modeling.....	27
Appendix 4: Interface extraction from binary Micro-CT images	30
Appendix 5: Reproducibility and software documentation.....	31
Appendix 6: Sample results and analysis.....	32

List of Figures

Figure 1: Comparison of the covariance for hard-sphere and overlapping-sphere models (Torquato and Strell 1985)	4
Figure 2: Triangulated representation of a sphere and bundle of tubes to illustrate Minkowski tensor valuations for simple geometric bodies.	5
Figure 3: Isotropic and anisotropic models used to evaluate the influence of introduced anisotropy for an arrangement of equally spaced spheroids.....	6
Figure 4: Triangulated pore-grain interface of a subvolume of the Ketton Micro-CT dataset.....	6
Figure 5: Three Micro-CT images of artificial and sedimentary rock used to illustrate directional measures to quantify pore morphology.	8
Figure 6: Estimated directional covariance for the beadpack, Ketton, and Estaillades samples.....	9
Figure 7: Comparison of the anisotropy indices for artificial and sedimentary samples as a function of image size.	10
Figure 8: Stereonet projections of the eigenvectors and eigenvalues as a function of image size	11
Figure 9: Qualitative comparison of the numerical permeability tensor and the characteristic pore size derived from the estimated directional covariance.....	11
Figure 10: Qualitative comparison of the numerical permeability tensor and eigenvalues of the first Minkowski tensor.	12
Figure 11: Left: Comparison of the Minkowski tensor anisotropy index and the anisotropy of the numerically estimated permeability tensor. Right: Estimates of the tortuosity of the Micro-CT images derived from a comparison of the analytical method of Bear and Bachmat with numerical estimates of the permeability tensor.	13
Figure 12: Comparison of the anisotropy of the permeability tensor for the evaluated sedimentary samples..	13

List of Tables

Table 1: Minkowski tensors for a sphere, arrangement of parallel planes and a bundle of tubes.	5
Table 2: Minkowski tensors of parametric pore-grain models.....	6
Table 3: Summary of the results for the analyzed Micro-CT datasets and parametric models.	8
Table 4: Anisotropy indices and Minkowski tensor of the full-size image for the presented samples.	10

Directional measures to characterize anisotropy in pore-scale morphology and flow properties

Lukas Mosser

Professor Olivier Dubrule, Professor Martin J. Blunt

Abstract

The ability of fluids to flow through sedimentary rocks is a critical component in the process of recovering oil and gas from subsurface hydrocarbon accumulations. The formation of hydrocarbon bearing reservoirs is attributed to the deposition of siliciclastic grains or carbonate components followed by burial and diagenesis. Their ability to transport fluids is a function of these depositional environments and can be described on a variety of length scales. At the pore-scale, modern solvers for the (Navier-) Stokes equations allow evaluating intrinsic permeability on segmented high-resolution Micro-CT images of individual samples. To integrate pore-scale information in core, sector or field scale studies, upscaling of pore-scale permeability is necessary. Knowledge about the existence of anisotropy in pore-scale flow properties can have critical implications on effective recovery strategies of oil and gas reservoirs.

This thesis aims to evaluate existing anisotropy at the pore-scale by applying directional measures of statistical variation and pore space morphology. High-resolution Micro-CT data of sedimentary sandstone and carbonate samples have been used in an integrated workflow to evaluate directional variation of pore space morphology and the relation to directional single-phase flow properties.

The covariance was estimated directionally to investigate the possible existence of variation in representative elementary volume (REV) size and pore geometry. We introduce a tensorial extension of Minkowski functionals allowing evaluation of orientational characteristics in the grain-void interface. These directional measures are shown to be physically well-defined and are directly related to the seminal work of Kozeny (1927) and Carman (1937, 1939). A number of simple geometric models are used to illustrate the characteristics of these tensorial measures. By extracting triangulated representations of the pore-grain interface, we are able to evaluate tensorial Minkowski functionals for binary Micro-CT images of sedimentary rock.

Our results indicate that directional estimates of the covariance can be used to assess pore-scale variation such as periodicity indicating the possible existence of stratification and gain information about the existence of REVs of different size in different directions. Directional estimates of the characteristic pore and mean grain size allow a qualitative estimate of the principal directions of flow. Evaluation of the anisotropy in surface orientation in the available Micro-CT images using Minkowski tensors allows evaluation of the REV and variation in surface orientation. By comparing numerical estimates of permeability and applying the theory of Bear and Bachmat (1986, 1990) we obtain directional estimates of the tortuosity factors for a variety of siliciclastic and carbonate samples. Our findings show that Minkowski tensors present a sensitive measure of anisotropy in pore morphology and can be applied to gain qualitative information on the existence of anisotropy at the pore-scale as well as the preferred directions of flow.

Introduction

Many factors governing the success of hydrocarbon exploration projects can be attributed to petrophysical properties of hydrocarbon saturated reservoir rocks. As fluids are transported from the high-pressure reservoir to a low pressure well their preferred path of least resistance is highly dependent on the heterogeneities and anisotropies present in the reservoir. Depending on the recovery mechanisms applied to maximize recovery, such as secondary recovery by water flooding or tertiary methods, information on the presence of these heterogeneities can have major implications on the application of these methods.

On the field scale, anisotropies in reservoir properties can be identified using modern methods in seismic processing. Seismic attributes allow the identification of regional variations in mechanical properties of the reservoir rock. These variations can be introduced in integrated reservoir modeling approaches to distinguish reservoir facies. These are linked with characteristic petrophysical property distributions gained from RCAL and SCAL analysis. Modern geostatistical methods allow the interpretation of ensembles of reservoir models to evaluate uncertainty inherent in the interpretation of the available data. By incorporating pressure transient and production information in a history matching workflow, uncertainty can be reduced.

Enhanced oil recovery methods may be applied to increase production. To effectively apply many EOR methods another length scale of a porous medium must be investigated. The pore-scale, defined as the scale where individual grains and fluid filled gas-filled pores may be distinguished. The pore-scale plays a major role in maximizing the recovery of hydrocarbons beyond residual saturations. From viscous and capillary force balance it can be shown that these residual saturations are functions of pore geometry, wettability characteristics of the grain surfaces and fluid properties.

Modern Micro-CT technology has made it possible to investigate these displacement processes occurring at the sub-millimeter scale and to analyze the controlling mechanisms. A variety of methods have been introduced for the analysis of pore-scale morphology to characterize material properties of porous media such as porosity, grain size distributions or connectivity. To quantify single-phase and two-phase flow properties of sedimentary rocks at the pore-scale, modern numerical solvers for the (Navier-) Stokes equations have been developed (Raeini et al. 2014; Alyafei et al. 2015; Mostaghimi et al. 2016; Nunes et al. 2016). Modern computational resources allow average single-phase flow properties to be determined in reasonable time. Obtaining directional estimates of permeability from high-resolution Micro-CT images is a time and resource consuming process.

This thesis will evaluate two statistical measures that determine the existence of anisotropy in a porous medium. Applied as a pre-processing step in a conventional upscaling workflow these methods help to identify directional variation in static and flow properties before applying computationally expensive methods to evaluate petrophysical properties at the pore-scale. The integration of this data into modern upscaling and integrated reservoir modeling processes allows uncertainty to be reduced due to increased knowledge on anisotropy present in oil and gas reservoirs.

This thesis is structured as follows: We begin by highlighting relevant concepts derived from the seminal work of Guimer (1955) and Debye et al. (1957) to introduce the covariance as a measure of the variance in pore morphology (Vogel 2002). Using simple geometric bodies and parametric models, we present the concept of tensorial Minkowski functionals and their applications to characterize anisotropy in random porous media. These tensors measure the shape and orientation of geometric bodies and are a natural extension of the scalar Minkowski functionals, volume, surface area, integral of mean curvature and the Euler characteristic (Chiu et al. 2013; Vogel et al. 2010; Arns et al. 2001).

In this work, seventeen Micro-CT images of sedimentary rock have been studied to evaluate the applicability of the suggested methods. The analyzed images have dimensions of $\sim 1 \text{ mm}^3$ resolved at resolutions of two to nine μm and have been previously acquired at the Micro-CT imaging facilities at Imperial College London (Bijelic 2015). By applying the directional extension of the covariance, we evaluate anisotropic characteristics of sedimentary rocks and evaluate the qualitative implications on single-phase fluid flow. Triangulated representations of the grain-void interface allow us to compute Minkowski tensors and their variation as a function of the image size. These integral geometric measures enable us to assess the applicability of these measures to quantify anisotropy in the studied samples. By linking tensorial Minkowski functionals to the macroscopic momentum balance introduced by Bear and Bachmat (1986, 1990), we estimate single-phase permeability and compare our results to numerical estimates of the directional permeability obtained from the solution of the Stokes equations on binary representations of each sample.

Literature review

Direct measurements of the effective permeability of porous media can be traced back to the experiments of Darcy (1856) to estimate the permeability of soils. Indirect measurement of material properties of porous media using two-point probability functions can first be attributed to Guimer (1955). Later theoretical and experimental work by Debye et al. (1957) on the scattering of x-rays has shown that two-point probability functions provide the means to characterize key properties of random materials such as the specific surface area. Many publications emphasize the relevance of two-point probability functions by showing that they arise in the description of effective properties governing a broad range of physical processes (Torquato 1997; Prager 1961).

Spatial statistics in the context of porous media with application to fluid flow problems were first considered by Matheron. While not only developing many image morphological concepts (Matheron 1975) his work on the estimation of the effective permeability of a porous medium (Matheron 1967) and his definition of a representative elementary volume (REV) have revolutionized the characterization of random materials with regards to flow in porous media. Based on Matheron's seminal work numerous approaches have been developed to quantify bounds on the effective permeability of random materials (Rubinstein and Torquato 1989). Today, the theory of deriving effective properties by volume averaging methods extends far beyond the field of flow in porous media. The general theory of random materials (Torquato 2002) aggregates methods to characterize and quantify effective properties and provides a rigorous mathematical and physical foundation for application in materials science.

The mathematical methods of modeling and characterizing the spatial distribution and morphology of objects are an active field of research in stochastic geometry (Stoyan et al. 1995). Many of the models developed in the context of stochastic geometry such as the Boolean model (Clausius 1858; Serra 1987) provide proxies for the description of random natural arrangements of objects and their statistical properties (Jacod and Joathon 1972). In earth sciences, many concepts such as angularity or sphericity of clastic grains can be described using image morphological methods and stochastic geometry (Serra 1982).

The covariance and its related covariance functions have been widely applied in stereological applications. Image stereological relations allow volumetric material properties to be related to two dimensional estimates of the covariance. For three-dimensional heterogeneous and isotropic media, it has been shown that the covariance is related to the specific surface area (Guimer 1955; Debye et al. 1957).

The same relationship has been proven for the case of angular averaged estimates of the covariance with regard to anisotropic media (Berryman 1987). For the case of anisotropic media where averaging is not performed, coefficients can be obtained from integral geometric analysis (Gokhale et al. 2005). These approaches allow determination of the specific surface area for a large variety of heterogeneous isotropic and anisotropic materials and therefore obtain an estimate of the effective permeability via the theory of Kozeny (1927) and Carman (1937, 1939).

Kozeny established a theoretical framework for estimating the permeability of a porous medium by deriving an analytical model for the permeability of a bundle of tubes. Carman later evaluated Kozeny's method with available measurement data and estimated the range of validity of his equation. This early work of Carman provides an excellent compendium of experimental and analytical approaches to estimate the permeability of granular beds. Variations of empirical and analytical Kozeny-Carman equations exist (Chapuis and Aubertin 2003). Analytical models of the permeability of dilute and non-dilute beds of spheres have been developed and can be used to compare numerical or experimental measurements of permeability to analytical data (Childress 1972; Howells 1974).

The macroscopic momentum balance approach by Bear and Bachmat (1986, 1990) allows the definition of the permeability tensor of an arbitrary three-dimensional porous medium as a function of the porosity, tortuosity and a measure of surface orientation. For isotropic porous media, their theory reduces to the Kozeny-Carman equation. Recent advances refining the macroscopic momentum balance approach have allowed new upper and lower bounds for the tortuosity to be defined (Guo 2012, 2015) using an analytical form of the tortuosity for anisotropic media based on an orientation tensor of void space in a porous medium (Pietruszczak and Krucinski 1989).

A number of methods to estimate the permeability of a porous medium numerically from volumetric representations have been developed. The two most common approaches to solving the (Navier-) Stokes equations include the Lattice Boltzmann method (Pan et al. 2001, 2004) as well as finite-difference or finite-volume methods. Recent developments in efficient Stokes solvers have made the direct solution of these equations possible direct on binary representations of the pore and void space (Mostaghimi et al. 2013). These binary images result from segmentation in the post-processing of Micro-CT samples of sedimentary rock.

The mathematical field of integral and stochastic geometry allows characterization of random geometric bodies and their arrangement, such as the structures found in natural materials. The simplest morphological measures are the four scalar Minkowski measures first derived from Hadwiger's theorem (Hadwiger 1957): the volume, surface area, the mean curvature and the Euler characteristic. Evaluating these relations as a function of a variable length scale leads to a very efficient descriptor of geometric arrangements. This was shown by applying scalar Minkowski functionals to analyze the large-scale structure of the universe (Mecke et al. 1994). An extension of scalar Minkowski functionals to vectorial and tensorial measures of orientation have been presented by Schröder-Turk et al. (2010). These tensorial measures allow the evaluation of orientational distributions of closed and open surfaces. Interfaces of binary images of porous media obtained from Micro-CT scanners represent open surfaces. For open surfaces, only a subset of the tensorial Minkowski measures is well defined. These so-called translation invariant tensors i.e. their measurement is independent of a reference location have been considered in this study. The additive property of Minkowski functionals makes them robust estimators and allow efficient parallel computation in $O(N)$, where N is the number of voxels of the Micro-CT image (Schröder-Turk et al. 2013). Hörrmann et al. (2014) give analytical estimators of the tensorial Minkowski functionals in two-dimensions for the Boolean model which have been used to estimate the orientation and intensity parameters of an underlying anisotropic Boolean model.

While scalar Minkowski functionals have been applied to characterize effective material properties and pore space morphology (Scholz et al. 2012), the derived relationships are not able to capture anisotropic behavior. Mecke and Arns (2005) highlight the use of Minkowski functionals to compare various modeling approaches for random porous media and show that scalar Minkowski functionals allow prediction of effective material properties. In the context of fluids in porous media, integrals of curvature of fluid interfaces occur in theoretical models to predict the onset of capillary condensation and the critical point of a multi-component mixture (Mecke and Arns 2005).

Many natural materials such as bone structures (Rho et al. 1998) or laminated shales (McLamore and Gray 1967) show a preferential orientation of their structuring components and anisotropic material properties. The orientation dependent tensorial extension of the Minkowski functionals by Schröder-Turk et al. (2013) gives rise to new approaches to formulate relationships for anisotropic material properties (Kuhn et al. 2015). Tensorial translation invariant Minkowski tensors have been shown to arise in the theory of the evolution of the interface of two mixing fluids without capillary tension (Wetzel and Tucker 1999) and in the characterization of foams (Saadatfar et al. 2012). The surface integrals involved in the theory of Bear and Bachmat (1986) have been shown in this work to be closely related to tensorial Minkowski functionals as morphological estimates of surface orientation.

Methodology

Micro-CT images and pre-processing

To evaluate and compare pore space anisotropy of various sedimentary rock samples, seventeen Micro-CT images that have been previously acquired are analyzed. Their size ranges from 300 to 500 voxels edge length and resolutions between two and nine micrometers. These datasets have been studied previously in the context of pore network extraction and modeling and evaluated regarding their static and dynamic petrophysical properties (Dong and Blunt 2009). We also refer the reader to appendix 6 where we present a summary of the properties of each sample. The acquired Micro-CT images have been segmented using Otsu's method and are represented as binary phases: the pore phase and the grain phase. All images are available in the public domain including static and dynamic single-phase flow properties (Bijeljic 2015). To reduce computational cost in the estimation of permeability five images have been downsampled from a resolution of 1000^3 voxels to 500^3 before being used in the analysis.

Covariance

Following the convention defined by Chiu et al. (2013) we define the probability that two points at a distance \mathbf{r} lie within the same phase Σ of the porous medium as

We will refer to $C(\mathbf{r})$ (Equation 1) as the covariance of the porous medium. This definition of the covariance is valid for single and multi-component systems e.g. carbonates with limestone and dolomite grains and intergranular void. The Micro-CT data used in this study contains binary information only therefore the phase of interest Σ is the pore phase.

To compare the covariance of various materials we define the normalized covariance:

We will highlight three essential characteristics of the covariance: The covariance at the origin is equal to the porosity ϕ of the observed phase Ξ . The limit of the covariance as the distance r approaches infinity, stabilizes at ϕ^2 . Finally, as shown by Debye et al. (1957) the first derivative of the covariance at the origin is related to the specific surface area S_v by

Gokhale (2005) highlights that the coefficient associated with the specific surface area varies in the case that radial averaging is not applied, and the covariance must include a measure of the orientation aligned with the direction of observation. Without radial averaging the coefficient of the specific surface area S_v can be obtained from

This relationship between the directional covariance and the specific surface area has significant implications for the later analysis of the available data. While the covariance can be extended to give directional information, it is always related to the total specific surface area and therefore does not allow any additional knowledge to be gained regarding effective directional properties.

Nevertheless, the covariance can be used as a valuable tool to characterize pore-scale morphology in multiple directions. Two quantitative measures can be deduced. We define a characteristic pore size $r_{c,i}$, where the subscript i denotes one of the three Cartesian directions $i \in \{x, y, z\}$:

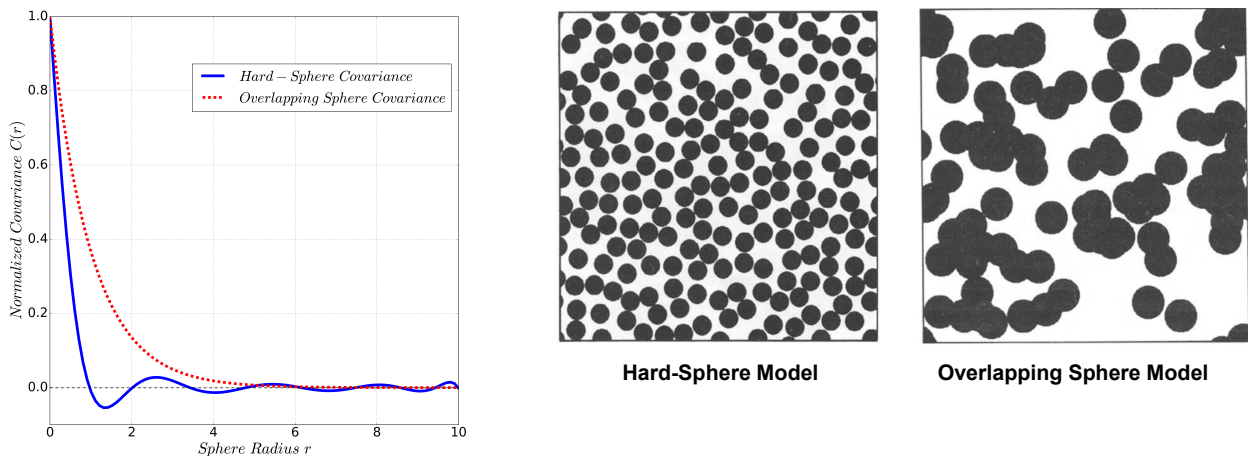


Figure 1: Comparison of the covariance for hard-sphere and overlapping-sphere models (Torquato and Strell 1985). Illustrations reproduced from Smith and Torquato (1988).

Furthermore, we can differentiate between qualitative shapes of the covariance. The existence of the so-called “hole-effect” can indicate short scale order in a porous medium (Figure 1), which occurs due to volume exclusion effects and is typical in systems that can be modeled as non-overlapping spheres (Smith and Torquato 1988). For porous media that exhibit behavior similar to the hard-sphere model, the wavelength of the oscillations observed in the covariance defines a mean grain size r_m . Different shapes of the covariance in specific directions indicate important directional differences in pore space morphology. The distance at which stabilization around ϕ^2 occurs is indicative of the size of the REV and may vary in different directions. If no stabilization occurs the true REV size has not been reached for the volume under investigation.

To obtain a directional estimate of the covariance, we follow the approach presented by Jin et al. (2016). Computation of the covariance is therein performed along linear sections of the binary volumetric image in the direction of interest and averaged across all linear sections in that direction (Pant 2016).

Scalar and tensorial Minkowski functionals

Minkowski functionals present valuable descriptors of pore space shape or morphology (Mecke and Arns 2005). While the scalar Minkowski functionals allow mean values for a given porous medium to be obtained, tensorial Minkowski measures allow additional directional information to be gained.

We can define four scalar Minkowski functionals: volume, surface area, integral of mean curvature and the Euler characteristic. It is important to note that due to the interface between pores and grains in sedimentary rocks typically being open surfaces i.e. the interface has disconnected edges, only translation invariant properties can be estimated.

Tensorial Minkowski functionals can be interpreted as indicators of how much of a scalar Minkowski measure is oriented in the direction of observation. To better relate the scalar and tensorial Minkowski functionals we will use the notation defined by Schröder-Turk et al. (2010).

We define the general equation from which all scalar, vectorial and tensorial Minkowski functionals can be derived as

The subscript ν in equation 6 denotes the order of the scalar Minkowski functional whereas superscripts r, s relate to the exponents defined in the general form (Equation 6).

To characterize pore space morphology two translation invariant tensors i.e. their estimation is independent of a reference location, have been considered. Due to mesh dependency effects (Appendix 4) only the first Minkowski tensor $W_1^{0,2}$ which is closely related to the surface area $W_1^{0,0}$ was considered:

The normalization of $W_1^{0,2}$ by the surface area $W_1^{0,0}$ allows an intuitive interpretation of the first Minkowski tensor:

The normalized tensor $\bar{W}_1^{0,2}$ represents the fraction of the total surface area oriented in the principal directions (Equation 9). The ratio of minimal and maximal eigenvalues of $W_1^{0,2}$ can be used to define an index of anisotropy $\beta_1^{0,2}$ (Schröder-Turk et al. 2013):

Combining the eigenvalues of $W_1^{0,2}$ with their respective eigenvectors these are interpreted as an oriented ellipsoid describing the directions and magnitude of anisotropy of the evaluated surface.

We illustrate this measure of anisotropy by evaluating the first Minkowski tensor $W_1^{0,2}$ and its anisotropy index $\beta_1^{0,2}$ for a set of simple geometric bodies (Figure 2). The random bundle of non-intersecting tubes was chosen to resemble the theoretical model used to derive the Kozeny-Carman equation (Kozeny 1927). Table 1 presents the first Minkowski tensor and the corresponding anisotropy index $\beta_1^{0,2}$ for the evaluated geometries.

	$\bar{W}_1^{0,2}$	$\beta_1^{0,2}$
Sphere	$\begin{bmatrix} 0.333 & 0 & 0 \\ 0 & 0.333 & 0 \\ 0 & 0 & 0.333 \end{bmatrix}$	1.0
Planes	$\begin{bmatrix} 1.0 & 0 & 0 \\ 0 & 0 & 0 \\ 0 & 0 & 0 \end{bmatrix}$	Not defined
Bundle of Tubes	$\begin{bmatrix} 0.5 & 0 & 0 \\ 0 & 0.5 & 0 \\ 0 & 0 & 0 \end{bmatrix}$	Not defined

Figure 2: Triangulated representation of a sphere and bundle of tubes to illustrate Minkowski tensor valuations for simple geometric bodies.

Table 1: Minkowski tensors for a sphere, arrangement of parallel planes and a bundle of tubes. Spherical bodies exhibit pure isotropic behavior.

For a sphere, the first Minkowski tensor shows pure axis aligned isotropy. The isotropic behavior is emphasized by the anisotropy index being equal to one. Computing $\bar{W}_1^{0,2}$ for the arrangement of planar surfaces shows that the surface has only one primary orientation. Finally, the bundle of tubes is isotropic in the plane representing the base of the tubes and zero in the third direction as the tubes are open and therefore no surface area is oriented in this direction.

Anisotropic parametric models as pore-grain analogs

While simple geometric models such as spheres and bundles of tubes can highlight the most basic characteristics of the Minkowski tensors, all these models show isotropic behavior. To underline the effect of anisotropy on the evaluated Minkowski tensor functionals and relate these simple models to the complex pore space found in sedimentary rocks parametric models were created. A NURBS (Non-Uniform-Rational-B-Spline) representation of an equally spaced array of spheroids was used to extract a pore-void interface that mimics the grain surfaces seen in natural sedimentary rocks. By rescaling two of the three axis aligned ellipsoids we introduce anisotropy into the geometry. A detailed description of the parametric modeling process can be found in appendix 3. We present here three parametric models of spheres and ellipsoids. By keeping the radius constant in the z-direction and reducing the radius of the ellipsoids in the x-y plane, anisotropy is introduced between the x-y plane and the z-direction.

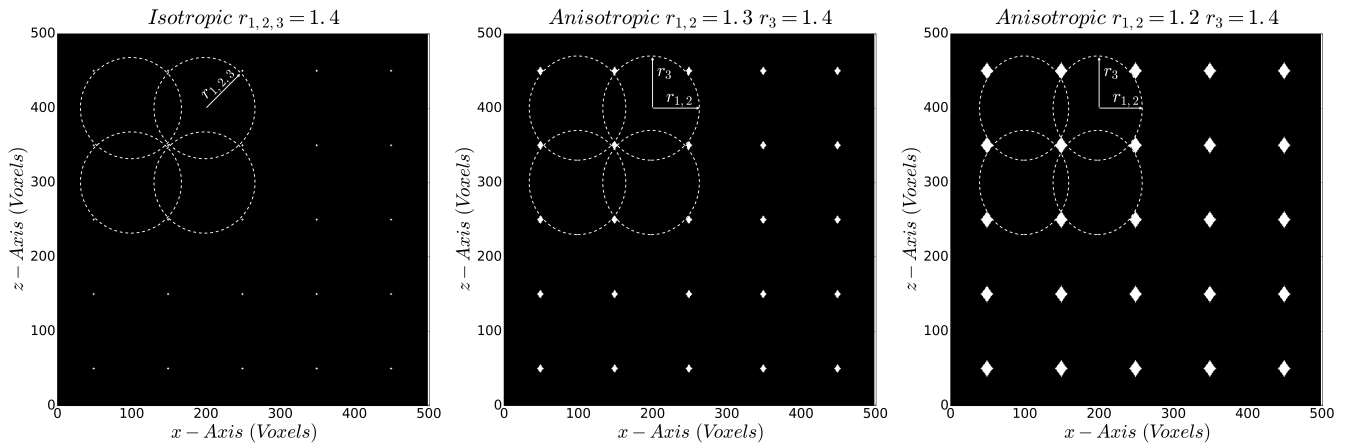


Figure 3: Isotropic and anisotropic models used to evaluate the influence of introduced anisotropy for an arrangement of equally spaced spheroids. X-Z plane is shown where anisotropy increases from left to right. Dotted lines indicate cross-sections of the structuring ellipsoidal or spherical grains.

Table 2 shows the resulting Minkowski tensors and anisotropy indices for the range of parametric models. We observe that the tensorial Minkowski functional indicates isotropic behavior in the x-y plane. Even though the change in the diameter is small, this measure is highly sensitive and indicates significant anisotropy of the pore grain interface.

Where the parametric description of boundary surfaces is possible, analytical equations of the Minkowski functionals can be derived. For pore-grain interfaces, this is not feasible, and therefore computations must be performed on a triangulated approximation of the interface extracted from the binary Micro-CT images using a triangulation algorithm such as marching cubes (Figure 4) (Appendix 4).

	$\bar{W}_1^{0,2}$	$\beta_1^{0,2}$
Isotropic $r_{1,2,3} = 1.4$	$\begin{bmatrix} 0.333 & 0 & 0 \\ 0 & 0.333 & 0 \\ 0 & 0 & 0.333 \end{bmatrix}$	1.0
Anisotropic $r_{1,2} = 1.3$ $r_3 = 1.4$	$\begin{bmatrix} 0.361 & 0 & 0 \\ 0 & 0.361 & 0 \\ 0 & 0 & 0.277 \end{bmatrix}$	0.77
Anisotropic $r_{1,2} = 1.2$ $r_3 = 1.4$	$\begin{bmatrix} 0.382 & 0 & 0 \\ 0 & 0.382 & 0 \\ 0 & 0 & 0.235 \end{bmatrix}$	0.61

Table 2: Minkowski tensors of parametric pore-grain models. Isotropic behavior can be observed for spherical grains. A change of 8% and 16% in the diameter of the grains in the x-y plane of the anisotropic parametric models leads to a significant change in the anisotropy index $\beta_1^{0,2}$.

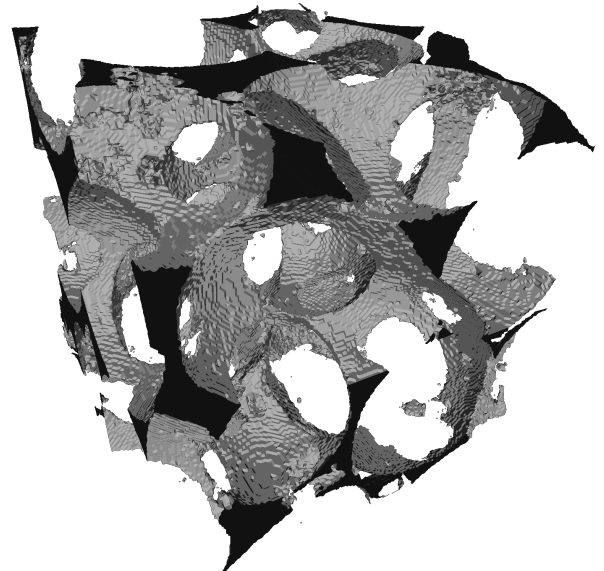


Figure 4: Triangulated pore-grain interface of a subvolume of the Ketton Micro-CT dataset. The bounding box of the extracted mesh has 200 μm side length and contains $\sim 850,000$ triangles.

Estimation of directional permeability

The first analytical models to estimate permeability of a porous medium can be attributed to the seminal work of Kozeny (1927) and later Carman who verified and generalized Kozeny's approach and compared it to experimental data for various grain size distributions. Kozeny's original formulation (Appendix 1B) also introduced the concept of tortuosity and is considered as a measure of the length of the actual path a particle being transported through a porous medium takes.

The Kozeny-Carman equation relates the effective average permeability of a porous medium with the specific surface area S_v , the porosity ϕ , and the tortuosity τ by:

The factor C_α in equation 11 is a shape factor depending on the shape of the pores and commonly assumed as $C_\alpha = 2$ for circular pores. For our purpose, specific surface areas have been determined by evaluating the covariance (Equation 1) as well as from the computation of the scalar Minkowski functional $W_1^{0,0}$ (Equation 7).

Using a macroscopic momentum balance Bear and Bachmat (1986) derive a theoretical expression for the permeability tensor k_{ij} :

Where α_{ij} is a measure of the orientation of the grain-fluid interface $S_{\alpha\beta}$:

Moreover, the tortuosity factor is defined as

By comparing the surface integrals in equation 13 and the first translation invariant Minkowski tensor $\bar{W}_1^{0,2}$ (Equation 9) we derive an expression for α_{ij} given as

By taking $v = 1$ and $(r, s) = (1, 1)$ in equation 6 we define the translation co-variant Minkowski Tensor $W^{1,1}$ as

This allows us to express the tortuosity factor (Equation 14) in terms of the tensorial Minkowski functional $W_1^{1,1}$:

By computing numerical estimates of the permeability in the three axis aligned orientations direct on the segmented binary image of the pore space (Mostaghimi et al. 2013) we compare numerical results of the permeability with estimates derived from the theory of Bear and Bachmat incorporating the use of the first Minkowski tensor $\bar{W}_1^{0,2}$.

Rearranging equation 12,

allows us to estimate the factor $C_\alpha \tau^2$ which can be used e.g. to obtain an empirical relationship for the directional permeability without the need to compute the directional permeability using computationally expensive numerical methods.

Results

For this study seventeen Micro-CT images of artificial and sedimentary rock, as well as five parametric grain models, have been analyzed regarding their directional static characteristics and their single-phase permeability (Table 3). To highlight the use of the covariance and Minkowski tensors as measures of pore space anisotropy, we will consider three distinctive samples (Figure 5). The beadpack is an artificial sample of equally sized spheres with a diameter of $100 \mu\text{m}$. Ketton represents an oolitic limestone with spheroidal grains, whereas Estaillades is a complex carbonate of biogenic origin showing no distinct grains. Table 3 presents a summary of the results for each evaluated sample whereas appendix 6 gives a detailed analysis of the results for each sample individually.

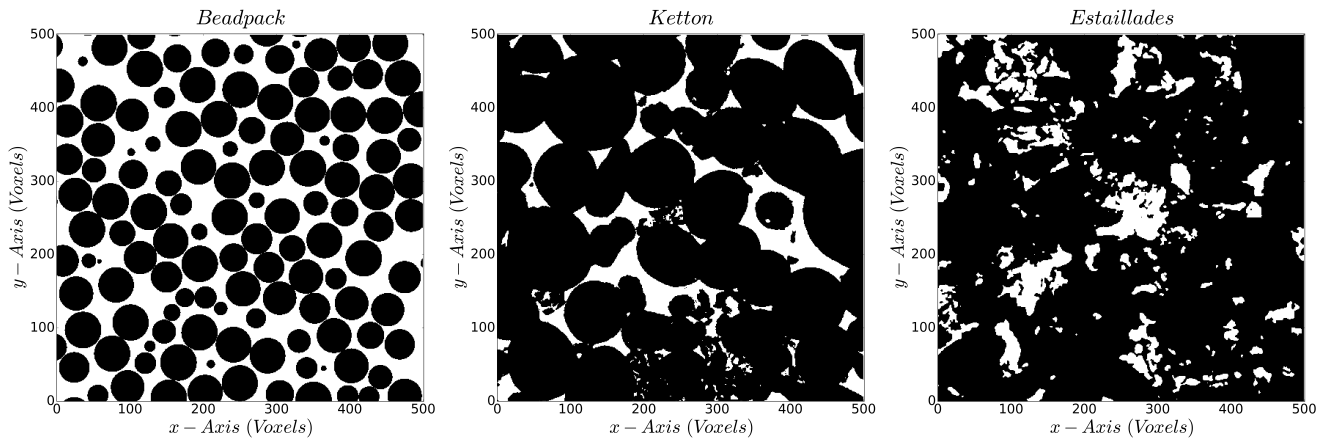


Figure 5: Three Micro-CT images of artificial and sedimentary rock used to illustrate directional measures to quantify pore morphology. The beadpack (left) consists of spheres of equal diameter and is equivalent to the theoretical hard-sphere model (Figure 1). Ketton (middle) is an oolitic limestone consisting of individual ellipsoidal grains. Estaillades (right) represents a sample of a complex carbonate with no distinguishable grains.

Sample Name	Rock Type	Porosity [-]	Average Permeability [Darcy]	Permeability Tensor Anisotropy $\frac{k_{min}}{k_{max}}$	Anisotropy Index $\beta_1^{0,2}$ [-]
				[-]	
Beadpack	Artificial	0.36	6.236	0.98	0.99
Bentheimer	Sandstone	0.20	2.658	0.81	0.86
Berea	Sandstone	0.20	1.302	0.88	0.92
Doddington	Sandstone	0.19	0.296	0.86	0.84
Estaillades	Carbonate	0.12	0.116	0.48	0.86
Ketton	Carbonate	0.13	3.940	0.64	0.77
C1	Carbonate	0.23	1.117	0.53	0.58
C2	Carbonate	0.17	0.073	0.11	0.67
S1	Sandstone	0.14	1.699	0.67	0.68
S2	Sandstone	0.25	3.950	0.79	0.75
S3	Sandstone	0.17	0.227	0.26	0.60
S4	Sandstone	0.17	0.262	0.75	0.59
S5	Sandstone	0.21	4.727	0.91	0.76
S6	Sandstone	0.24	11.11	0.95	0.75
S7	Sandstone	0.25	7.058	0.80	0.76
S8	Sandstone	0.34	13.34	0.96	0.68
S9	Sandstone	0.22	2.253	0.67	0.82
Isotropic $r_{1,2,3} = 1.4$	Parametric	0.04	0.3e-3	1.0	1.0
Isotropic $r_{1,2,3} = 1.3$	Parametric	0.11	0.936	0.99	1.0
Isotropic $r_{1,2,3} = 1.2$	Parametric	0.21	8.621	0.99	1.0
Anisotropic $r_{1,2} = 1.3$ $r_3 = 1.4$	Parametric	0.08	0.379	0.15	0.77
Anisotropic $r_{1,2} = 1.2$ $r_3 = 1.4$	Parametric	0.15	3.430	0.18	0.61

Table 3: Summary of the results for the analyzed Micro-CT datasets and parametric models. Sample porosity was determined from the estimated covariance at the origin ($r=0$). Directional permeability was computed using a parallel implementation of the method to solve the Stokes equation on binary Micro-CT images (Mostaghimi et al. 2013). The anisotropy index $\beta_1^{0,2}$ (Equation 10) based on the first translation invariant Minkowski tensor $\overline{W}_1^{0,2}$ (Equation 9) was evaluated from triangulated representations of the pore-grain interface (Appendix 4).

Integrated computational workflow

While analytical and empirical relationships for the covariance, Minkowski functionals, and single phase permeability exist for simple geometric arrangements, the complex pore-grain structure of sedimentary rock requires numerical computation of these parameters. An integrated workflow was developed to compute these directional properties for binary Micro-CT data (Appendix 2). All Micro-CT data used in this study is publicly available in a binary pre-processed format (Bijeljic 2015). Due to grid sizes of modern Micro-CT images exceeding 100 million grid cells (500^3 voxels), currently available geostatistical libraries such as RGeostats were not suitable due to memory requirements greater than sixteen gigabytes exceeding available computational resources. An implementation of the covariance estimator optimized for binary Micro-CT images presented by Pant (2016) was used to evaluate the directional covariance.

The evaluation of tensorial Minkowski functionals requires a triangulated surface representation of the grain-void interface. The marching cubes method (Lorensen and Cline 1987) was used to extract surface meshes from binary representation (Appendix 4). The open-source library Karambola (Schröder-Turk et al. 2013) allowed computation of Minkowski tensors on arbitrary triangulated surfaces. For each Micro-CT image approximately 250 meshes were extracted at increasing image size. Due to a large number of meshes required for the Minkowski tensor analysis, an automated workflow was necessary. Any existing mesh defects such as non-manifold vertices would have made this evaluation impossible. The marching cubes implementation available in the visualization toolkit (VTK) produces high resolution triangulated representations of the pore-grain interface (Appendix 4). No non-manifold vertices were encountered using these software implementations. To further reduce computational time, the workflow was executed in parallel on a number of desktop computers.

Numerical estimates of the directional permeability were obtained by employing a parallelized implementation of the method described by Mostaghimi et al. (2013). The workflow, software, and documentation required to reproduce the figures and results in this thesis have been made publicly available (Appendix 5).

Covariance estimation

The directional covariance was estimated using an implementation of the algorithm presented by Pant (2016) (Appendix 6). The beadpack sample shows periodicity in all three directions due to the presence of a significant hole effect (Figure 6 left). Kozeny (1927) shows for equal sized spheres of diameter d_{grain} that the specific surface area S_v can be analytically determined as function of the beadpack porosity:

The mean grain size and specific surface area derived from the covariance (Equation 3) show an error of 8 % when compared to the theoretical value ($d_{grain} = 100 \mu m$) of $S_v = 38250 m^{-1}$ (Equation 19). Ketton (Figure 6 middle) shows a significantly smaller characteristic pore size in the z direction with strong periodicity indicating a structural difference in the vertical and horizontal directions. By comparing the covariance of hard and non-overlapping spheres (Figure 1) with the results shown in figure 6 we find that the beadpack closely resembles, as expected, the hard-sphere model. Ketton shows similarity to the hard-sphere model in the z-direction whereas the x and y direction are interpreted as overlapping grains. Finally, Estaillades shows no periodicity in the covariance arising due to the complex structure of the pore space (Figure 6 right).

To estimate the REV scale for these samples, the directional variations in pore space morphology must be taken into account. The size of the REV is the same in all directions for the beadpack. For Ketton the size of the REV is direction dependent as stabilization occurs later for the z-direction. Consequently, the largest stabilization distance must be chosen as the REV scale. No stabilization can be observed in the Estaillades sample and therefore no distinct REV size can be defined.

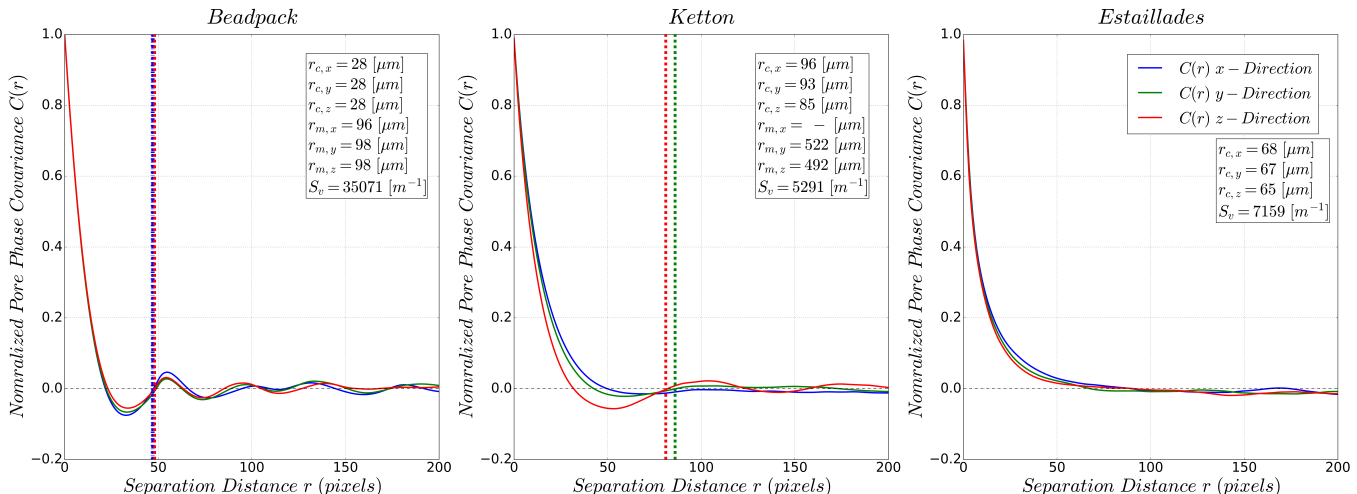


Figure 6: Estimated directional covariance for the beadpack, Ketton, and Estaillades samples. Directional variations show structural differences which is supported by the analytical shape of the covariance of hard and non-overlapping spheres (Figure 1). Vertical lines indicate the wavelength of the covariance which defines the mean grain size $r_{m,i}$.

Minkowski tensors as measures of pore space anisotropy

The grain pore interfaces of the analyzed samples have been discretized using a marching cubes algorithm (Appendix 4). The anisotropy index $\beta_1^{0,2}$ was evaluated numerically as a function of the window size. This allows the definition of an anisotropy based REV where the shape of the graph $\beta_1^{0,2}(r)$ stabilizes and the intrinsic anisotropy of the material is reached (Figure 7).

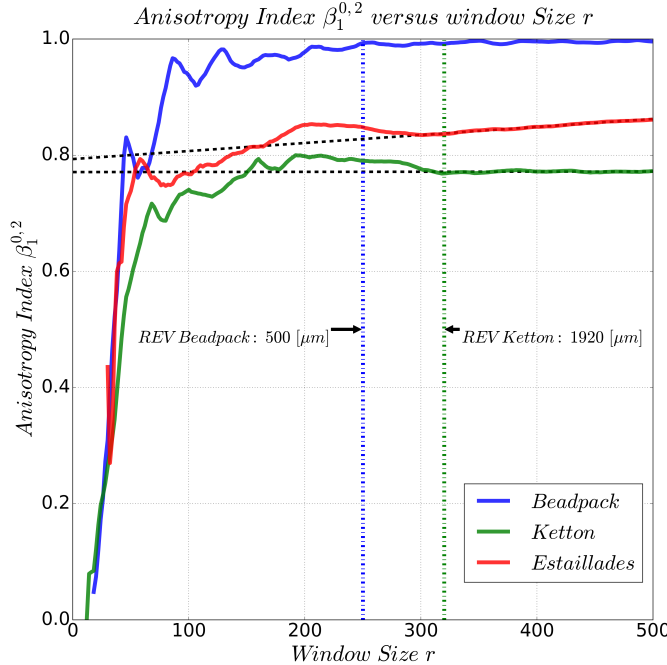


Figure 7: Comparison of the anisotropy indices for artificial and sedimentary samples as a function of image size. Stabilizations indicate the REV determined from surface anisotropy.

For the beadpack, isotropic behavior can be observed where $\beta_1^{0,2}$ approaches unity and an REV of approximately $500 \mu\text{m}$ can be identified. This is equivalent to five times the diameter of the individual grains ($d_{\text{grain}} = 100 \mu\text{m}$). Early fluctuations can be explained by the image containing individual spherical grains at 50, 80 and 120 voxels respectively.

Ketton shows a clear stabilization at $1920 \mu\text{m}$, additionally highlighted by the horizontal dashed straight line fit. The linear least squares regression for the Estaillades sample shows that no stabilization is obtained within the image. This indicates that the REV has not been reached as the material exhibits a change in anisotropy. While a short stabilization is reached at 200 voxels it is necessary to evaluate the significance of this anisotropy by averaging over an ensemble of sub volumes at this length scale. Table 3 presents the normalized first Minkowski tensor $\bar{W}_1^{0,2}$ and the anisotropy index $\beta_1^{0,2}$ at the full image size for each sample.

From these results, we were able to deduce directional trends of the pore-grain interface. The beadpack sample shows clear isotropic behavior and no preferential orientation. For Ketton, we can observe a preferential orientation where 40% of the interface is oriented in the z-direction. While the anisotropy index has been evaluated for Estaillades for the full image, it is not possible to define the orientation of the pore-grain interface representative of an REV and may change when larger samples of the carbonate are acquired and analyzed. Where distinct grains in the material can be identified such as Ketton or the beadpack, the magnitude of the anisotropy index can be interpreted as the ratio of the shortest and longest half axis of a representative grain. For Ketton the estimated anisotropy may occur due to preferential cementation of the calcite oolites leading to deformation of the individual grains.

Decomposition of the Minkowski tensor into eigenvalues and eigenvectors allows directional information of the pore grain interface as a function of the subvolume size to be obtained. Using a stereonet projection of the eigenvectors we can analyze the three-dimensional vectors and their change in orientation (Figure 8). Furthermore, we have attributed the eigenvectors with their respective eigenvalues showing the directions of minimum (blue), intermediate (green) and maximum (red) eigenvalues. Increasing saturation in color corresponds to increasing subvolume size. Colored diamonds indicate the orientation of the eigenvectors at full image size. Isocontours indicate the two sigma range for the density of eigenvectors.

The randomly dispersed pattern observed for the artificial beadpack sample (Figure 8) arises from the isotropic nature of the Minkowski tensor for this sample. This dispersion in the eigenvector orientation arises because the eigenvalues tend towards $\frac{1}{3}$ for isotropic media and all orientations are equally likely to occur. Unlike the beadpack, Ketton shows a well-defined cluster of data points at large sample size (high color saturation). This focused orientation of the pore grain interfaces underlines that there exists one intrinsic anisotropy and orientation in the material. This trend follows our previous observation (Figure 7 middle) that there is a well-defined REV scale for the Ketton sample.

Estaillades has been shown not to exhibit an REV at the full image scale based on the anisotropy index $\beta_1^{0,2}$ which can also be observed from the directional distribution of the eigenvectors of the Minkowski tensor. We observe no clustering at large sample sizes with no stabilized orientation.

Sample Name	$\bar{W}_1^{0,2} [-]$	$\beta_1^{0,2} [-]$
Beadpack	$\begin{bmatrix} 0.333 & 0 & 0 \\ 0 & 0.333 & 0 \\ 0 & 0 & 0.333 \end{bmatrix}$	0.99
Estaillades	$\begin{bmatrix} 0.316 & 0 & 0 \\ 0 & 0.321 & 0 \\ 0 & 0 & 0.364 \end{bmatrix}$	0.86
Ketton	$\begin{bmatrix} 0.306 & 0 & 0 \\ 0 & 0.322 & 0 \\ 0 & 0 & 0.372 \end{bmatrix}$	0.77

Table 4: Anisotropy indices and Minkowski tensor of the full-size image for the presented samples.
The beadpack shows near isotropic behavior while Ketton and Estaillades both show a significant level of anisotropy.

To summarize our findings on evaluating the anisotropy of the material using Minkowski tensors we conclude that it is possible to define two criteria to establish an REV. To estimate the size of the REV for anisotropic samples based on the Minkowski tensor $\bar{W}_1^{0,2}$ it is necessary for stabilization of the anisotropy index to occur over a sufficient range of consecutive sample sizes.

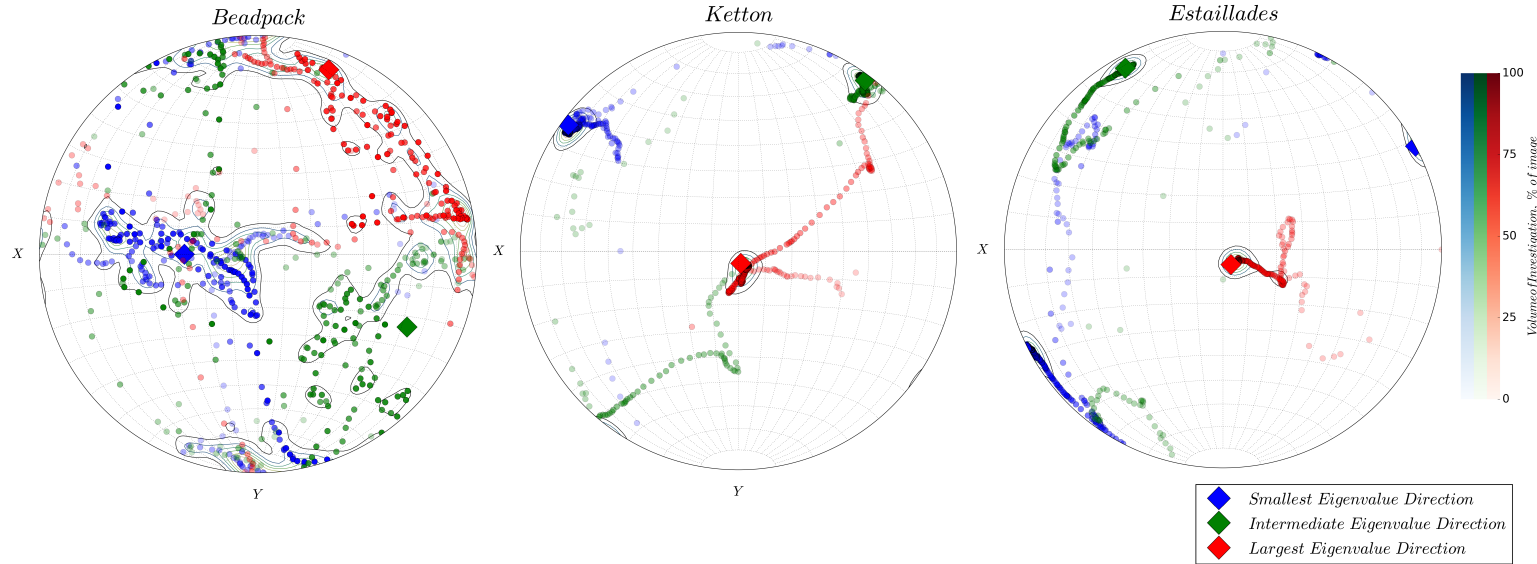


Figure 8: Stereonet projections of the eigenvectors and eigenvalues as a function of image size for three presented samples. Diamonds indicate the directions of minimum (blue), intermediate (green) and maximum (red) eigenvalues. Increasing colour saturation indicates larger image size.

This establishes a scale and magnitude of intrinsic anisotropy in the material. For sedimentary or carbonate samples consisting of distinct grains this information can be used to infer the shape of the average grains in terms of a representative spheroid (Hörrmann et al. 2014). The second criterion can be established from the eigenvector decomposition. For materials exhibiting isotropic behavior, random scattering is expected. If the analyzed material has a preferred intrinsic orientation, a dense cluster of orientations can be observed in the stereonet projection of the eigenvectors. For sedimentary samples for which no REV can be defined no stabilization in the anisotropy index or the distribution of eigenvectors can be found.

Single-phase flow properties

Prediction of single-phase permeability from directional covariance

Permeability was computed on the binary segmented representations of the acquired seventeen Micro-CT datasets using a finite difference method to solve the Stokes equation (Mostaghimi et al. 2013). The theory of Kozeny and Carman relates the effective permeability for isotropic media to the specific surface area S_v , and the tortuosity of the pore space. We have shown in the methodology section that the directional covariance is directly related to the specific surface area (Equation 4). This implies that only the average effective permeability can be obtained from the covariance using the Kozeny-Carman relationship (Equation 11). The directional characteristic pore size $r_{c,i}$ (Equation 5) has been correlated with the numerical directional permeability. Smaller characteristic pore radii are expected to correlate with smaller permeabilities whereas larger pore radii with higher permeabilities in the corresponding direction. Figure 9 shows a correlation matrix of the directional permeability with the characteristic pore size obtained from the directional covariance estimates.

Blue shading indicates that the direction of the smallest, intermediate or largest permeability coincide with the direction of the smallest, intermediate and largest characteristic pore size respectively.

Directional alignment can be observed for many samples including the complex Estaillades sample. Deviations from this trend can be explained by the fact that the size of the images for samples S1-S9, C1-2 (Table 3) may not be sufficient to estimate the covariance accurately.

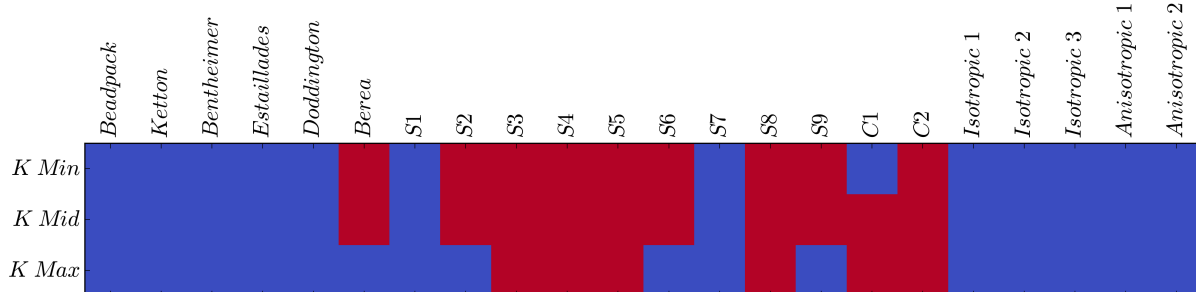


Figure 9: Qualitative comparison of the numerical permeability tensor and the characteristic pore size derived from the estimated directional covariance. Blue shading indicates that the magnitude and direction of the characteristic pore size is aligned with the magnitude and direction of the permeability tensor e.g. the smallest permeability and characteristic pore size can be observed in the x-direction. A red shading indicates that the numerical estimate of the directional permeability does not correlate with the directional characteristic pore size. Twelve out of twenty-two samples (~55%) show directional alignment of the characteristic pore size and permeability.

Minkowski tensors as qualitative indicators of directional permeability

The Kozeny-Carman equation (Equation 11) allows us to establish a qualitative link between the first Minkowski tensor and the directional permeability. As we have shown earlier, the first Minkowski tensor can be interpreted as the orientational distribution of the surface area of the pore-grain interface. Due to the inverse relationship with the specific surface area, the direction of the largest eigenvalue will align with the direction of the smallest permeability, and the direction of the smallest eigenvalue corresponds to the highest permeability.

We illustrate this relationship by defining the set of sorted eigenvalues λ_i of the Minkowski tensor $W_1^{0,2}$ corresponding to the fraction of the total specific surface area S_v oriented in the direction of the eigenvectors e_i :

$$\lambda_1 > \lambda_2 > \lambda_3 \text{ and } \{e_1, e_2, e_3\}. \dots \quad (20)$$

Evaluation of the Minkowski tensor $\bar{W}_1^{0,2}$ (Appendix 6) for the studied Micro-CT data has shown that off-diagonal terms are of the order less than 1e-2 and therefore the tensors are assumed to be aligned with the Cartesian coordinate system. By recalling the Kozeny-Carman relationship (Equation 11) the estimated permeabilities k_i in the direction i is proportional to the fraction of the specific surface area λ_i :

Qualitatively, therefore, the ordered estimated directional permeabilities are related to the sorted eigenvalues of $\bar{W}_1^{0,2}$ such that

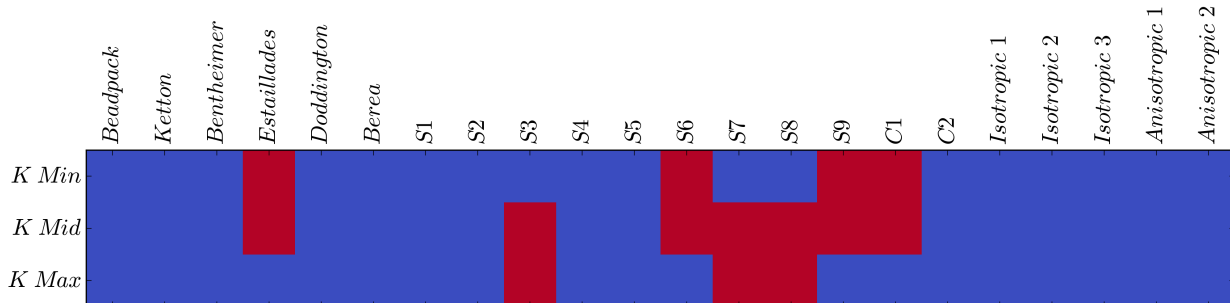


Figure 10: Qualitative comparison of the numerical permeability tensor and eigenvalues of the first Minkowski tensor. Blue shading indicates that the eigenvalues and eigenvectors of the first Minkowski tensor are aligned with the magnitude and direction of the permeability tensor according to the qualitative correlation given by equation 22. A red shading indicates that the numerical estimate of the directional permeability does not agree with the eigenvalues of the Minkowski tensor $\overline{W}_1^{0,2}$. Fifteen out of twenty-two samples (~70%) show directional alignment of the Minkowski tensor and permeability. For all analyzed samples, the estimated Minkowski tensor correctly predicts the direction of maximal or minimal permeability.

Figure 10 summarizes the results of this qualitative relationship for twenty-two samples of which five are artificial parametric models as presented in the methodology section (Appendix 3). A blue shading indicates that the eigenvalues of the first Minkowski tensor are aligned with the permeability according to the theory of Kozeny-Carman; a red shading indicates otherwise. For most of the analyzed samples, a good correlation between the estimated permeability and the Minkowski tensor can be observed. For all samples at least one direction, the minimum or maximum permeability is correctly predicted.

A cross-plot of the anisotropy of the numerically estimated directional permeability and the anisotropy index $\beta_1^{0,2}$ shows that the magnitude of the anisotropy index $\beta_1^{0,2}$ cannot predict the ratio of minimum and maximum directional permeability (Figure 11 left). More than 80% of the analyzed samples that show anisotropy in pore morphology based on the geometric anisotropy index $\beta_1^{0,2}$ show anisotropy in the estimated directional permeability. Three samples show near isotropic permeability ($\frac{k_{min}}{k_{max}} > 0.9$) while the anisotropy index $\beta_1^{0,2}$ predicts a greater anisotropy.

Following the theory of Bear and Bachmat (1986) highlighted in the methodology section, the Minkowski tensor $W_1^{0,2}$ has been used to estimate the factor α_{ij} (Equation 15) that accounts for orientation information of the pore grain interface. While we have shown that the tortuosity factor T_{ij}^* (Equation 17) is related to the Minkowski tensor $W_1^{1,1}$ we were able to estimate the tortuosity $C_\alpha \tau^2$ by comparing the numerical estimate of directional permeability with the analytical results (Equation 18).

The permeability predicted using equation 12 considerably overestimates the permeability which is reflected in the high tortuosity factors (Figure 11 right). While for porosities greater than 20% reasonable values for $C_\alpha \tau^2$ are obtained (Mostaghimi et al. 2013), low porosity samples show exceedingly high tortuosity factors.

Discussion

Knowledge of an existing anisotropy in sedimentary structures can have a significant impact on optimal recovery strategies for oil and gas reservoirs or the application of enhanced recovery methods. We have evaluated two methods to analyze the pore-scale morphology and identify anisotropic characteristics in Micro-CT images of siliciclastic and carbonate samples.

Evaluating the directional covariance allows a qualitative assessment of the pore space morphology (Figure 9). Local differences in pore structures can be observed where sedimentary or chemical processes have altered the pore and grain structure. This can be seen in the Ketton sample (Figure 6, 7, 8) where evidence was found of significant differences in the pore structure between horizontal and vertical directions. These directional differences are evident from the reduced characteristic pore size (Figure 6), the Minkowski tensor $W_1^{0,2}$ having its largest eigenvalue in the vertical direction (Figure 7, Table 4) where the lowest value of permeability can be found. While it is not possible to attribute this directional change solely to one mechanism without further investigation, chemical processes leading to preferential cementation of the oolite grains presents a possible explanation.

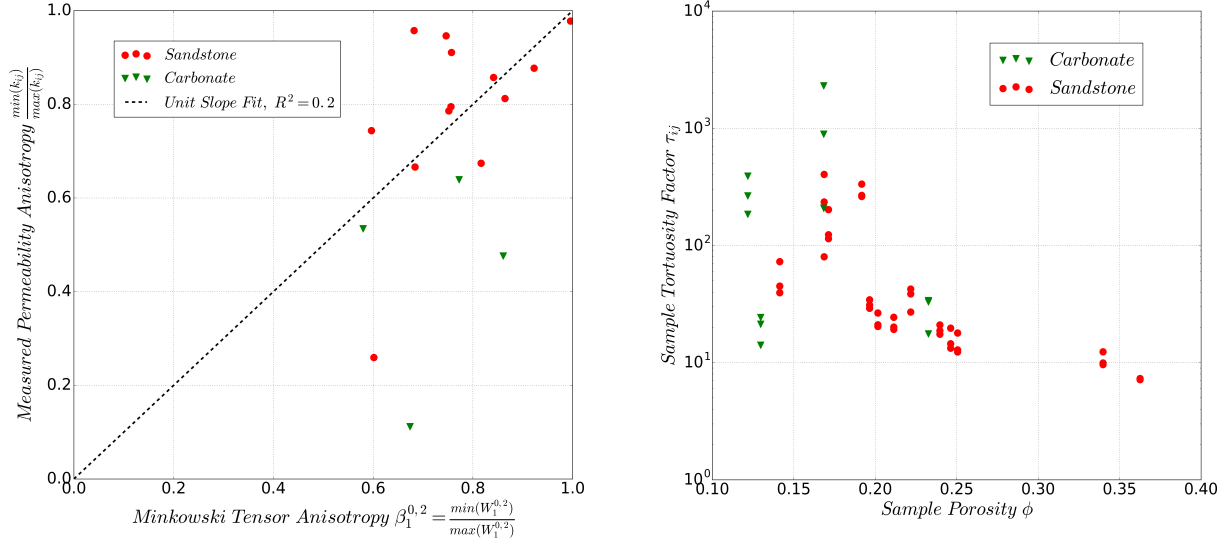


Figure 11: Left: Comparison of the Minkowski tensor anisotropy index and the anisotropy of the numerically estimated permeability tensor. Right: Estimates of the tortuosity of the Micro-CT images derived from a comparison of the analytical method of Bear and Bachmat with numerical estimates of the permeability tensor. A linear least squares regression of the data presented in figure 11 (left) with a unit slope straight line shows an R^2 value of 0.2, clearly indicating that it is not possible to quantify the anisotropy of the permeability tensor based on the Minkowski tensor anisotropy index $\beta_1^{0,2}$.

Moreover, the evaluation of the covariance and tensorial Minkowski measures shows that their use is effective when both methods are applied together. For the majority of the samples analyzed both the covariance and Minkowski tensor indicate the presence of anisotropy in the pore-grain interface (Figure 9, 10). The definition of a representative elementary volume from the covariance can be challenging and in many cases ambiguous. Stabilization of the covariance is hard to determine and varies in different directions indicating the need to define directional REVs. Using the Minkowski tensor to determine an REV size based on intrinsic material anisotropy (Figure 7) and stabilization in the orientation distribution (Figure 8) is intuitive and considered an advantage of tensorial Minkowski measures compared to the covariance.

We have found no evidence that the magnitude of the anisotropy index $\beta_1^{0,2}$ can be linked directly to the anisotropy of the permeability tensor (Figure 11 left). We have shown that Minkowski tensors have a physical interpretation in the context of the macroscopic momentum balance theory of Bear and Bachmat (1986). These relationships allow empirical tortuosity factors for each spatial direction to be determined where numerical estimates of permeability are available. A detailed analysis incorporating theoretical results on upper and lower bounds of permeability should be performed to reduce uncertainty. Incorporation of the translation covariant Minkowski Tensor $W_1^{1,1}$ could lead to better estimates of the permeability from spatial statistics of the pore-grain interface and will be considered as future work.

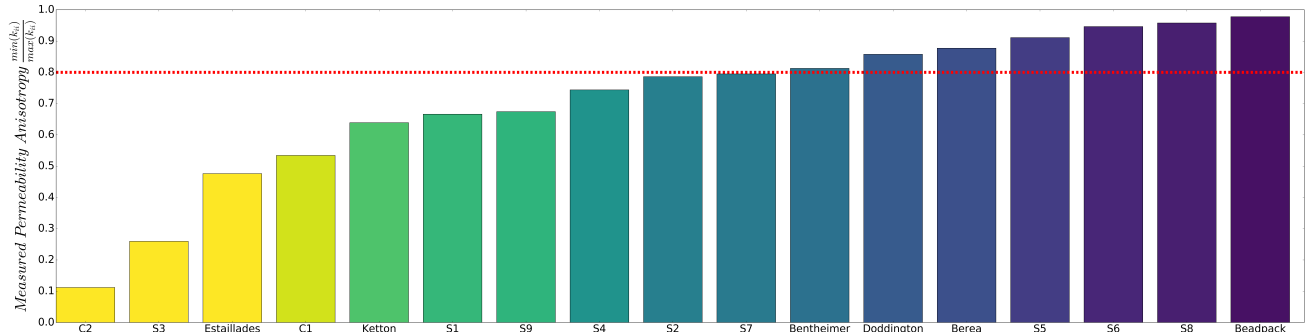


Figure 12: Comparison of the anisotropy of the permeability tensor for the evaluated sedimentary samples considered in this study. Sixty percent of the analyzed samples show a difference greater than 20% between the smallest and largest values of permeability. More than 80% of the sedimentary samples show a permeability anisotropy greater than 10%.

Finally, our analysis has shown that most samples of sedimentary rock show an intrinsic anisotropy of the permeability tensor (Figure 12). The impact of this anisotropy of the permeability at the pore-scale must be evaluated on a case by case basis for the applications considered. Our results challenge the assumption that granular sedimentary rock e.g. Ketton, Doddington or Bentheimer (Appendix 6) can be regarded as isotropic at the pore-scale and directional measures such as Minkowski functionals provide effective tools to determine the presence and nature of directional variation in pore space morphology.

Efficient parallel algorithms have been developed to compute Minkowski functionals in linear time complexity $O(N)$, where N is the total number of voxels in the Micro-CT image (Schröder-Turk et al. 2013). For modern Micro-CT data where N is of the order of billions of voxels, the computational effort to solve the (Navier-) Stokes equations becomes exceedingly high. While no evidence was found that the Minkowski tensor $W_1^{0,2}$ can provide an estimate of the directional permeability of a porous medium, this integral geometric property presents a sensitive measure of the anisotropy in pore space morphology at a reduced computational cost. The ability of tensorial Minkowski functionals to characterize the orientational distribution of the pore-grain interface could lead to improved methods to constrain the reconstruction and modeling of porous media based on volumetric Micro-CT data.

Tensorial Minkowski functionals could prove to be a valuable tool to characterize porous media and physical processes where anisotropic behavior is known to exist a priori. Many sedimentary rocks and their components, such as shales or bedded sandstones, exhibit anisotropic behavior. The mechanical and fluid flow properties of shales have been shown to be highly directional dependent (McLamore and Gray 1967). For processes and materials where distinct geometric bodies occur, such as foams (Huber and Gibson 1988) or granular materials consisting of individual grains, the class of translation covariant Minkowski tensors provide a rich framework to describe the orientation, arrangement, and anisotropy of their structuring elements (Kapfer et al. 2010). In multi-phase flow applications, these Minkowski tensors could be used to describe the morphology of fluid ganglia, migrating and trapped fluids. Other possible applications of these integral geometric descriptors extend far beyond the field of oil and gas and could prove invaluable in medical and material sciences.

Conclusions

Micro-CT images of artificial and sedimentary rock have been evaluated regarding their static and dynamic properties as a function of the direction of measurement. By applying the classic covariance or two-point probability function in three orthogonal directions, we were able to identify directional differences in pore space morphology. We have implemented a novel extension of scalar Minkowski functionals to tensorial measures first introduced by Schröder-Turk et al. (2013). These tensors can be used to characterize the anisotropy of the pore-grain interface. By numerically estimating the anisotropy of the Minkowski tensor characterizing the orientation of the boundary surface as a function of image size we were able to determine REV length scales based on measures of surface anisotropy and preferential orientation.

By numerically estimating the permeability of the studied samples we were able to relate pore-grain interface anisotropy to single-phase directional permeability. Our results show that Minkowski measures allow a qualitative estimation of the principal directions of flow. While the covariance cannot provide an effective measure of directional permeability, characteristic pore sizes derived from directional estimates of the covariance provide a good qualitative correlation with the single-phase permeability tensor. We, therefore, conclude that both the covariance and Minkowski tensors are complimentary measures for the primary directions of flow and can be used to evaluate the existence of anisotropy without the need to perform computationally expensive measurements of the permeability tensor.

By showing the relationship of Minkowski tensors to the macroscopic momentum balance approach of Bear and Bachmat (1986), we highlight the physical interpretation and importance of this new class of integral geometric relations. Comparison of the estimated permeability with finite-difference measurements of permeability show that it is not sufficient to include surface orientation effects alone, but the characterization of the tortuosity is necessary and considered as future work.

As Mecke and Arns (2005) have shown, the application of Minkowski functionals to the field of fluids in porous media is rich for the case of scalar Minkowski measures. Future work will focus on extending these approaches to incorporate directional information in the form of measured Minkowski tensors in new material models. Characterization of foams for enhanced oil recovery methods or changes in the grain sizes and shapes due to chemical dissolution processes could be quantified using Minkowski vectors and tensors. Empirical measurements of these geometric descriptors could provide effective new constraints for image reconstruction and modeling of the pore space morphology found in Micro-CT images of sedimentary rock.

Nomenclature

$P(\cdot)$	Probability function
\mathcal{E}	Pore-phase
o	Origin of coordinate system
\mathbb{R}^d	Set of real valued numbers of dimension- d
$C(r)$	Covariance
$C(r, \theta, \phi)$	Directional covariance
$G(r, \theta', \phi')$	Surface orientation function (Gokhale et al. 2005)
S_v	Specific surface area
\bar{r}_c	Characteristic pore size
K	Geometric body

∂K	Boundary/surface of body K
$W_v^{r,s}(K)$	Minkowski functional (r, s) of order v
G_v	$v=1,2: G_v = 1, v=3: G_v = \text{mean curvature}$
$W_1^{0,0}(K)$	Surface area of body K
$W_1^{0,2}(K)$	First translation invariant tensorial Minkowski functional
$W_1^{1,1}(K)$	First translation covariant tensorial Minkowski functional
$\beta_1^{0,2}$	Anisotropy index derived from $W_1^{0,2}(K)$
$\#(\cdot)$	Count function, number of elements in set
k_{eff}	Effective permeability
k_{ij}	Permeability tensor
α_{ij}	Surface orientation tensor
δ_{ij}	Dirac delta function
$S_{\alpha\beta}$	Pore-grain boundary surface
C_α	Kozeny-Carman geometric factor
T_{ij}^*	Tortuosity factor
ϕ	Porosity
τ	Tortuosity

References

- Alyafei, N., A. Q. Raeini, A. Paluszny, and M. J. Blunt. 2015. "A Sensitivity Study of the Effect of Image Resolution on Predicted Petrophysical Properties." *Transport in Porous Media* 110 (1). Springer Netherlands: 157–69. doi:10.1007/s11242-015-0563-0.
- Arns, C. H., M. A. Knackstedt, W V Pinczewski, and K R Mecke. 2001. "Euler-Poincaré Characteristics of Classes of Disordered Media." *Physical Review E, Statistical, Nonlinear, and Soft Matter Physics* 63 (3 Pt 1): 031112. doi:10.1103/PhysRevE.63.031112.
- Bear, J., and Y. Bachmat. 1986. "Macroscopic Modeling of Transport Phenomena in Porous Media. 2: Applications to Mass, Momentum, and Energy Transport." *Transport in Porous Media* 1: 241–69. doi:10.1007/BF00238182.
- Bear, J., and Y. Bachmat. 1990. *Introduction to Modeling of Transport Phenomena in Porous Media*. Springer Netherlands. doi:10.1007/978-94-009-1926-6.
- Berryman, J. G. 1987. "Relationship between Specific Surface Area and Spatial Correlation Functions for Anisotropic Porous Media." *Journal of Mathematical Physics* 28 (1): 244. doi:10.1063/1.527804.
- Bijeljic, B. 2015. "Imperial College Micro-CT Database." <https://www.imperial.ac.uk/engineering/departments/earth-science/research/research-groups/perm/research/pore-scale-modelling/micro-ct-images-and-networks/>.
- Carman, P C. 1937. "Fluid Flow through Granular Beds." *Transactions-Institution of Chemical Engineers* 15. Institution of Chemical Engineers: 150–66. doi: 10.1016/S0263-8762(97)80003-2.
- Carman, P. C. 1939. "Permeability of Saturated Sands, Soils, and Clays." *The Journal of Agricultural Science* 29: 262. doi:10.1017/S0021859600051789.
- Chapuis, R. P., and M. Aubertin. 2003. "Predicting the Coefficient Permeability of Soils Using the Kozeny-Carman Equation." *École Polytechnique de Montréal*, no. January: 1–31.
- Childress, S. 1972. "Viscous Flow Past a Random Array of Spheres." *The Journal of Chemical Physics* 56 (6): 2527. doi:10.1063/1.1677576.
- Chiu, S. N., D. Stoyan, W. S Kendall, and J. Mecke. 2013. *Stochastic Geometry and Its Applications*. John Wiley & Sons.
- Clausius, R. 1858. "Über Die Bewegende Kraft Der Wärme, Teil I, Teil II."
- Darcy, H. P. G. 1856. "Les Fontaines Publiques de Ill. Ville de Dijon." *Victor Dalmont*.
- Debye, P., H. R. Anderson, and H. Brumberger. 1957. "Scattering by an Inhomogeneous Solid. II. the Correlation Function and Its Application." *Journal of Applied Physics* 28 (6): 679–83. doi:10.1063/1.1722830.
- Dong, H., and M. J. Blunt. 2009. "Pore-Network Extraction from Micro-Computerized-Tomography Images." *Physical Review E - Statistical, Nonlinear, and Soft Matter Physics* 80 (3): 1–11. doi:10.1103/PhysRevE.80.036307.
- Gokhale, A. M., A. Tewari, and H. Garmestani. 2005. "Constraints on Microstructural Two-Point Correlation Functions." *Scripta Materialia* 53 (8): 989–93. doi: 10.1016/j.scriptamat.2005.06.013.
- Guimer, A., G. Fournet. 1955. "Small Angle Scattering of X-Rays." *J. Wiley & Sons, New York*.
- Guo, P. 2012. "Dependency of Tortuosity and Permeability of Porous Media on Directional Distribution of Pore Voids." *Transport in Porous Media* 95 (2): 285–303. doi:10.1007/s11242-012-0043-8.
- Guo, P. 2015. "Lower and Upper Bounds for Hydraulic Tortuosity of Porous Materials." *Transport in Porous Media* 109 (3). Springer Netherlands: 659–71. doi:10.1007/s11242-015-0541-6.
- Hadwiger, H. 1957. "Vorlesungen Über Inhalt, Oberfläche Und Isoperimetrie." *Springer*.
- Hörrmann, J., D. Hug, M. Andreas Klatt, and K. Mecke. 2014. "Minkowski Tensor Density Formulas for Boolean Models." *Advances in Applied Mathematics* 55 (1): 48–85. doi:10.1016/j.aam.2014.01.001.
- Hörrmann, J., and W. Weil. 2015. "Valuations and Boolean Models," 1–34. <http://arxiv.org/abs/1510.07910>.
- Howells, I.D. 1974. "Drag due to the Motion of a Newtonian Fluid through a Sparse Random Array of Small Fixed Rigid Objects." *J. Fluid Mech.* 64: 449–75.
- Huber, A. T., and L. J. Gibson. 1988. "Anisotropy of Foams." *Journal of Materials Science* 23 (8): 3031–40. doi:10.1007/BF00547486.
- Jacod, J., and P. Joathan. 1972. "Conditional Simulation of Sedimentary Cycles in Three Dimensions." In *Mathematical Models of Sedimentary Processes*, pp 139–65. doi:10.1007/978-1-4684-1995-5_7.
- Jin, C., P. A. Langston, G. E. Pavlovskaya, M. R. Hall, and S. P. Rigby. 2016. "Statistics of Highly Heterogeneous Flow Fields Confined to Three-Dimensional Random Porous Media." *Physical Review E - Statistical, Nonlinear, and Soft Matter Physics* 93 (1). doi:10.1103/PhysRevE.93.013122.

- Kapfer, S. C., W. Mickel, F. M. Schaller, M. Spanner, C. Goll, T. Nogawa, N. Ito, K. Mecke, and G. E. Schröder-Turk. 2010. "Local Anisotropy of Fluids Using Minkowski Tensors." *Journal of Statistical Mechanics: Theory and Experiment* 2010 (11): P11010. doi:10.1088/1742-5468/2010/11/P11010.
- Kozeny, J. 1927. "Über Kapillare Leitung Des Wassers Im Boden." *Akad. Wiss. Wien* 136: 271–306.
- Kuhn, M. R., Wai Ching Sun, and Qi Wang. 2015. "Stress-Induced Anisotropy in Granular Materials: Fabric, Stiffness, and Permeability." *Acta Geotechnica* 10 (4). Springer Berlin Heidelberg: 399–419. doi:10.1007/s11440-015-0397-5.
- Lorensen, W., and H. Cline. 1987. "Marching Cubes: A High Resolution 3D Surface Construction Algorithm." *ACM Siggraph Computer Graphics* 21 (4): pp. 163–69.
- Matheron, G. 1967. "Éléments Pour Une Théorie Des Milieux Poreux."
- Matheron, G. 1975. *Random Sets and Integral Geometry. Wiley Series in Probability and Mathematical Statistics: Probability and Mathematical Statistics*.
- McLamore, R., and K. E. Gray. 1967. "The Mechanical Behavior of Anisotropic Sedimentary Rocks." *Journal of Engineering for Industry* 89 (1): 62–73. doi:10.1115/1.3610013.
- Mecke, K. R., T. Buchert, and H Wagner. 1994. "Robust Morphological Measures for Large-Scale Structure in the Universe." *Astronomy and Astrophysics* 288 288: 697–704. doi:10.1017/CBO9781107415324.004.
- Mecke, K., and C. H. Arns. 2005. "Fluids in Porous Media: A Morphometric Approach." *Journal of Physics: Condensed Matter* 17 (9): S503–34. doi:10.1088/0953-8984/17/9/014.
- Mostaghimi, P., M. J. Blunt, and B. Bijeljic. 2013. "Computations of Absolute Permeability on Micro-CT Images." *Mathematical Geosciences* 45 (1): 103–25. doi:10.1007/s11004-012-9431-4.
- Mostaghimi, P., M. Liu, and C. H. Arns. 2016. "Numerical Simulation of Reactive Transport on Micro-CT Images." *Mathematical Geosciences*, no. August. doi:10.1007/s11004-016-9640-3.
- Nunes, J P Pereira, M J Blunt, and B Bijeljic. 2016. "Journal of Geophysical Research: Solid Earth Pore-Scale Simulation of Carbonate Dissolution in Micro-CT Images." doi:10.1002/2015JB012117
- Pan, C X, M Hilpert, and C T Miller. 2004. "Lattice-Boltzmann Simulation of Two-Phase Flow in Porous Media." *Water Resources Research* 40 (2): W01501. doi:10.1029/2003WR002120.
- Pan, C., M. Hilpert, and C. Miller. 2001. "Pore-Scale Modeling of Saturated Permeabilities in Random Sphere Packings." *Phys. Rev. E* 64 (6): 1–9. doi:10.1103/PhysRevE.64.066702.
- Pant, L. 2016. "Stochastic Characterization and Reconstruction of Porous Media." http://www.esdlab.mece.ualberta.ca/pdfs/Lalit_phdthesis.pdf.
- Pietruszczak, S., and S. Krucinski. 1989. "Description of Anisotropic Response of Clays Using a Tensorial Measure of Structural Disorder." *Mechanics of Materials* .2-3 (8: 237–49.
- Prager, S. 1961. "Viscous Flow through Porous Media." *Physics of Fluids* 4 (12): 1477. doi:10.1063/1.1706246.
- Raeini, A. Q., M. J. Blunt, and B. Bijeljic. 2014. "Direct Simulations of Two-Phase Flow on Micro-CT Images of Porous Media and Upscaling of Pore-Scale Forces." *Advances in Water Resources* 74. Elsevier Ltd: 116–26. doi:10.1016/j.advwatres.2014.08.012.
- Rho, J. Y., L. Kuhn-Spearing, and P. Ziopoulos. 1998. "Mechanical Properties and the Hierarchical Structure of Bone." *Medical Engineering and Physics* 20 (2): 92–102. doi:10.1016/S1350-4533(98)00007-1.
- Rubinstein, J., and S. Torquato. 1989. "Flow in Random Porous Media: Mathematical Formulation, Variational Principles, and Rigorous Bounds." *Journal of Fluid Mechanics* 206 (1889): 25. doi: 10.1017/S0022112089002211.
- Saadatfar, M., M. Mukherjee, M. Madadi, G. E. Schröder-Turk, F. Garcia-Moreno, F. M. Schaller, S. Hutzler, A. P. Sheppard, J. Banhart, and U. Ramamury. 2012. "Structure and Deformation Correlation of Closed-Cell Aluminum Foam Subject to Uniaxial Compression." *Acta Materialia* 60 (8): 3604–15. doi: 10.1016/j.actamat.2012.02.029.
- Scholz, C., F. Wirner, Jan Götz, U. Röde, G.E. Schröder-Turk, K. Mecke, and C. Bechinger. 2012. "Permeability of Porous Materials Determined from the Euler Characteristic." *Physical Review Letters* 109 (26): 1–5. doi:1 0.1103/PhysRevLett.109.264504.
- Schröder-Turk, G. E., S. Kapfer, B. Breidenbach, C. Beisbart, and K. Mecke. 2010. "Tensorial Minkowski Functionals and Anisotropy Measures for Planar Patterns." *Journal of Microscopy* 238 (1): 57–74. doi: 10.1111/j.1365-2818.2009.03331.x.
- Schröder-Turk, G. E., W. Mickel, S. C. Kapfer, F. M. Schaller, B. Breidenbach, D. Hug, and K. Mecke. 2013. "Minkowski Tensors of Anisotropic Spatial Structure." *New Journal of Physics* 15. doi:10.1088/1367-2630/15/8/083028.
- Serra, J. 1982. *Image Analysis and Mathematical Morphology*. Academic Press, London.
- Serra, J. 1987. "Boolean Random Functions." *Acta Stereol.* 6: 325–30.
- Smith, P., and S. Torquato. 1988. "Computer Simulation Results for the Two-Point Probability Function of Composite Media." *Journal of Computational Physics* 76 (1): 176–91. doi:10.1016/0021-9991(88)90136-2.
- Stoyan, S., Kendall, W. S., Mecke, J. 1995. *Stochastic Geometry and Its Applications*. doi: 10.1002/bimj.4710390510.
- Torquato, S. 1997. "Exact Expression for the Effective Elastic Tensor of Disordered Composites." *Physical Review Letters* 79 (4): 681–84. doi:10.1103/PhysRevLett.79.681.
- Torquato, S. 2002. "Random Heterogeneous Materials." *Springer Verlag-New York*. doi:10.1007/978-1-4757-6355-3.
- Torquato, S., and G. Strell. 1985. "Microstructure of Two-Phase Random Media." *J. Chem. Phys* 82 (2).
- Vogel, H. J., U. Weller, and S. Schlöter. 2010. "Quantification of Soil Structure Based on Minkowski Functions." *Computers and Geosciences* 36 (10): 1236–45. doi: 10.1016/j.cageo.2010.03.007.
- Vogel, H.-J. 2002. "Topological Characterization of Porous Media." *Morphology of Condensed Matter, Edited by K. Mecke, D. Stoyan, Lecture Notes in Physics* 600: 75–92. doi: 10.1007/3-540-45782-8_3.
- Wetzel, E. D., and C. L. Tucker. 1999. "Area Tensors for Modeling Microstructure during Laminar Liquid-Liquid Mixing." *International Journal of Multiphase Flow* 25 (1): 35–61. doi: 10.1016/S0301-9322(98)00013-5.

Appendices

Appendix 1A: Milestones

Journal/DOI	Year	Title	Authors	Contribution
	1856	Les Fontaines Publiques de l'Ile Ville de Dijon.	H.P.G. Darcy	First experiments on the hydraulic conductivity of porous soils.
Akad. Wiss. Wien, 136	1927	Über kapillare Leitung des Wassers im Boden	J. Kozeny	Derived an analytical relationship for the permeability for spherical bead packs
10.1016/S0263-8762(97)80003-2	1937	Fluid flow through granular beds	P. C. Carman	An extensive compendium of experimental and theoretical work to estimate permeability from material properties.
10.1063/1.1722830	1957	Scattering by an inhomogeneous solid. II. the correlation function and its application	P. Debye	Theoretical and analytical relationship between two-point probability functions and effective material properties.
Springer Berlin	1957	Vorlesungen über Inhalt, Oberfläche und Isoperimetrie	H. Hadwiger	Formulated a (proven) theorem about the morphological requirements to describe geometrical bodies. Minkowski functionals are a direct result of this theorem.
10.1007/BF00238182	1986	Macroscopic modeling of transport phenomena in porous media. 2: Applications to mass, momentum and energy transport	J. Bear and Y. Bachmat	Derived an analytical equation for the permeability at the REV scale by applying a macroscopic momentum balance approach.
10.1063/1.527804	1987	Relationship between specific surface area and spatial correlation functions for anisotropic porous media	J.G. Berryman	Derived an equation for the surface area derived from the covariance of an anisotropic material. Allows effective permeability to be derived using the Kozeny-Carman equation.
10.1017/S0022112089002211	1989	Flow in random porous media: mathematical formulation, variational principles, and rigorous bounds	J. Rubinstein and S. Torquato	Derived analytical bounds for the effective permeability of a random porous medium. This relationship contains a characteristic length scale which can be estimated from an empirical correlation function.
10.1016/S0301-9322(98)00013-5	1999	Area tensors for modeling microstructure during laminar liquid-liquid mixing	E. Wetzel and C. Tucker	Analytical derivation of the equations governing the mixing of two fluids without interfacial tension. Define surface orientation tensor equivalent to the first translation invariant Minkowski tensor.
10.1103/PhysRevE.64.066702	2001	Pore-scale modeling of saturated permeabilities in random sphere packings	C. Pan, M. Hilpert, C. Miller	Describe a lattice Boltzmann method to compute the permeability of random materials from Micro-CT images.
10.1007/978-1-4757-6355-3	2002	Random Heterogeneous Materials	S. Torquato	A collection of theoretical approaches to model random materials by statistical or empirical methods. Provides classification framework for problems in random materials. Solutions and theoretical bounds for numerous applications.
10.1088/0953-8984/17/9/014	2005	Fluids in porous media: a morphometric approach	K. Mecke and C.H. Arns	Introduced concept of scalar Minkowski functionals in the context of fluids in porous media. Comparison of various modeling approaches and incorporation of Minkowski functionals in constitutive physical laws.
10.1088/1367-2630/15/8/083028	2013	Minkowski tensors of anisotropic spatial structure	Schröder-Turk, G.E. Mickel, W. Kapfer, S. C. et al.	Extended the theory on scalar Minkowski functionals to vectorial and tensorial measures derived from Hadwiger's theorem. Provide numerical algorithms to compute Minkowski tensors on arbitrary surfaces and provide numerous applications
10.1007/s11004-012-9431-4	2013	Computations of Absolute Permeability on Micro-CT Images	P. Mostaghimi, M.J. Blunt, B. Bijeljic	Developed finite-difference implementation of Stokes equations with accurate boundary conditions for permeability estimation of binary Micro-CT images. Evaluated validity of Kozeny-Carman equation at the pore-scale and length scales for REVs.

Appendix 1B: Summaries of key milestone publications

Akad. Wiss. Wien 136: 271–306

Year: 1927

Title: Über Kapillare Leitung Des Wassers Im Boden

Author(s): Kozeny, J.

Contribution:

Established the first mathematical description relating an applied pressure gradient to observed flow rates.

Derived an equation for the permeability of a bundle of tubes with an equal diameter under steady laminar flow conditions. This equation relates the specific surface area of a material and its porosity to the observed permeability. Many of the later contributions to estimate permeability from material properties are based on the work of Kozeny and later Carman who evaluated the validity of Kozeny's method with new experimental data. In its original form Kozeny gives a relation for the permeability of a spherical bead packs as:

$$k = c \frac{l_s}{l_w} \frac{\phi^3}{36(1 - \phi)^2} d_w^2$$

Here the factor $\frac{l_s}{l_w}$ describes the tortuosity of the pore space.

Methodology:

Based on previous experiments evaluating the relationship between applied pressure gradients, observed flow rates, grain size and sorting in each material a simple relationship to estimate the single-phase permeability of materials under steady laminar flow is established. Kozeny derived analytical relationships for special cases such as spherical bead packs and compared the validity of his theory by comparison with published data.

Conclusion:

The work of Kozeny is considered as one of the earliest milestones in the theory of flow in porous media. His analytical model to compute permeability based on intrinsic material properties has influenced many later works trying to improve or disprove the validity of the Kozeny-(Carman) equation for various flow regimes and materials. His mathematical derivations and analytical approach introduced new concepts such as the tortuosity derived from physical observations.

Comments:

The manuscript is in German and easy to follow along. Many experimental results are provided as well as references are given to a large number of resources from the time of Kozeny. His work gives insight into a rich community of theoretical and experimental work performed in the field of flow in porous media. An English translation of the manuscript is not available but would be a valuable contribution.

Journal of Applied Physics 28 (6): 679–83. doi:10.1063/1.1722830.
 Year: 1957

Title: Scattering by an Inhomogeneous Solid. II. The Correlation Function and Its Application *

Author(s): Debye, P., H. R. Anderson, and H. Brumberger

Contribution:

The authors establish a theoretical relationship between the experimental results of small angle x-ray scattering of porous media and the theory of two-point probability functions also known as the covariance. They show that for porous media that have a random distribution of pore diameters, the two-point probability function has an exponential form and can be observed experimentally in their results. Their analysis shows that it is possible to estimate the specific surface area from the initial slope of the covariance. Their contribution is based on earlier work by Debye and Bueche (1949) who first developed a method to analyze materials by small angle scattering of x-ray radiation.

Methodology

Based on classical theory on scattering they show that the two-point correlation function is related to the intensity of scattered radiation:

$$I = 4\pi \langle \eta \rangle_{av} V \int \gamma(r) r^2 \frac{\sin(ksr)}{ksr} dr$$

Where $\gamma(r)$ is the empirical covariance of an analyzed sample. Following mathematical derivation shows that the specific surface area S_v is related to the covariance by:

$$S_v = \frac{S}{V} = -4\phi(1-\phi) \left. \frac{d\gamma(r)}{dr} \right|_{r=0}$$

By comparing their theoretical with the experimental results, they are able to evaluate material properties for numerous samples and show the validity of their work. They refer to the work of Guinier and Fournet (1955) as well as Porod (1952) who have derived the same analytical results using a different approach. The experimental study of Van Nordstrand and Johnson (1954) used a purely empirical approach to defining a relation between the specific surface area and two-point probability functions.

Conclusion:

The theoretical work of Debye et al. is one of the first references that highlights the ability to derive material properties from two-point correlation functions. Their work presents the basis for later analytical and experimental work in the field of random porous media and has influenced new interest in the field of spatial probability functions allowing for a full statistical model of random porous media in the context of n-point probability functions.

Comments:

A short and precise paper that gives most mathematical derivation steps as well as experimental results. Attributing Guinier et. al. to have obtained similar results prior to Debye and nearly at the same time from a similar approach is humbling. Unknowing at the time, their results are not only valid for isotropic media but also anisotropic as is later shown by Berryman (1987).

Journal of Mathematical Physics 28 (1): 244. doi:10.1063/1.527804.

Year: 1987

Title: Relationship between Specific Surface Area and Spatial Correlation Functions for Anisotropic Porous Media

Author(s): Berryman, J. G.

Contribution:

In the context of anisotropic porous media, the work of Berryman provides a mathematical foundation to apply the covariance as a measure of the pore-scale morphology and material properties. He showed that the specific surface area of an anisotropic random porous medium could be derived from a radially averaged covariance. Therefore, estimates of the specific surface area of an anisotropic porous medium can be derived from empirical covariance functions and used in conjunction with the Kozeny-Carman equation that relates the specific surface area of a porous medium to predict the effective average single-phase permeability.

Methodology

For anisotropic media, Berryman recognized that the two-point probability function exhibits a translation invariance property i.e. the result is independent of the location of measurement. This relationship allowed him to evaluate the two-point probability function for a binary porous medium solely as a function of orientation. The resulting expression for the specific surface area is equivalent to the result derived by Debye et al. (1957).

Conclusion:

The results of Berryman show that estimates of the specific surface area may be obtained from measurements of the covariance function for isotropic and anisotropic media. While one could assume that this is possible, a mathematical proof for this is necessary. His work also highlights the versatility of the covariance function in the context of estimating material properties and its applicability to random materials.

Comments:

A short but valuable contribution towards characterizing anisotropic random media.

Mathematical Geosciences 45 (1): 103–25. doi:10.1007/s11004-012-9431-4.

Year: 2013

Title: Computations of Absolute Permeability on Micro-CT Images

Author(s): Mostaghimi, P., M. J. Blunt, B. Bijeljic

Contribution:

The authors present a novel finite-difference implementation with exact no-flow boundary conditions at the pore-grain interface to solve the Stokes equation directly on binary segmented Micro-CT images. The proposed method has been validated against lattice Boltzmann methods. The permeability of sand packs, sandstone, and carbonate samples was computed with respect to three Cartesian directions to analyze the anisotropy of permeability at the pore-scale. Their results show that the REV at the pore-scale may vary significantly compared to static properties such as porosity or the specific surface area as well as permeability. The authors show that the Kozeny-Carman equation significantly overpredicts the permeability of sedimentary samples at the pore-scale.

Methodology:

The authors develop a new finite-difference scheme to solve the Stokes equation on binary images. Their method decouples pressure and velocity in a Semi-Implicit formulation. By including a correction term for pressure and velocity, they can establish convergence. Their convergence criterion evaluates the flux across voxelized elements. The sparse system of linear equations is solved iteratively using an algebraic multigrid solver. By applying a known pressure gradient and evaluating the flux, they are able to numerically estimate the permeability of binary images.

Conclusion:

Using the method developed to compute numerical estimates of permeability on binary Micro-CT images, the authors show that the Kozeny-Carman equation fails to predict the permeability of many samples of natural sandstones and carbonates. Significant correction factors have to be introduced to account for the deviation from observed values of permeability. By evaluating the porosity, as well as the specific surface area across a range of sample sizes, they establish sizes of the REV for a number of samples of sedimentary and artificial rock. Their results show a significant variation in REV size when derived from static or dynamic flow properties.

Comments:

Extraction of the largest connected pore space may not be representative of the permeability of a Micro-CT sample. A method to find all connected components should be applied to find all contributing sub-volumes before solving the relevant equations.

New Journal of Physics 15. doi: 10.1088/1367-2630/15/8/083028

Year: 2010

Title: Minkowski Tensors of Anisotropic Spatial Structure

Author(s): Schröder-Turk, G. E., W. Mickel, S. C. Kapfer, F. M. Schaller, B. Breidenbach, D. Hug, K. Mecke

Contribution:

The authors extend the classical framework of scalar Minkowski functionals, volume, surface area, the integral of mean curvature and the Euler characteristic to tensorial functionals. They provide a rigorous mathematical framework from which many integral geometric tensor properties can be derived. The developed theory of vectorial and tensorial Minkowski functionals is accompanied by discretized equations that allow the integrals to be solved for arbitrary surfaces. By providing a number of examples where Minkowski tensors have been applied to characterize anisotropy they highlight the potential of this method to characterize the structure of materials.

Methodology:

Based on the more general forms of Hadwiger (1957) they extend the framework of scalar Minkowski functionals to Minkowski vectors and tensors. By introducing a general notation valid for all Minkowski functionals. This notation stems for the general integral geometric relation from which all other Minkowski functionals can be derived:

$$W_v^{r,s}(K) = \frac{1}{3} \int_{\partial K} G_v x^r n^s dA, v = 1, 2, 3 \text{ and } (r, s) = (2, 0), (1, 1) \text{ or } (0, 2)$$

The above relationship is valid only for the given set of exponents and is zero otherwise. The function G_v has following form:

$$G_v = \begin{cases} 1, & \text{for } v = 0 \\ 1, & \text{for } v = 1 \\ \frac{\kappa_1 + \kappa_2}{2}, & \text{for } v = 2 \end{cases}$$

These tensors can be categorized into two classes: translation covariant i.e. their measurement depends on a reference location (often an area or volume centroid is chosen) and translation invariant tensors. For closed surfaces or discrete bodies, the translation covariant tensors are well defined and may be used extract shape information.

Conclusion:

While Schröder et al. have not discovered a whole new class of image morphological descriptors, they have provided a mathematical framework that links many integral geometric relationships that occur in physical processes. This framework provides the basis to evaluate these tensorial descriptors where 2D or 3D images of the structures are available to be used to characterize the distribution of structuring elements of random materials.

Comments:

The theory surrounding Minkowski tensors is rich, and many applications could be considered. Especially the large variety of translation covariant Minkowski tensors could be useful to describe physical or chemical processes in porous media where closed bodies occur e.g. the formation of droplets in capillary trapping or the shape of foam in enhanced oil recovery processes. Their integration into a new class of property models could allow incorporation of orientational information in improved material models.

Transactions-Institution of Chemical Engineers 15. Institution of Chemical Engineers: 150–66. Doi: 10.1016/S0263-8762(97)80003-2.

Year: 1937

Title: Fluid Flow through Granular Beds

Author(s): Carman, P. C.

Contribution:

Carman's publication presents the most detailed and complete resource of experimental and theoretical results for the estimation of permeability in granular media in his time. Starting with the initial experiments of Darcy, Carman compiles an extensive set of data and conclusions from before and after Kozeny's seminal work. Other approaches are highlighted where dimensionless groups provide good results in predicting the permeability of beds of spherical grains.

Methodology

This publication is an extensive comparative literature review encompassing a broad variety of experimental and theoretical results on the estimation of permeability. Each approach is carefully examined and evaluated with respect to other published results highlighting the importance of each presented publication.

Conclusion:

An invaluable compendium of analytical and theoretical results on permeability estimation.

Comments:

Many of the results presented stem from publications written in English. While Kozeny's publication is written in German, there exists a large variety of results that have gone unnoticed in this context and are not mentioned in the work of Carman.

Journal of Physics: Condensed Matter 17 (9): S503–34. doi:10.1088/0953-8984/17/9/014.
Year: 2005

Title: Fluids in Porous Media: A Morphometric Approach

Author(s): Mecke, K., and C. H. Arns

Contribution:

The authors present a morphological approach to characterize properties of porous media and their contained fluids. They first introduce the theory of scalar Minkowski functionals in the context of material properties. They highlight the important link between integral geometric relationships and the surface and volume integrals that occur in the mathematical description of processes in porous media.

Methodology

The authors first introduce the general concept of Minkowski functionals. In three dimensions these are the volume, surface area, integral of mean curvature and Euler characteristic. These are derived from Hadwiger's theorem which states that the global morphology of a binary material can be described by the set of scalar Minkowski measures. These morphological relations allow the formulation of material models for effective or average properties using scalar Minkowski functionals. Modeling approaches such as the Boolean model are introduced and used to generate realizations of Micro-CT images based on measured scalar Minkowski functionals. By evaluating two-point probability functions for each model, they estimate a goodness of fit for each of the proposed modeling approaches.

Conclusion:

The authors conclude that a combination of Minkowski measures and two-point probability functions allow for the most realistic visual reproduction of porous media but leave work on future hybrid models as an open problem. Their model for the shear modulus of vuggy carbonates is a promising result in the context of geological applications. Their derivation of capillary condensation is an inspiring approach to link morphological measures to physical processes and highlights their importance in the context of single and multi-phase flow in porous media.

Comments:

While Hadwiger's theorem states that material morphology can be uniquely described on a global level, this is not the case for the local scale as models that are conditioned with respect to the global scalar Minkowski functionals often show very different morphology while having similar effective properties.

This publication is underrated and maybe undiscovered in its importance. There are many valuable approaches defined here that deserve to be carefully reexamined in the context of modern geomodeling approaches and open problems in the multi-phase flow behavior in porous media and enhanced oil recovery methods.

Transport in Porous Media 1: 241–69. doi:10.1007/BF00238182.
 Year: 1986

Title: Macroscopic Modelling of Transport Phenomena in Porous Media. 2: Applications to Mass, Momentum, and Energy Transport.

Author(s): Bear, J., Y. Bachmat.

Contribution:

In their first publication, the authors describe a volume averaging approach to defining the equations of flow and transport in porous media. This requires the definition of a so-called representative elementary volume over which the equations can be solved. They provide a rigorous mathematical derivation of the equations governing the transport of mass, exchange of momentum and energy. This allows them in their second volume to apply their general theory to a set of relevant applications. These include heat conduction, thermo-elastic as well as diffusion problems. The authors derive a general equation for single-phase flow in porous media that allows an estimate of the permeability tensor of a material to be obtained.

$$k_{ij} = \frac{\phi^3}{C_\alpha S_\nu^2} \alpha_{il}^{-1} T_{lj}^* = \frac{\phi^3}{C_\alpha S_\nu^2} \alpha_{ij}^{-1} \frac{1}{\tau^2}$$

Methodology:

By applying a macroscopic momentum balance to a representative elementary volume over which the equations governing single-phase flow are averaged, the authors derive a general expression of the permeability of a porous medium. This equation includes two factors that characterize the orientation and tortuosity of the pore space.

$$\begin{aligned} \alpha_{ij} &= \delta_{ij} - \frac{1}{S_{\alpha\beta}} \int n_\alpha^i n_\alpha^j dA \\ T_{ij}^* &= \frac{1}{\phi V} \int x^i n^j dA \end{aligned}$$

As has been shown in the methodology section, these integral geometric measures are directly related to tensorial Minkowski functionals. For simplified cases of isotropic media, these equations simplify to the well-known Kozeny-Carman equation.

Conclusion:

The authors presented a new analytical expression to predict the permeability from derived material properties. While their method contains two integral geometric expressions to characterize the pore-grain interface and the tortuosity at the REV scale, the authors give no indication on how these properties could be measured. With the advent of modern Micro-CT methods measurement of these integral geometric relations for actual pore-grain surfaces has become possible and is evaluated as part of this thesis.

Comments:

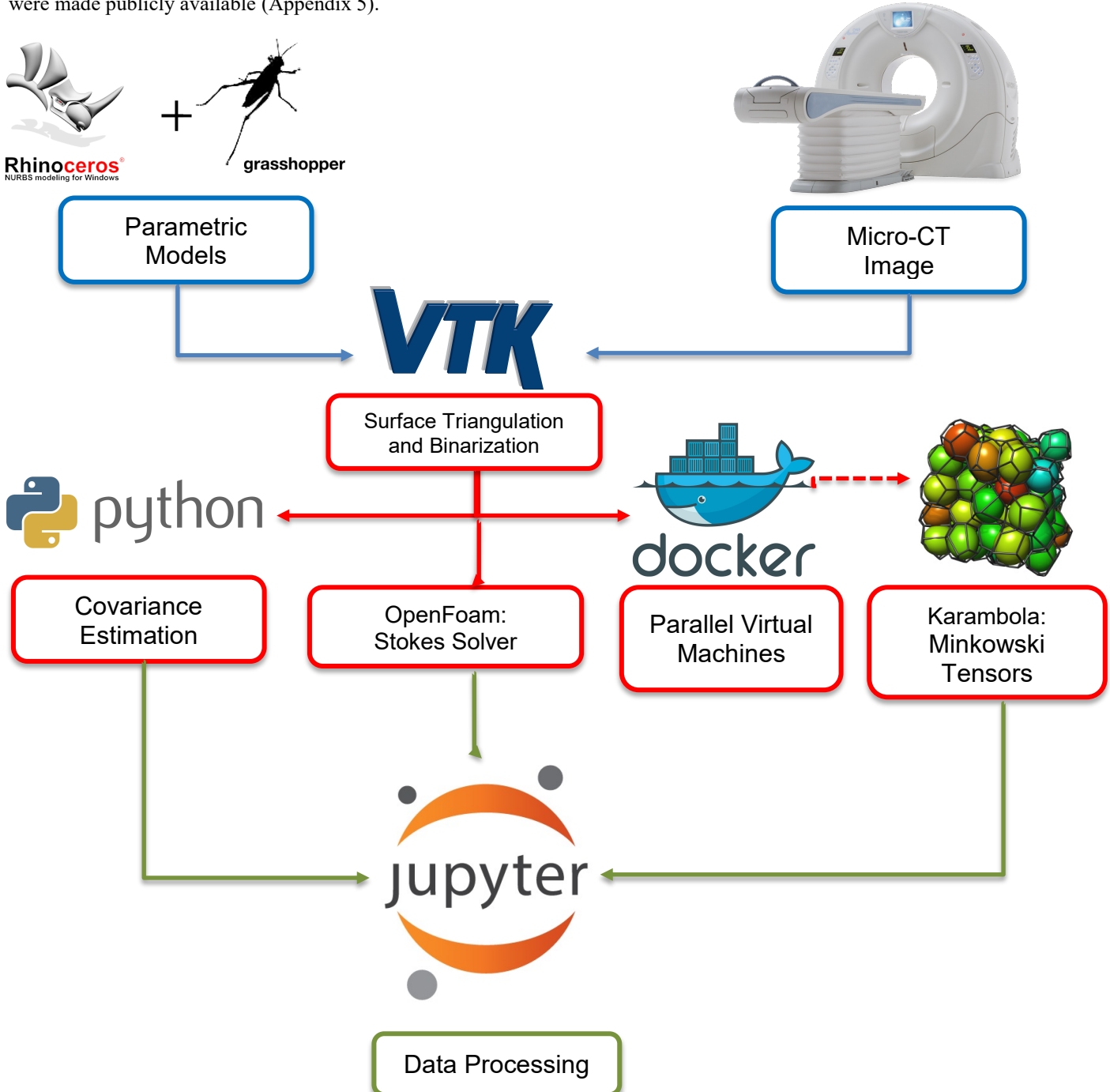
Mathematically complex and convoluted, could easily be split into multiple publications. Their general theory provides many relevant examples and approaches to solving complex physical processes in porous media.

Appendix 2: Workflow description

The following section describes the general workflow used to generate parametric models, compute covariance and Minkowski tensors from binary representations as well as the computation of directional permeability of the individual samples.

We can distinguish two sources of data in this thesis: parametric models and Micro-CT images of sedimentary or artificial rock. Parametric models were created using a NURBS (Non-Uniform-Rational-B-Spline) based modeling tool Rhino and a parametric modeling suite Grasshopper. The workflow used for parametric modeling can be found in appendix 3.

The VTK toolkit was used to extract triangulated surfaces from Micro-CT samples of sedimentary rock and to create binary representations of the parametric models. Triangulated surface representations were used as input for the Karambola software that allows computation of scalar, vectorial and tensorial Minkowski functionals and is presented by (Schröder-Turk et al. 2013) (Appendix 4). By using the virtualization toolkit Docker, numerous virtual machines were used to parallelize the computation of Minkowski valuations on a cluster of desktop PCs. The programming language Python was used to compute covariance from binary representations (Pant 2016). An OpenFoam implementation of the algorithms described by (Mostaghimi, Blunt, and Bijeljic 2013) has been applied to compute numerical estimates of the permeability in three spatial directions. All data was analyzed, and graphs created using Jupyter notebooks. All algorithms and datasets were made publicly available (Appendix 5).

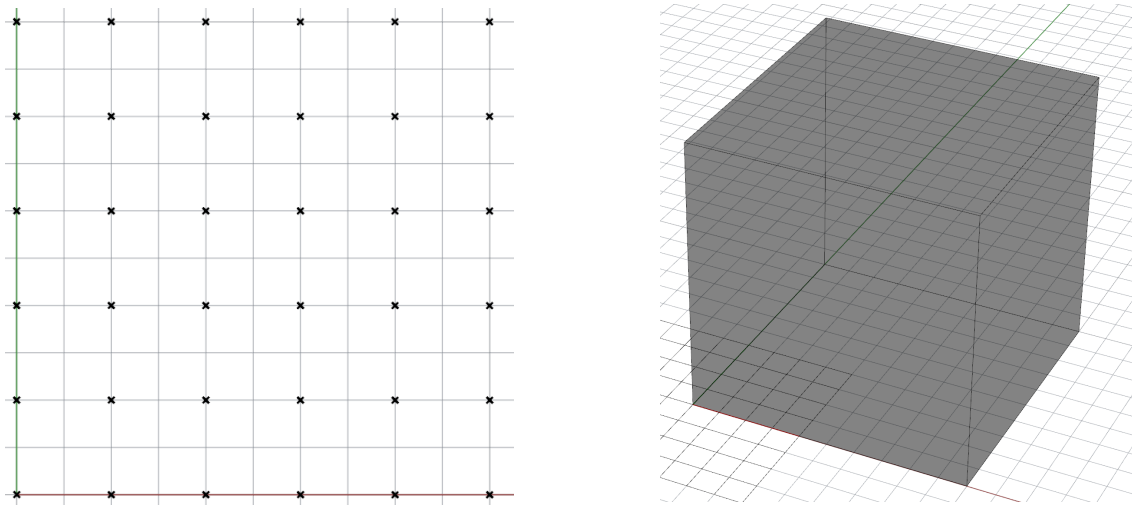


Appendix Figure 1: Data generation and processing workflow used to estimate covariance and Minkowski tensors from Micro-CT data.

Appendix 3: Parametric pore space modeling

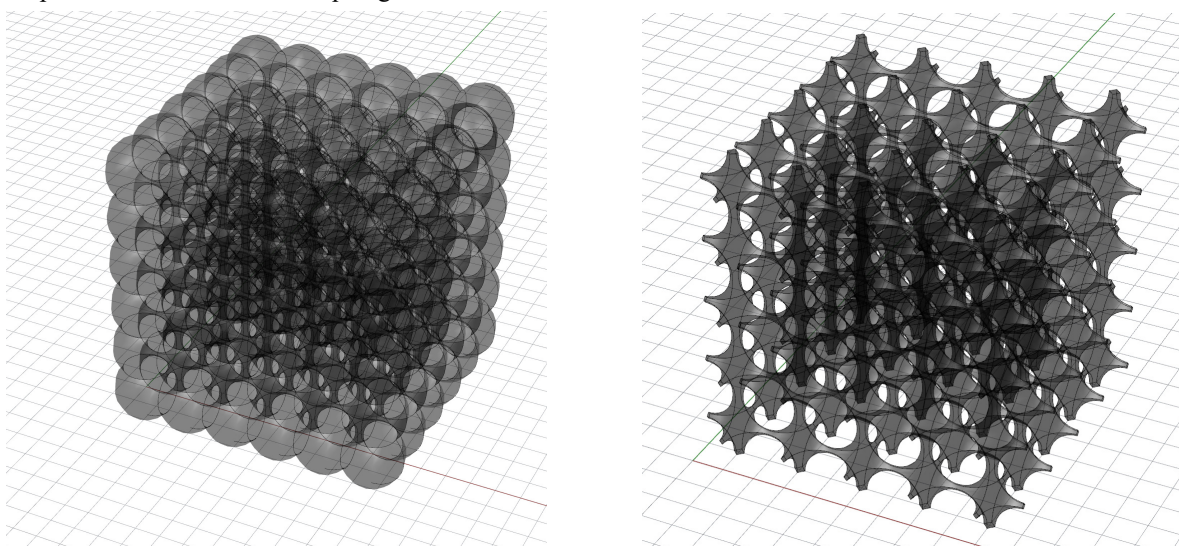
Analyzing the behavior of statistical and image morphological measures for various rock samples is a challenging task as the geometry of the existing pore space often arises from physical and chemical processes. These can be related to stochastic processes such as the Boolean model (Torquato 2002). Due to the stochastic nature of the models, analysis of the statistical measures requires evaluation using an ensemble of realizations. While this approach gives a better understanding of the average behavior of the evaluated measures, a deterministic modeling approach combined with evaluation of a known parameter space can provide insight into the fundamental behavior of individual models.

Here we describe a set of parametric models based on a deterministic equally spaced soft sphere and later ellipsoidal grain model. The parametric modeling tool Grasshopper was used to create parametric models arising from a set of linked modules. This allows an intuitive and modular workflow for model generation and parametrization. All models were created using Rhino 5.0 and the Grasshopper module.



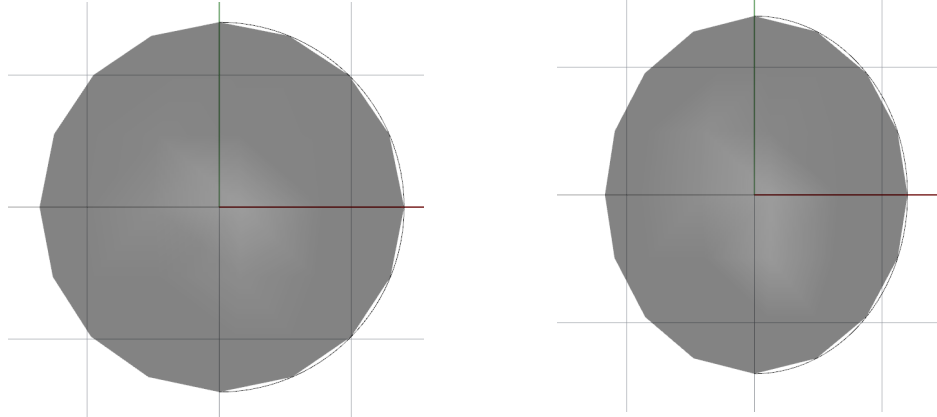
Appendix Figure 2: Left: Input grid of points representing the centroids of the ellipsoidal or spherical grains. Right: Box volume from which the pore space is extracted using Boolean operations.

Each model is comprised of a grid of points equally spaced on a 3D lattice. These equally spaced lattice points act as centers for spherical or ellipsoidal grains. Each grain is defined by a center vertex and a radius. Ellipsoidal grains are created by applying a uniaxial or biaxial scaling transformation. Each sphere is represented as a NURBS (Non-Uniform Rational B-Spline) object and accounts for a single grain. The number of grains in each direction can be varied independently. For this study, an equal number of grains were placed to create a cubic grid of spheres with equal edge lengths. This allows a similar representation as the available images of sedimentary rock samples and eliminates the need to compensate for bias due to unequal grid sizes in each direction.



Appendix Figure 3: Left: Union of spheres representing the grains of a parametric sample. Right: Pore grain interface after applying Boolean operations to extract the boundary surface.

A number of Boolean operations were applied to extract the surface representation of the pore space. Due to the overlap of the soft spheres, a union of all grains allows the grain space to be represented. A surrounding box volume is introduced to represent the void space. Boolean subtraction of the grains from the void space results in a representation of the intergranular void space. Finally, Boolean intersection of the void space and the bounding surfaces results in a surface representation of the boundary surfaces of the grain and void space. These surfaces are open and periodic in the Cartesian directions closely mimicking the behavior of perfect isotropic arrangements of spherical grains. This parametric representation is similar to triply periodic media such as Schwartz's P surface.

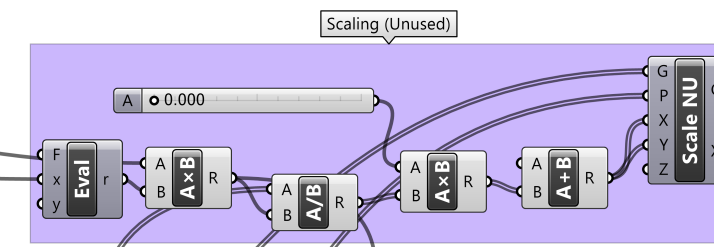
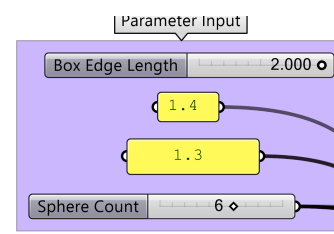
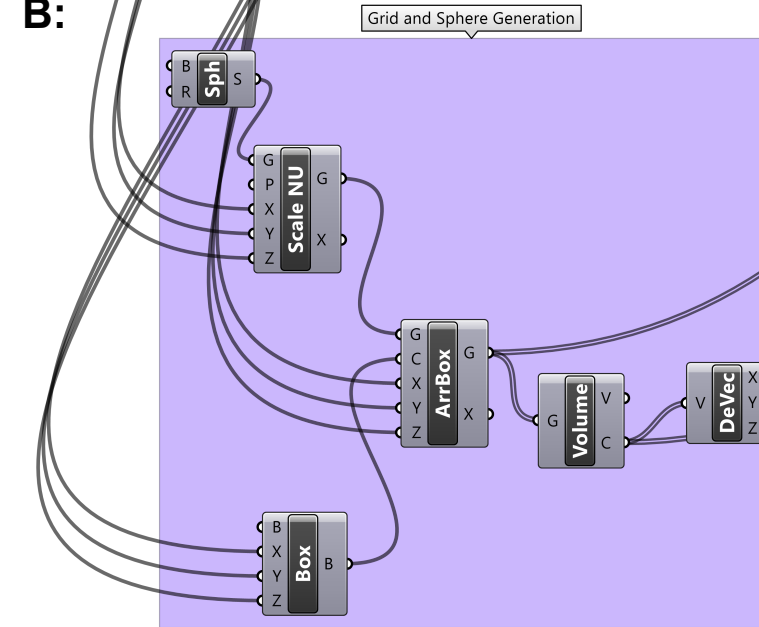
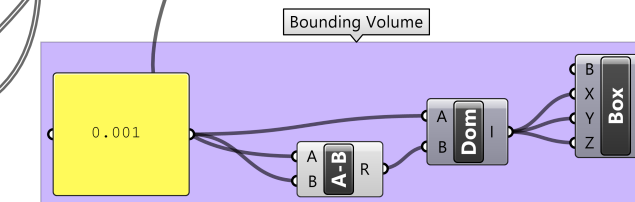
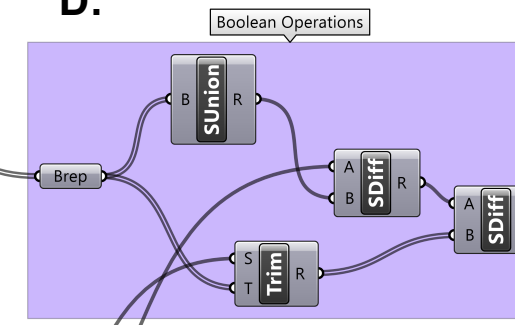
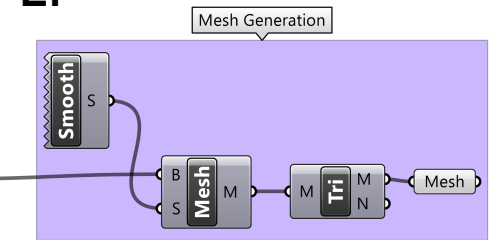


Appendix Figure 4: Left representative spheroid grain with radius 1.4 [m]. Right: Ellipsoidal grain with reduced radius of 1.2 [m] in the x-y plane. (x-z plane shown)

Deterministic scenarios were created to evaluate statistical as well as morphological image characteristics and to relate these to their respective flow properties. Isotropic models have been defined with radii ranging from 1.2 to 1.4 [m]. These lengths are later scaled to match the typical size of Micro-CT samples. To evaluate the effect of anisotropy two models have been created with ellipsoidal grains. The ellipsoidal grains have been stretched in two of three directions leading to anisotropic behavior in the z-direction, with the x-y plane showing similar behavior (Appendix 6).

Minkowski properties of these parametric models can be directly measured on the triangulated surface representation by export via a suitable file format. Models were first exported to STL mesh files and later converted to the POLY file format required by the Minkowski tensor library Karambola (Schröder-Turk et al. 2013). An intermediate binarization step was necessary to evaluate the covariance of these parametric models. To convert a surface representation to a binary voxel image, the Visual Tool Kit was used. The VTK library consists of industry standard algorithms for computations on large image datasets and surface representations as they are commonly applied in environments where CT imaging is applied, such as bioengineering or medical applications.

To convert the STL surface representations the vtk algorithm vtkPolyDataToImageStencil and vtkImageStencil were applied. To convert open surfaces, it is necessary to first apply a hole closing on all open edges before converting to binary format. This removes introduced artifacts in the images and allows a highly resolved representation of the surfaces. To reintroduce periodic boundaries single voxel slices in each Cartesian direction were removed that have been added as a padding by the binarization algorithm. All images were specified to have 500 voxels in each direction matching the dimensions of the available image samples of sedimentary rock. All binary images were output as TIFF image stacks for later processing and evaluation. For computation of permeability, each binary representation was converted to a raw 8-bit format with a voxel resolution of $2 \mu\text{m}$. While this resolution has no physical context it is in the range of the resolution of typical Micro-CT images and allows for later comparison of permeability estimates in typical mD or Darcy units. A full analysis of covariance, Minkowski measures and permeability is presented in appendix 6.

A:**B:****C:****D:****E:**

Appendix Figure 5: A: Input parameters used to construct the parametric model. Two radii can be input, here 1.4 denotes the radius in the z-direction and 1.3 the radius in the x-y plane. Sphere count determines how many spheres are placed in each direction to create the array of spheroids. B: Modules creating the grid of spheres from the input array. C: Box volume generation modules from which the pore-grain interface is extracted. D: Boolean operations acting on the box volume and set of spheres. E: Mesh triangulation of the pore-grain interface and output to file.

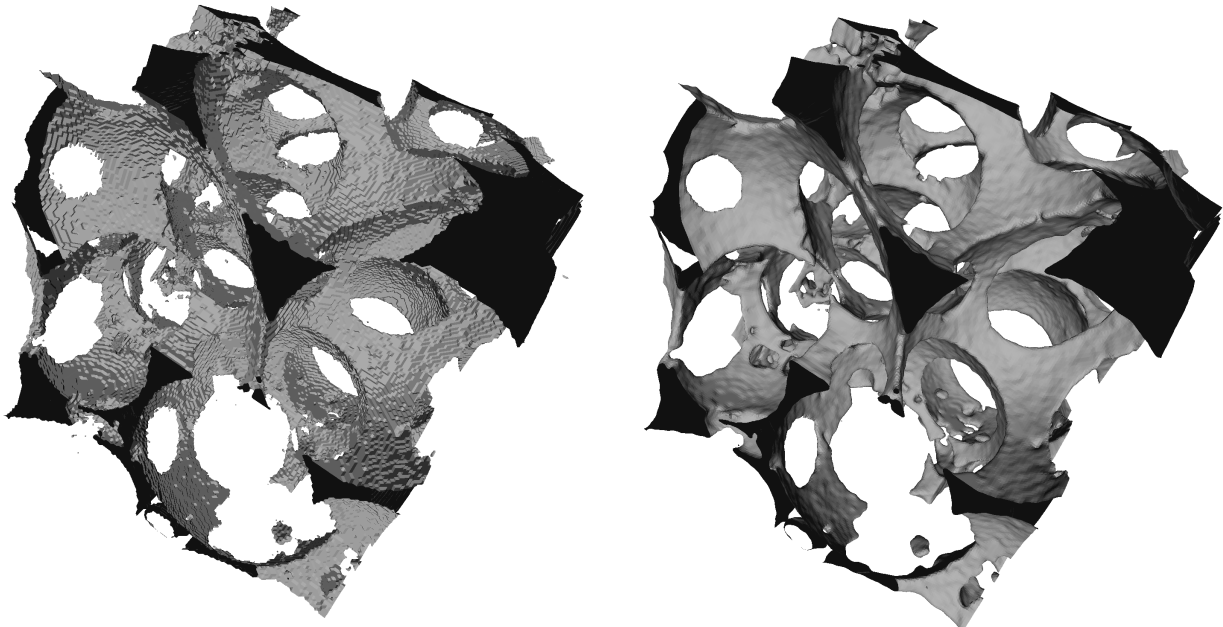
Appendix 4: Interface extraction from binary Micro-CT images

While Minkowski tensors are well defined on parametric surfaces where analytical results for scalar and tensorial Minkowski functionals exist (Schröder-Turk et al. 2013; Hörrmann and Weil 2015), approximations of the Minkowski tensors for arbitrary surfaces can be computed from discretized surface representations.

The surface integrals in the definition of the first and second translation invariant Minkowski tensor are discretized as a sum over finite surface elements (Equation 8). A triangulated surface representation is necessary as an input for the available implementation in the Minkowski functional software library Karambola (Schröder-Turk et al. 2013). The classical Marching Cubes algorithm was used to extract an explicit triangulated surface representation of the boundary between grain and void space. Two approaches to extract the boundary surfaces were evaluated:

The first approach assumes that the image has not been segmented using image segmentation methods and is available as a grayscale image. As no raw data was accessible in this study, a 3-dimensional Gaussian filter with a standard deviation of $\sigma=1.0$ was applied to the segmented images, before applying Otsu's thresholding method to convert the image to a binary representation. For this approach it is key that binary images are required to later compute statistical measures such as covariance as well as the permeability. Therefore, the image after thresholding using Otsu's method should be used for all later computations. It is important to note that this would be the standard procedure in analyzing Minkowski tensors or any statistical or numerical measure on the binary and surface representations.

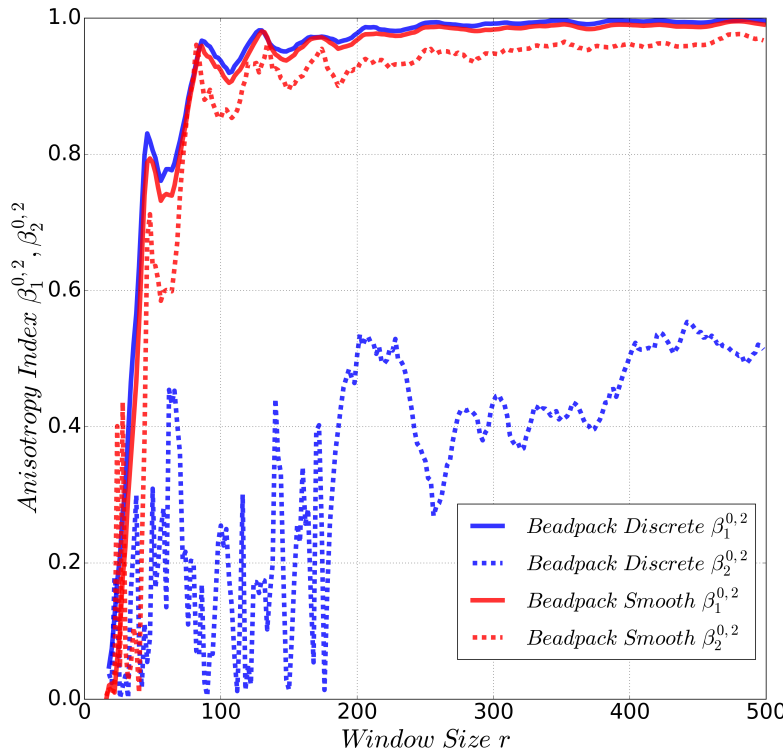
The second approach assumes that the image has been filtered and segmented into binary form as has been the case for the available Micro-CT images. The boundary surface is extracted from the binary voxel representation using a discrete Marching Cubes algorithm. This approach allows an almost exact representation of the given binary surface. All results presented in this thesis apart from the following comparison have been computed using the discrete Marching Cubes method.



Appendix Figure 6: Comparison of two surface triangulations of the Ketton sample. Left: The surface has been directly extracted from the input dataset and shows a rough surface topology. Right: Smoothed sample after application of a Gaussian blur and thresholding using Otsu's method.

A first general observation can be made on the smoothness of the resulting meshes (Appendix Figure 6). The surfaces extracted after applying Otsu's method are very smooth and have few edges. The discrete Marching Cubes algorithm leads to much rougher surfaces but a more exact representation compared to the binary image.

For the resulting anisotropy indices $\beta_1^{0,2}$ we can see for the beadpack sample (Appendix Figure 7) both approaches lead to almost the same graph. For the second anisotropy index $\beta_2^{0,2}$ we observe considerable mesh dependency. For smoothed meshes this measure may be used to gain insight on the curvature distribution of the pore-grain interface. For this study only the first anisotropy index was considered to have a consistent representation of the boundary across the workflow. The mesh dependency is expected as the application of the Gaussian filter changes the shape and therefore surface representation of the pore space. We therefore recommended to apply the Minkowski tensor analysis after segmentation of the binary image and if necessary evaluate the variability of the Minkowski measures as a function of smoothing applied to the resulting triangulated interface.



Appendix Figure 7: Comparison of the two anisotropy indices $\beta_1^{0,2}$ and $\beta_2^{0,2}$ for smooth and rough triangulations of the pore-grain interface. Considerable mesh dependency can be observed for the second anisotropy index.

Both methods, discrete and smooth, were implemented using the Python wrapper library of the Visual Tool Kit VTK which provides industry standard algorithms for surface extraction from binary voxel images. Specifically, vtkDiscreteMarchingCubes and vtkMarchingCubes were used to compute the triangulated surfaces.

An important issue when dealing with any discretized surface or volume representation such as triangular or tetrahedral meshes is mesh quality. The computation of Minkowski tensors on triangular meshes is not sensitive to the shape or of the triangular elements as opposed to e.g. finite element computations. Meshes that have non-manifold vertices cannot be used for the computation of the Minkowski functionals. A comparison of various libraries showed that triangular meshes created with VTK consistently show no non-manifold vertices. This was a critical step in this study due to a large number of meshes required (~250 per graph), any necessary manual corrections would have made this impossible.

An additional factor that has to be considered is the need for improved software allowing the computation of Minkowski tensors on very large meshes. Each mesh extracted at full image size requires 1.5 gigabytes of hard disk space. Evaluating the anisotropy indices for a range of values requires multiple hundred gigabytes of disk space which could be reduced considerably using modern storage and compression algorithms.

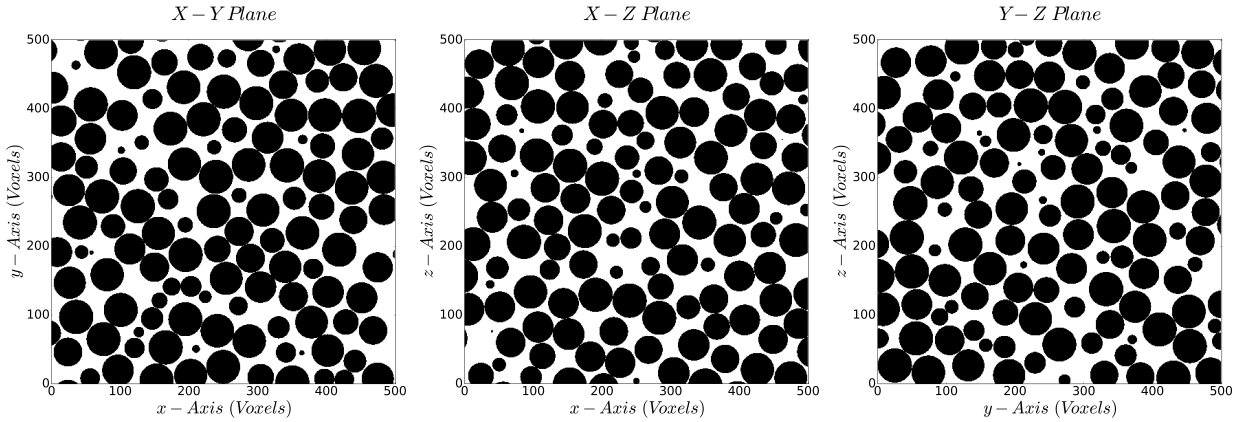
Appendix 5: Reproducibility and software documentation

Reproducibility of results is an important aspect of the scientific process. Reproduction of critical results by third parties allows validation of proposed methods and workflows. Therefore, emphasis was placed on making the results and methods used in this thesis reproducible and publicly available. Due to restrictions on formatting, the thesis itself is not reproducible but all figures showing numerical results can be reproduced using the provided Jupyter notebooks. All input data and computed results are freely available and may be used with proper citation of this publication. Software, results, and figures have been added to the versioning system GitHub and are available under the following link: https://github.com/LukasMosser/MSc_Thesis

Appendix 6: Sample results and analysis

Sample 1: Beadpack

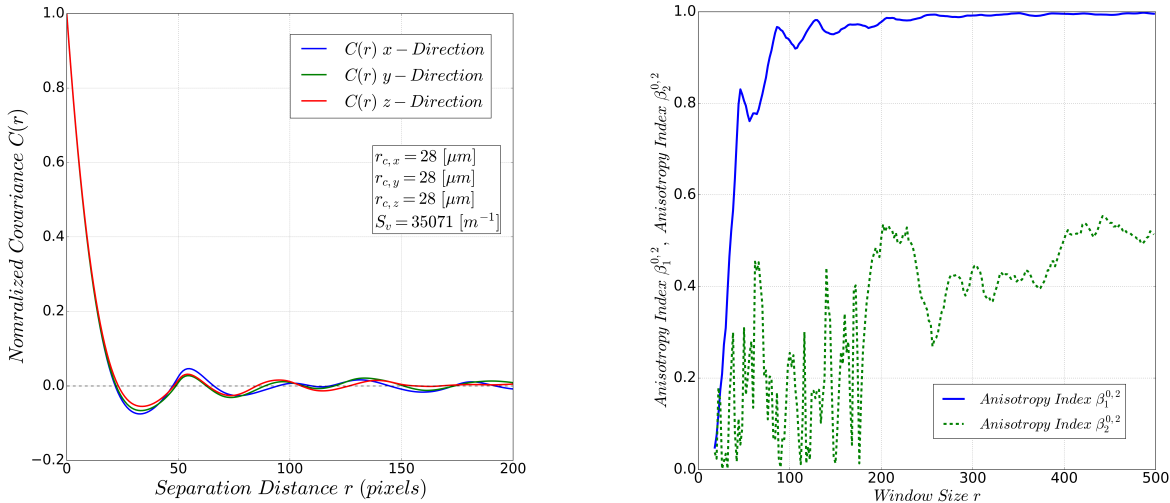
Orthogonal Image Projections:



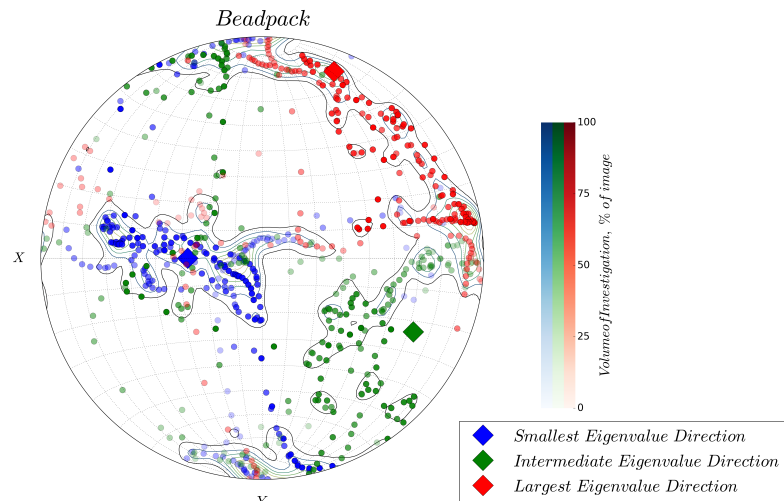
Appendix Figure 8: Orthogonal views of the beadpack image. Views seen from front of sample.

Sample Analysis:

Artificial beadpack sample. Grain diameter $100 \mu\text{m}$. The covariance resembles the hard-sphere model in all directions. Isotropic behavior is observed in all directions. Anisotropy index $\beta_1^{0,2}$ shows isotropic behavior above $500 \mu\text{m}$. The eigenvectors are isotropic across all length scales.



Appendix Figure 9: Left: Normalized directional covariance of the beadpack sample. Right: Anisotropy indices derived from Minkowski tensor functionals.

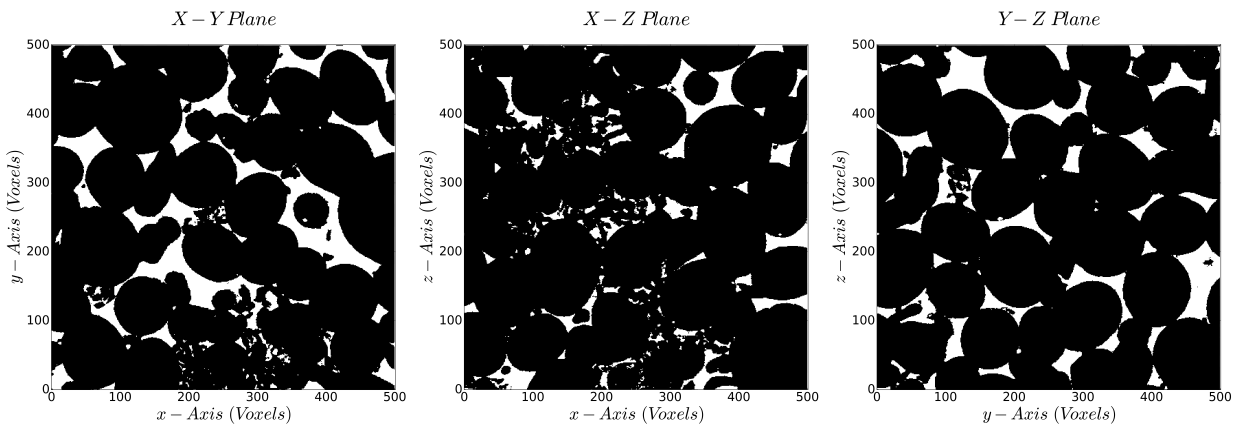


Appendix Figure 10: Stereonet projection of eigenvectors of Minkowski tensor $W_1^{0,2}$ of the beadpack sample.

Results Summary		
Image Name	Beadpack	
Rock Type	Artificial	
Property	Value	Unit
Image Resolution	2.0	[μm]
Image Dimensions	(500, 500, 500)	(Nx, Ny, Nz) [voxel]
Covariance Analysis Results		
Porosity	0.36	[\cdot]
Directional Characteristic Pore Size [$r_{c,x}, r_{c,y}, r_{c,z}$]	28,28,28	[μm]
Average Characteristic Pore Size \bar{r}_c	28	[μm]
Specific Surface Area	35071	[m^{-1}]
Minkowski Tensor Analysis		
Normalized Minkowski Functional $\widehat{W}_1^{0,2}$	$\begin{bmatrix} 0.333 & 0 & 0 \\ 0 & 0.334 & 0 \\ 0 & 0 & 0.332 \end{bmatrix}$	[\cdot]
Normalized Minkowski Functional $\widehat{W}_2^{0,2}$	$\begin{bmatrix} 0.394 & -0.07 & 0.02 \\ -0.07 & 0.254 & 0.009 \\ 0.02 & 0.009 & 0.350 \end{bmatrix}$	[\cdot]
Anisotropy Index $\beta_1^{0,2}$	0.99	[\cdot]
Anisotropy Index $\beta_2^{0,2}$	0.51	[\cdot]
Permeability Computation Results		
Effective Porosity	0.36	[\cdot]
Directional Permeability	$\begin{bmatrix} 6.184 & - & - \\ - & 6.326 & - \\ - & - & 6.197 \end{bmatrix}$	[Darcy]

Sample 2: Ketton

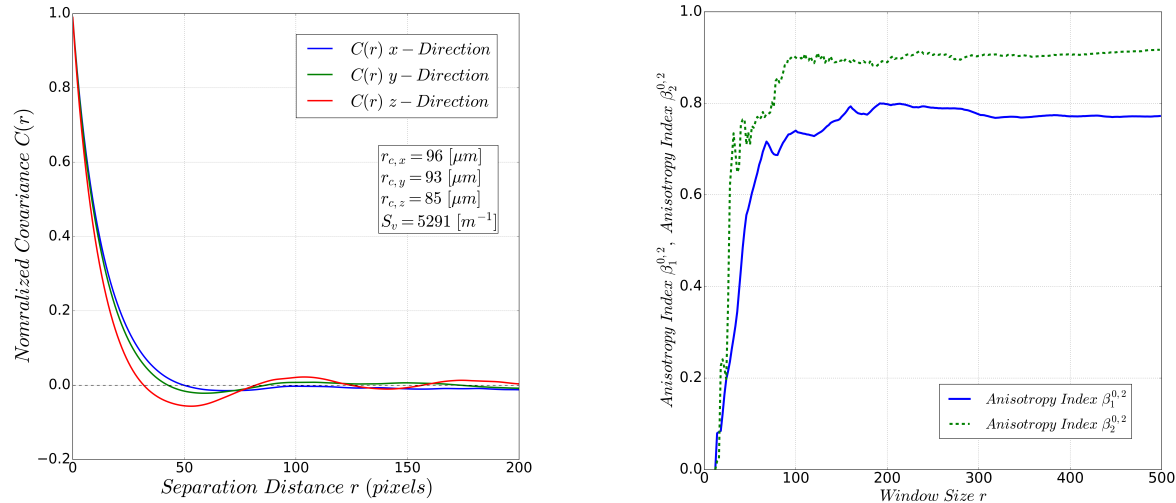
Orthogonal Image Projections:



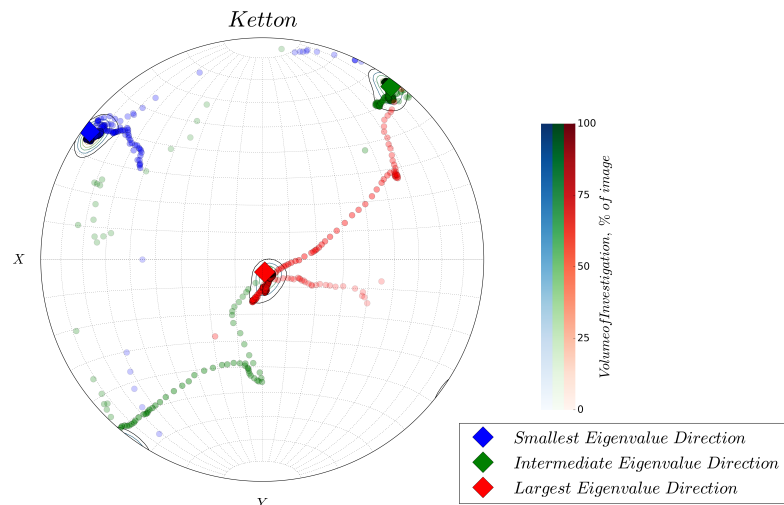
Appendix Figure 11: Orthogonal views of the Ketton image. Views seen from front of sample.

Sample Analysis:

Oolitic limestone sample with distinct ellipsoidal grains. The covariance resembles the hard-sphere model in the z-direction. Possible preferential cementation of grains. Anisotropy index $\beta_1^{0,2}$ shows isotropic behavior above 1800 μm . Stereonet indicates that preferential orientation of pore-grain surface is reached at small sample volumes. Permeability reduced in z-direction. This is in agreement with covariance (characteristic pore size) and $W_1^{0,2}$ eigenvalues.



Appendix Figure 12: Left: Normalized directional covariance of the Ketton sample. Right: Anisotropy indices derived from Minkowski tensor functionals.

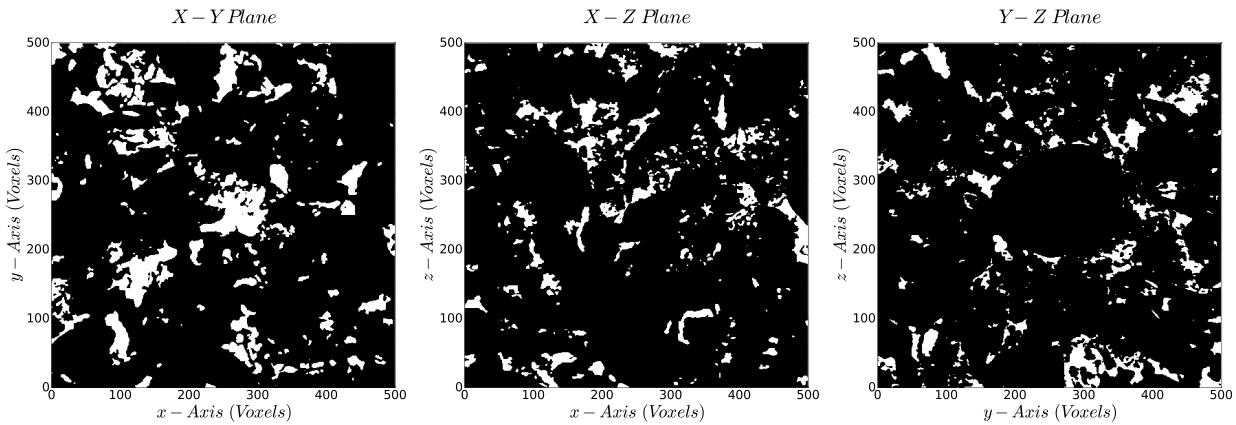


Appendix Figure 13: Stereonet projection of eigenvectors of Minkowski tensor $W_1^{0,2}$ of the Ketton sample.

Results Summary		
Image Name	Ketton	
Rock Type	Carbonate	
Property	Value	Unit
Image Resolution	6.00012	[μm]
Image Dimensions	(500, 500, 500)	(Nx, Ny, Nz) [voxel]
Covariance Analysis Results		
Porosity	0.13	[\cdot]
Directional Characteristic Pore Size [$r_{c,x}, r_{c,y}, r_{c,z}$]	96,93,85	[μm]
Average Characteristic Pore Size \bar{r}_c	85	[μm]
Specific Surface Area	5291	[m^{-1}]
Minkowski Tensor Analysis		
Normalized Minkowski Functional $\widehat{W}_1^{0,2}$	$\begin{bmatrix} 0.306 & 0.025 & -0.003 \\ 0.025 & 0.334 & 0.004 \\ -0.003 & 0.004 & 0.331 \end{bmatrix}$	[\cdot]
Normalized Minkowski Functional $\widehat{W}_2^{0,2}$	$\begin{bmatrix} 0.322 & 0.005 & 0 \\ 0.005 & 0.330 & 0 \\ 0 & 0 & 0.348 \end{bmatrix}$	[\cdot]
Anisotropy Index $\beta_1^{0,2}$	0.77	[\cdot]
Anisotropy Index $\beta_2^{0,2}$	0.92	[\cdot]
Permeability Computation Results		
Effective Porosity	0.13	[\cdot]
Directional Permeability	$\begin{bmatrix} 5.103 & - & - \\ - & 3.456 & - \\ - & - & 3.261 \end{bmatrix}$	[Darcy]

Sample 3: Estaillades

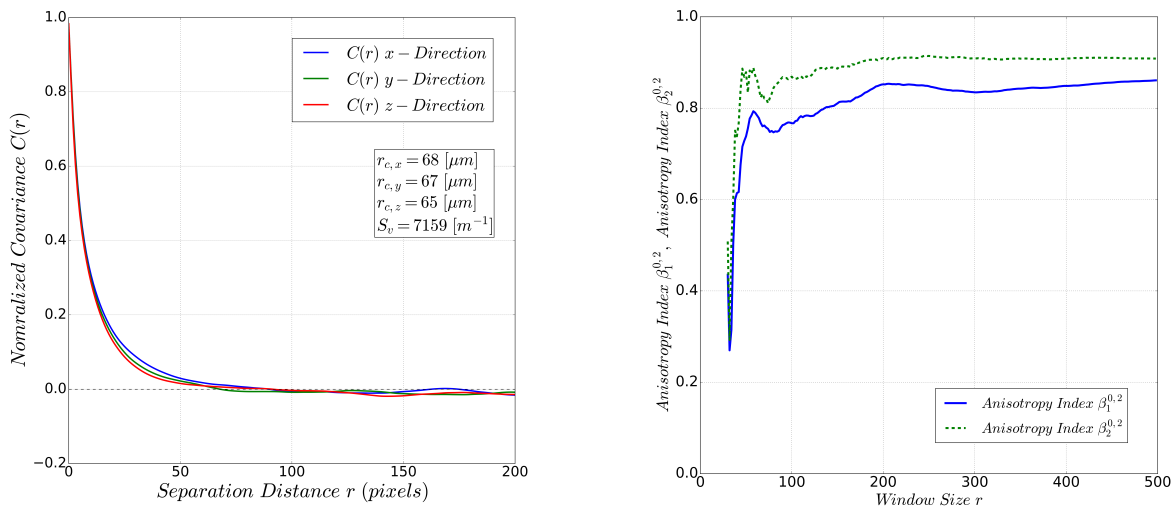
Orthogonal Image Projections:



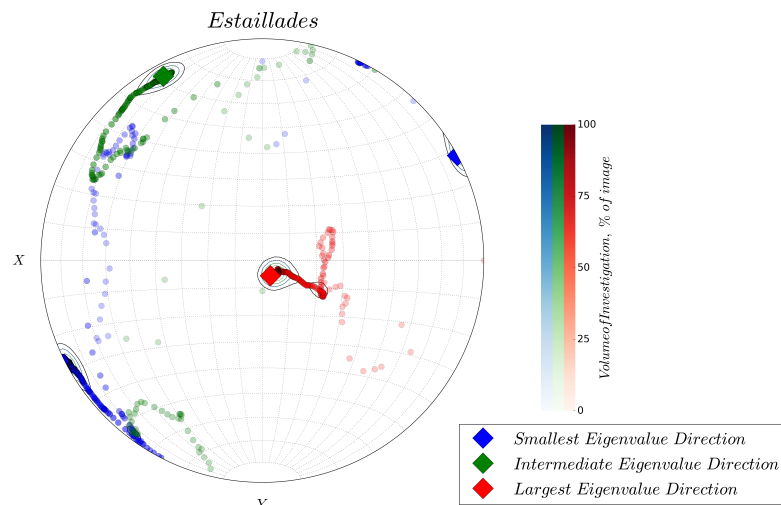
Appendix Figure 14: Orthogonal views of the Estaillades image. Views seen from front of sample.

Sample Analysis:

Complex carbonate with biogenic structures. No clear stabilization of covariance in any direction. No stabilization in anisotropy index $\beta_1^{0,2}$. The stereonet shows multiple traced paths and no clear orientation indicating that an REV has not been reached or a second subscale in the image is present (~ 200 voxels).



Appendix Figure 15: Left: Normalized directional covariance of the Estaillades sample. Right: Anisotropy indices derived from Minkowski tensor functionals.

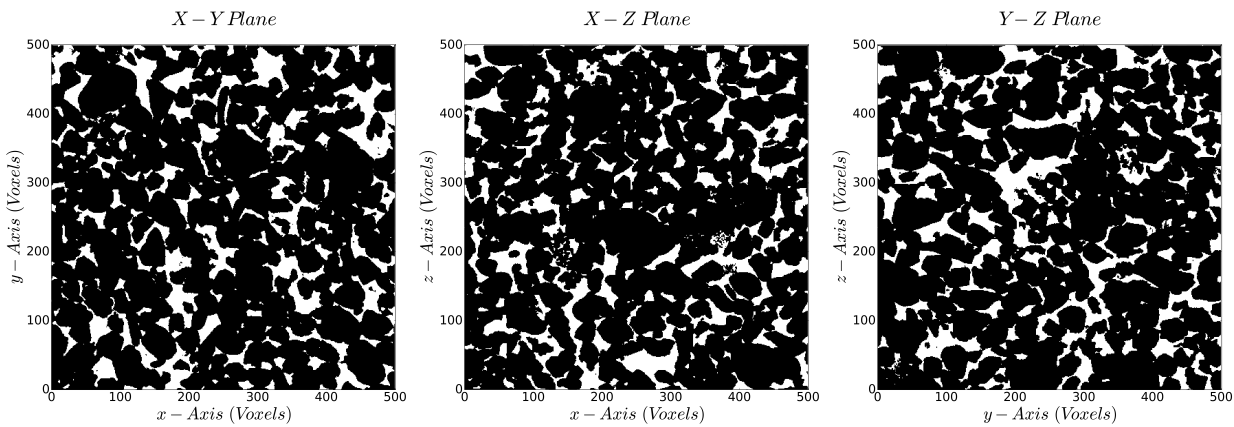


Appendix Figure 16: Stereonet projection of eigenvectors of Minkowski tensor $W_1^{0,2}$ of the Estaillades sample.

Results Summary		
Image Name	Estailles	
Rock Type	Carbonate	
Property	Value	Unit
Image Resolution	6.62272	[μm]
Image Dimensions	(500, 500, 500)	(Nx, Ny, Nz) [voxel]
Covariance Analysis Results		
Porosity	0.12	[\cdot]
Directional Characteristic Pore Size [$r_{c,x}, r_{c,y}, r_{c,z}$]	68,67,65	[μm]
Average Characteristic Pore Size \bar{r}_c	60	[μm]
Specific Surface Area	7159	[m^{-1}]
Minkowski Tensor Analysis		
Normalized Minkowski Functional $\widehat{W}_1^{0,2}$	$\begin{bmatrix} 0.315 & -0.004 & -0.002 \\ -0.004 & 0.320 & 0.004 \\ -0.002 & 0.004 & 0.364 \end{bmatrix}$	[\cdot]
Normalized Minkowski Functional $\widehat{W}_2^{0,2}$	$\begin{bmatrix} 0.323 & -0.003 & -0.002 \\ -0.003 & 0.324 & 0.001 \\ -0.002 & 0.001 & 0.353 \end{bmatrix}$	[\cdot]
Anisotropy Index $\beta_1^{0,2}$	0.86	[\cdot]
Anisotropy Index $\beta_2^{0,2}$	0.91	[\cdot]
Permeability Computation Results		
Effective Porosity	0.10	[\cdot]
Directional Permeability	$\begin{bmatrix} 0.157 & - & - \\ - & 0.075 & - \\ - & - & 0.117 \end{bmatrix}$	[Darcy]

Sample 4: Bentheimer

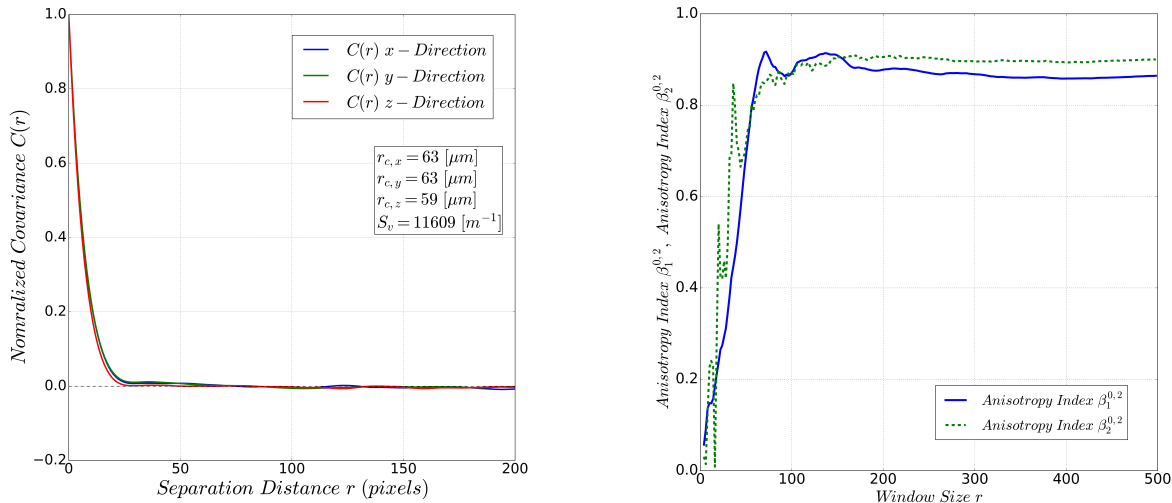
Orthogonal Image Projections:



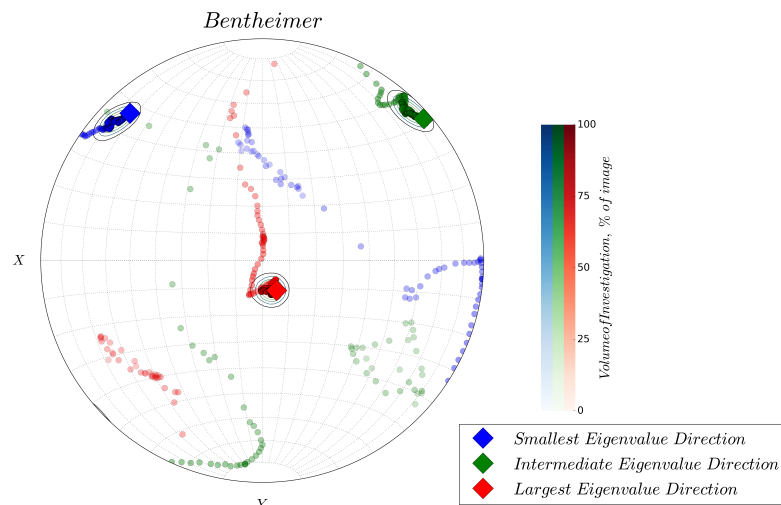
Appendix Figure 17: Orthogonal views of the Bentheimer image. Views seen from front of sample.

Sample Analysis:

Siliciclastic sandstone sample. Individual grains identifiable. The covariance resembles overlapping sphere model rather than the hard-sphere model. Possible cementation or packing due to angular grains. The anisotropy index indicates small anisotropy which correlates well with the covariance and the measured permeability having the lowest value of 2.3 Darcy in the z-direction.



Appendix Figure 18: Left: Normalized directional covariance of the Bentheimer sample. Right: Anisotropy indices derived from Minkowski tensor functionals.

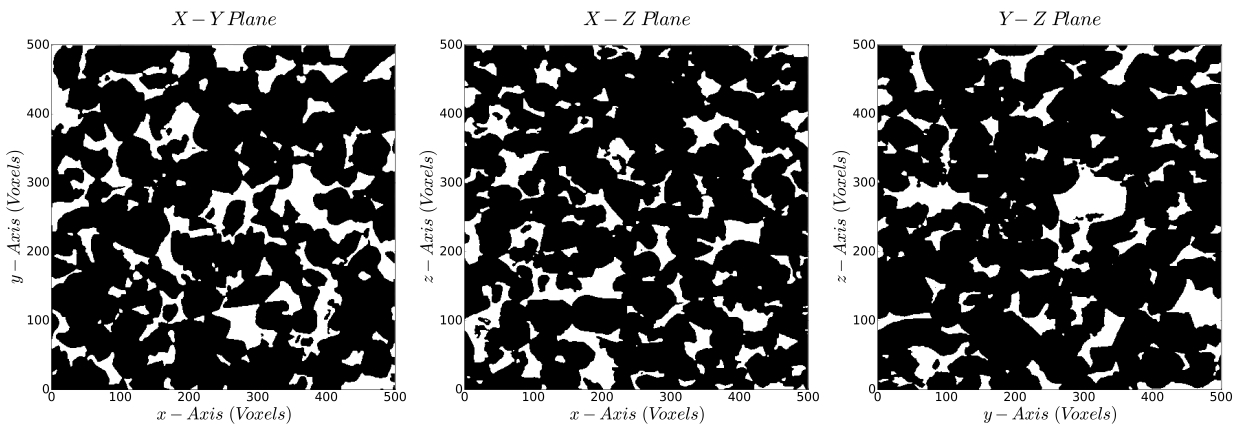


Appendix Figure 19: Stereonet projection of eigenvectors of Minkowski tensor $W_1^{0,2}$ of the Bentheimer sample.

Results Summary		
Image Name	Bentheimer	
Rock Type	Sandstone	
Property	Value	Unit
Image Resolution	6.007	[μm]
Image Dimensions	(500, 500, 500)	(Nx, Ny, Nz) [voxel]
Covariance Analysis Results		
Porosity	0.20	[\cdot]
Directional Characteristic Pore Size [$r_{c,x}, r_{c,y}, r_{c,z}$]	63,63,59	[μm]
Average Characteristic Pore Size \bar{r}_c	55	[μm]
Specific Surface Area	11609	[m^{-1}]
Minkowski Tensor Analysis		
Normalized Minkowski Functional $\widehat{W}_1^{0,2}$	$\begin{bmatrix} 0.321 & 0.008 & -0.005 \\ 0.008 & 0.321 & 0.008 \\ -0.005 & 0.008 & 0.357 \end{bmatrix}$	[\cdot]
Normalized Minkowski Functional $\widehat{W}_2^{0,2}$	$\begin{bmatrix} 0.324 & 0.004 & -0.002 \\ 0.004 & 0.334 & 0.006 \\ -0.002 & 0.006 & 0.331 \end{bmatrix}$	[\cdot]
Anisotropy Index $\beta_1^{0,2}$	0.86	[\cdot]
Anisotropy Index $\beta_2^{0,2}$	0.90	[\cdot]
Permeability Computation Results		
Effective Porosity	0.20	[\cdot]
Directional Permeability	$\begin{bmatrix} 2.779 & - & - \\ - & 2.867 & - \\ - & - & 2.329 \end{bmatrix}$	[Darcy]

Sample 5: Doddington

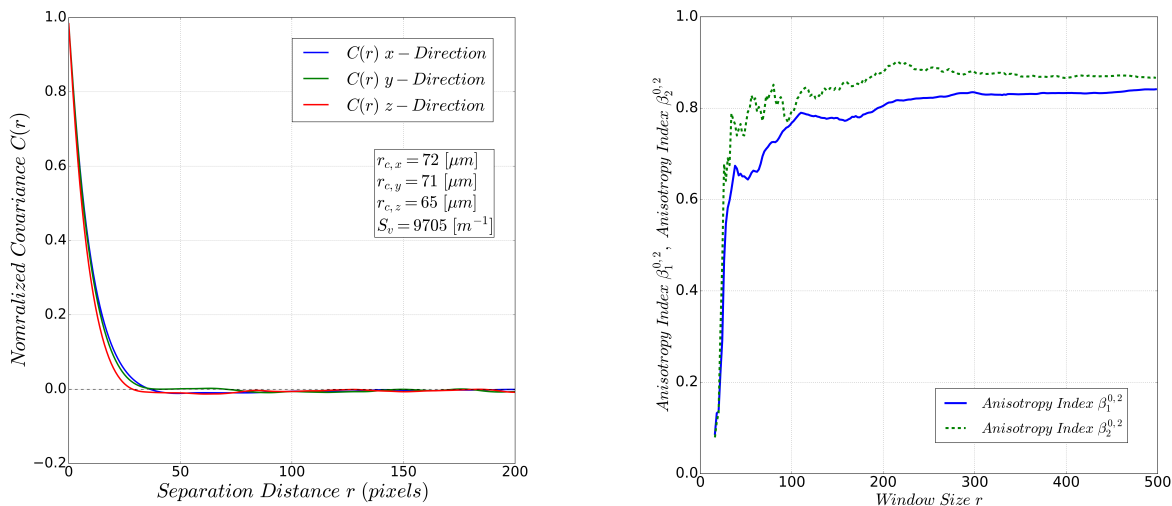
Orthogonal Image Projections:



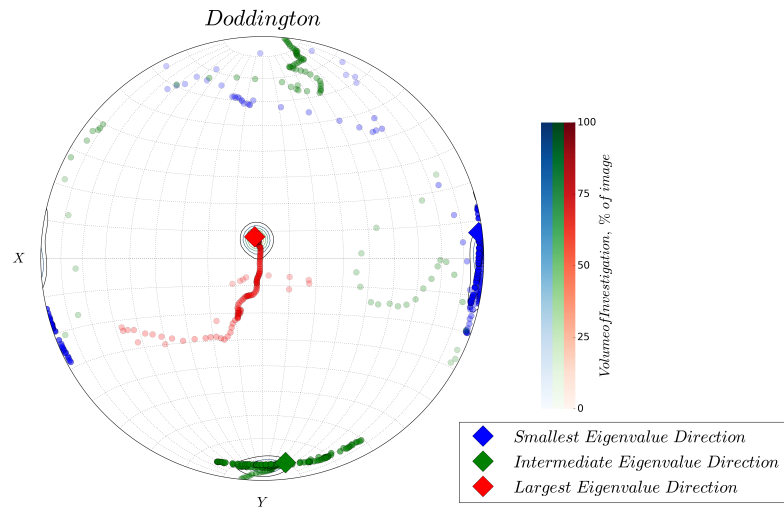
Appendix Figure 20: Orthogonal views of the Doddington image. Views seen from front of sample.

Sample Analysis:

Siliciclastic sandstone with distinct angular grains. The covariance shows small anisotropy ($r_{c,z} < r_{c,x,y}$) therefore the permeability is expected to be smallest in z-direction. The Minkowski tensor shows anisotropy stabilizing at $1600 \mu\text{m}$. The stereonet shows preferential pore-grain interface orientation at small sample sizes.



Appendix Figure 21: Left: Normalized directional covariance of the Doddington sample. Right: Anisotropy indices derived from Minkowski tensor functionals.

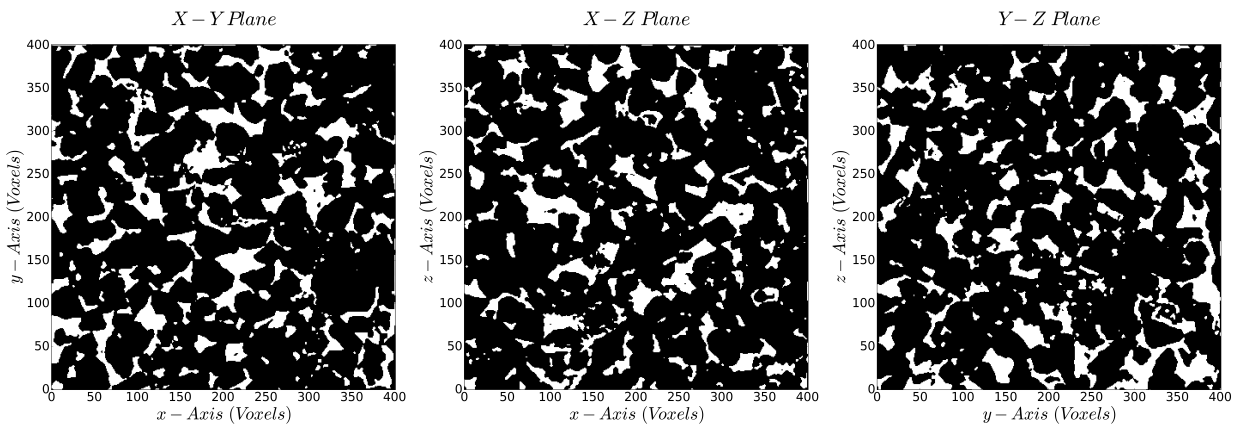


Appendix Figure 22: Stereonet projection of eigenvectors of Minkowski tensor $W_1^{0,2}$ of the Doddington sample.

Results Summary		
Image Name	Doddington	
Rock Type	Sandstone	
Property	Value	Unit
Image Resolution	5.3858	[μm]
Image Dimensions	(500, 500, 500)	(Nx, Ny, Nz) [voxel]
Covariance Analysis Results		
Porosity	0.19	[\cdot]
Directional Characteristic Pore Size [$r_{c,x}, r_{c,y}, r_{c,z}$]	72,71,65	[μm]
Average Characteristic Pore Size \bar{r}_c	63	[μm]
Specific Surface Area	9705	[m^{-1}]
Minkowski Tensor Analysis		
Normalized Minkowski Functional $\widehat{W}_1^{0,2}$	$\begin{bmatrix} 0.313 & 0 & 0.003 \\ 0 & 0.316 & -0.008 \\ 0.003 & -0.008 & 0.371 \end{bmatrix}$	[\cdot]
Normalized Minkowski Functional $\widehat{W}_2^{0,2}$	$\begin{bmatrix} 0.319 & -0.002 & 0 \\ -0.002 & 0.334 & -0.005 \\ 0 & -0.005 & 0.331 \end{bmatrix}$	[\cdot]
Anisotropy Index $\beta_1^{0,2}$	0.84	[\cdot]
Anisotropy Index $\beta_2^{0,2}$	0.87	[\cdot]
Permeability Computation Results		
Effective Porosity	0.19	[\cdot]
Directional Permeability	$\begin{bmatrix} 0.313 & - & - \\ - & 0.308 & - \\ - & - & 0.268 \end{bmatrix}$	[Darcy]

Sample 6: Berea

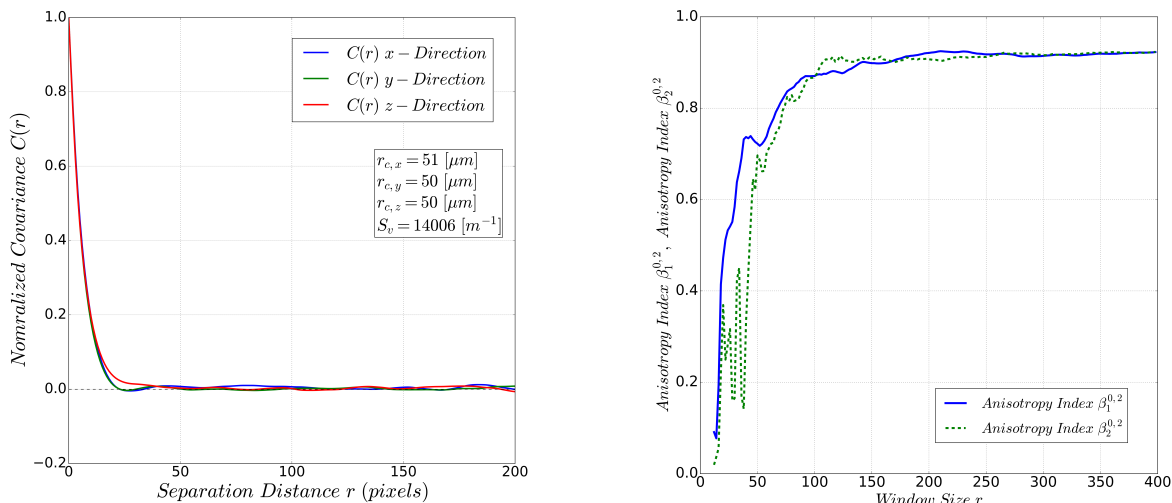
Orthogonal Image Projections:



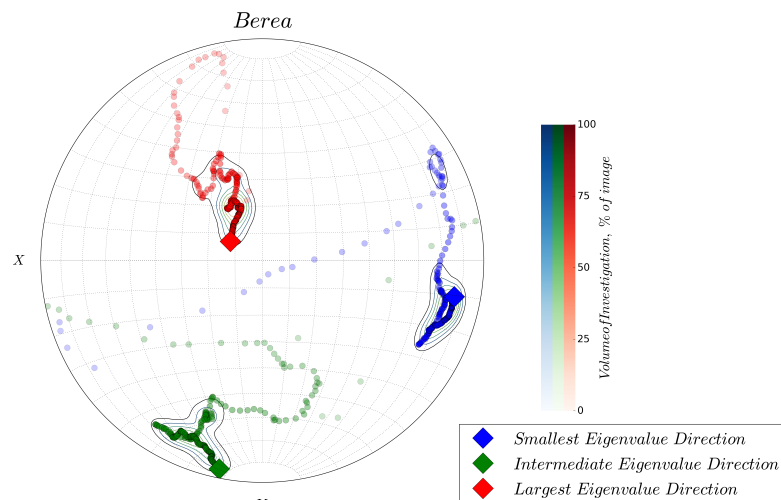
Appendix Figure 23: Orthogonal views of the Berea image. Views seen from front of sample.

Sample Analysis:

Well-known Berea sandstone. Nearly isotropic behavior according to Minkowski tensor and covariance analysis. The stereonet shows a nearly axis-aligned orientation of the eigenvectors of the Minkowski tensor $W_1^{0,2}$. Well defined hole effect in covariance for x and y-direction. The z-direction resembles overlapping grains. Permeability in z-direction slightly deviates from x-y plane.



Appendix Figure 24: Left: Normalized directional covariance of the Berea sample. Right: Anisotropy indices derived from Minkowski tensor functionals.

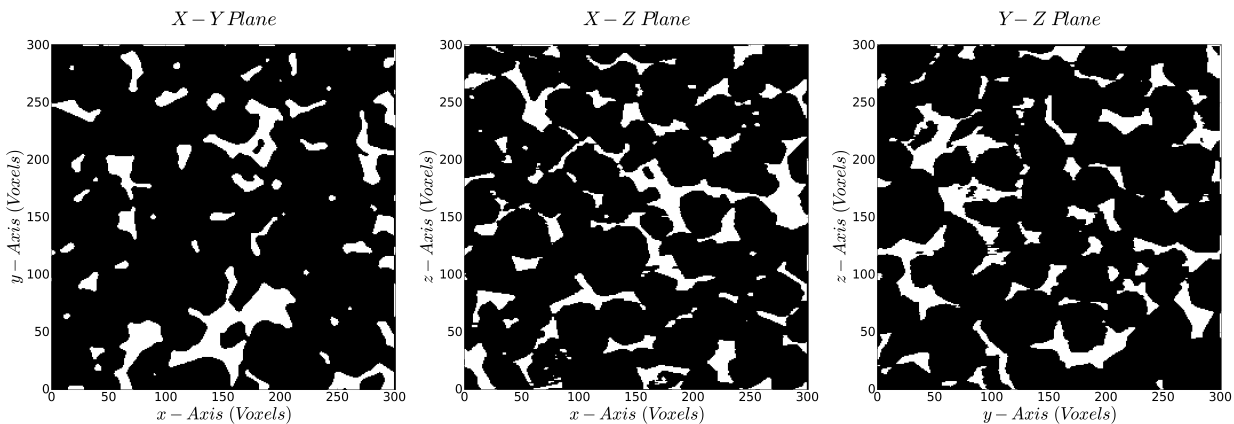


Appendix Figure 25: Stereonet projection of eigenvectors of Minkowski tensor $W_1^{0,2}$ of the Berea sample.

Results Summary		
Image Name	Berea	
Rock Type	Sandstone	
Property	Value	Unit
Image Resolution	5.345	[μm]
Image Dimensions	(300, 300, 300)	(Nx, Ny, Nz) [voxel]
Covariance Analysis Results		
Porosity	0.20	[\cdot]
Directional Characteristic Pore Size [$r_{c,x}, r_{c,y}, r_{c,z}$]	51,50,50	[μm]
Average Characteristic Pore Size \bar{r}_c	45	[μm]
Specific Surface Area	14006	[m^{-1}]
Minkowski Tensor Analysis		
Normalized Minkowski Functional $\widehat{W}_1^{0,2}$	$\begin{bmatrix} 0.321 & 0.003 & 0.005 \\ 0.003 & 0.335 & -0.002 \\ 0.005 & -0.002 & 0.344 \end{bmatrix}$	[\cdot]
Normalized Minkowski Functional $\widehat{W}_2^{0,2}$	$\begin{bmatrix} 0.323 & 0.001 & 0.003 \\ 0.001 & 0.329 & -0.002 \\ 0.003 & -0.002 & 0.349 \end{bmatrix}$	[\cdot]
Anisotropy Index $\beta_1^{0,2}$	0.92	[\cdot]
Anisotropy Index $\beta_2^{0,2}$	0.92	[\cdot]
Permeability Computation Results		
Effective Porosity	0.20	[\cdot]
Directional Permeability	$\begin{bmatrix} 1.378 & - & - \\ - & 1.321 & - \\ - & - & 1.208 \end{bmatrix}$	[Darcy]

Sample 7: S1

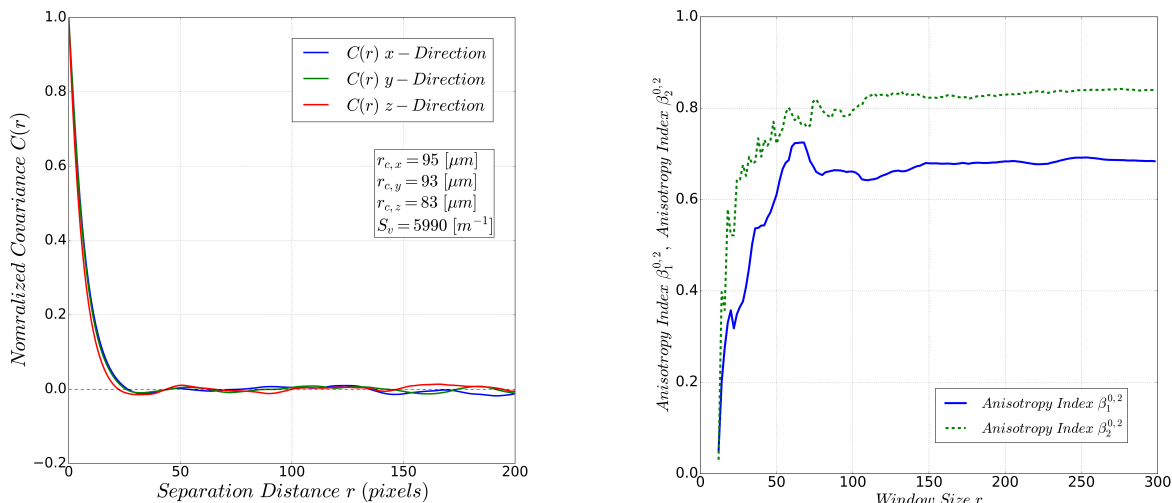
Orthogonal Image Projections:



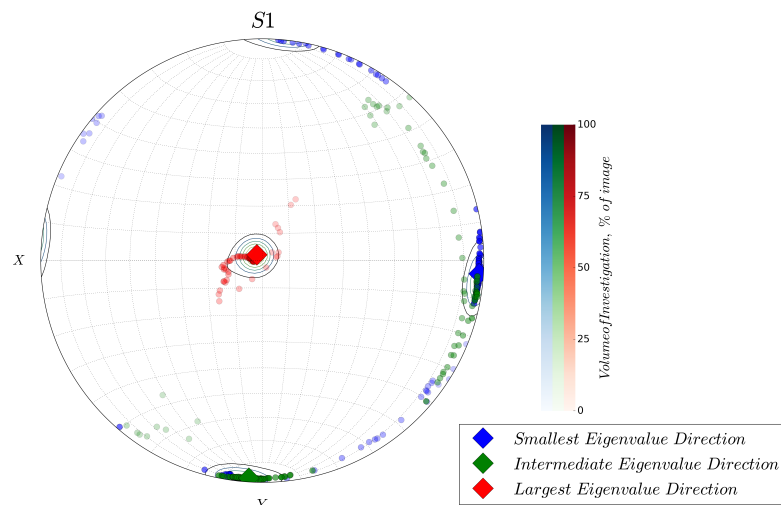
Appendix Figure 26: Orthogonal views of image S1. Views seen from front sample.

Sample Analysis:

Covariance shows well-defined hole-effect in all directions. The initial slope in z-direction steeper, therefore, a smaller characteristic pore size. The Minkowski tensor anisotropy index $\beta_1^{0,2}$ shows strong anisotropy which is reflected in the numerical permeability estimate. The Anisotropy index is equal to ratio of min and max values of permeability tensor ~ 0.68 . Smallest and intermediate eigenvalues switch position indicating that their values are very close.



Appendix Figure 27 Left: Normalized directional covariance of the S1 sample. **Right:** Anisotropy indices derived from Minkowski tensor functionals.

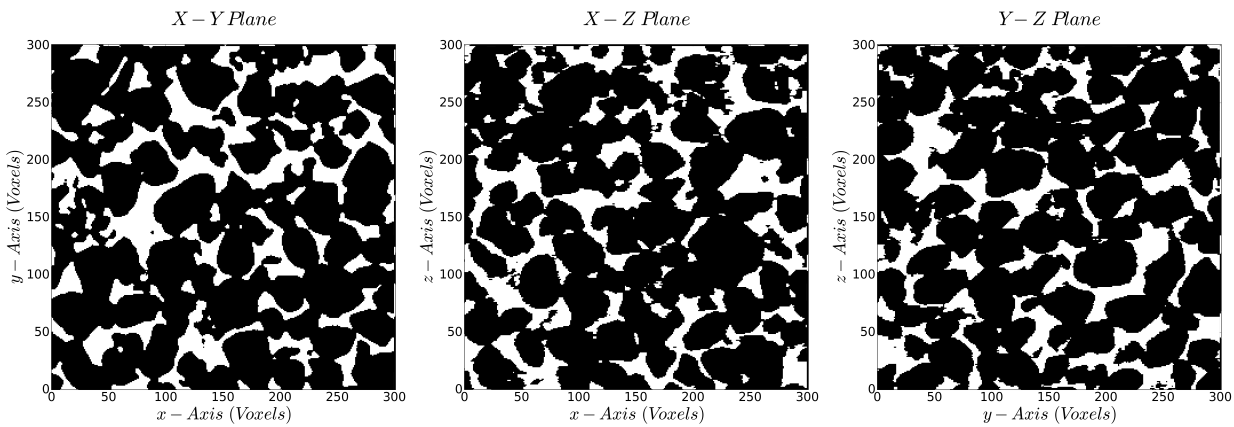


Appendix Figure 28: Stereonet projection of eigenvectors of Minkowski tensor $W_1^{0,2}$ of the S1 sample.

Results Summary		
Image Name	S1	
Rock Type	Sandstone	
Property	Value	Unit
Image Resolution	8.683	[μm]
Image Dimensions	(300, 300, 300)	(Nx, Ny, Nz) [voxel]
Covariance Analysis Results		
Porosity	0.14	[\cdot]
Directional Characteristic Pore Size [$r_{c,x}, r_{c,y}, r_{c,z}$]	95,93,83	[μm]
Average Characteristic Pore Size \bar{r}_c	81	[μm]
Specific Surface Area	5990	[m^{-1}]
Minkowski Tensor Analysis		
Normalized Minkowski Functional $\widehat{W}_1^{0,2}$	$\begin{bmatrix} 0.287 & 0 & 0 \\ 0 & 0.295 & 0 \\ 0 & 0 & 0.419 \end{bmatrix}$	[\cdot]
Normalized Minkowski Functional $\widehat{W}_2^{0,2}$	$\begin{bmatrix} 0.313 & 0 & 0 \\ 0 & 0.315 & -0.002 \\ 0 & -0.002 & 0.372 \end{bmatrix}$	[\cdot]
Anisotropy Index $\beta_1^{0,2}$	0.68	[\cdot]
Anisotropy Index $\beta_2^{0,2}$	0.84	[\cdot]
Permeability Computation Results		
Effective Porosity	0.13	[\cdot]
Directional Permeability	$\begin{bmatrix} 1.995 & - & - \\ - & 1.775 & - \\ - & - & 1.329 \end{bmatrix}$	[Darcy]

Sample 8: S2

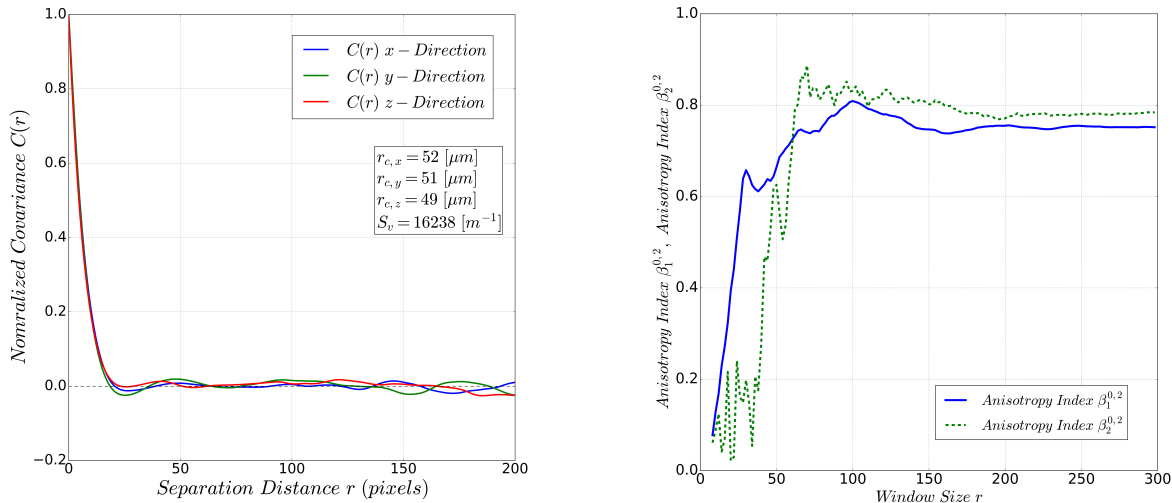
Orthogonal Image Projections:



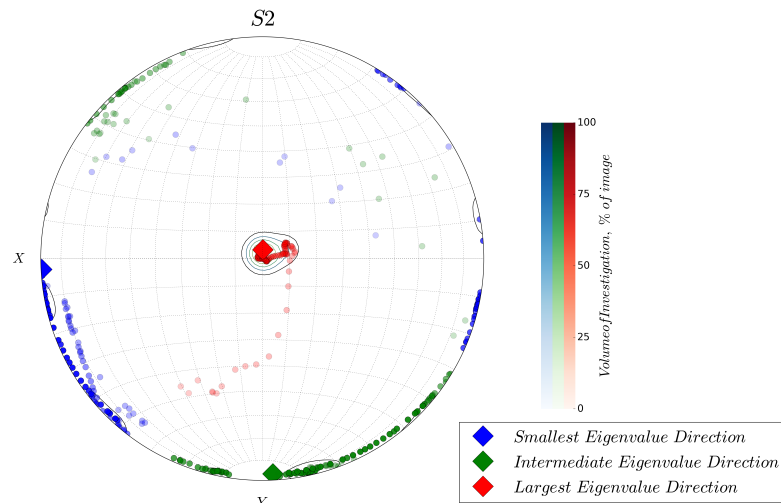
Appendix Figure 29: Orthogonal views of image S2. Views seen from front sample.

Sample Analysis:

Siliciclastic sandstone sample S2. Pronounced periodicity in the covariance with significantly different wavelength. Nearly same characteristic pore size in all three Cartesian directions. Anisotropy indicated by Minkowski tensor and in numerical permeability tensor. Principal directions of Minkowski tensor $W_1^{0,2}$, characteristic pore size from covariance and permeability do not align. Intermediate and smallest eigenvalues are nearly equal and switch position as volume of investigation grows larger.



Appendix Figure 30 Left: Normalized directional covariance of the S2 sample. Right: Anisotropy indices derived from Minkowski tensor functionals.

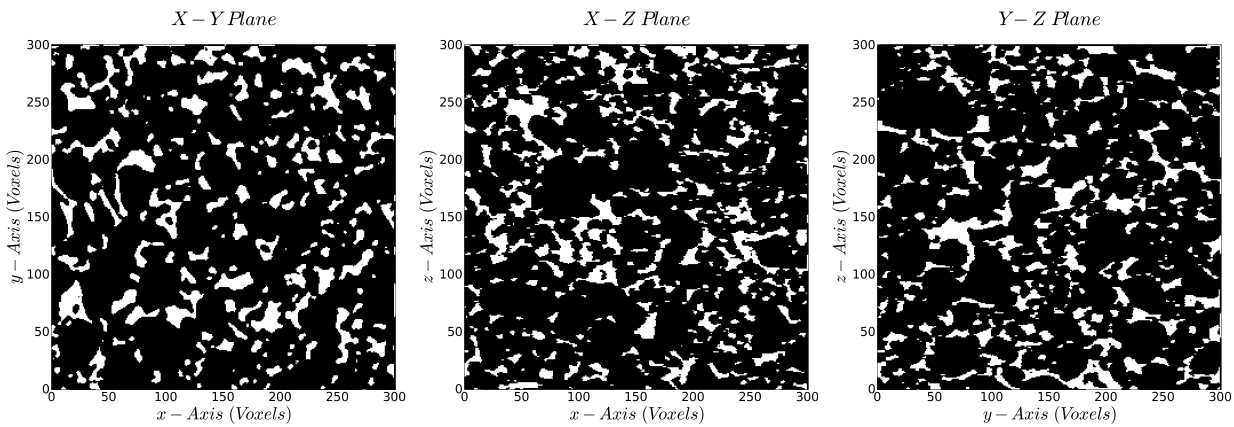


Appendix Figure 31: Stereonet projection of eigenvectors of Minkowski tensor $W_1^{0,2}$ of the S2 sample.

Results Summary		
Image Name	S2	
Rock Type	Sandstone	
Property	Value	Unit
Image Resolution	4.956	[μm]
Image Dimensions	(300, 300, 300)	(Nx, Ny, Nz) [voxel]
Covariance Analysis Results		
Porosity	0.25	[\cdot]
Directional Characteristic Pore Size [$r_{c,x}, r_{c,y}, r_{c,z}$]	52,51,49	[μm]
Average Characteristic Pore Size \bar{r}_c	45	[μm]
Specific Surface Area	16238	[m^{-1}]
Minkowski Tensor Analysis		
Normalized Minkowski Functional $\widehat{W}_1^{0,2}$	$\begin{bmatrix} 0.300 & 0 & 0 \\ 0 & 0.303 & 0 \\ 0 & 0 & 0.398 \end{bmatrix}$	[\cdot]
Normalized Minkowski Functional $\widehat{W}_2^{0,2}$	$\begin{bmatrix} 0.315 & 0.01 & 0.002 \\ 0.01 & 0.306 & -0.008 \\ 0.002 & -0.008 & 0.379 \end{bmatrix}$	[\cdot]
Anisotropy Index $\beta_1^{0,2}$	0.75	[\cdot]
Anisotropy Index $\beta_2^{0,2}$	0.78	[\cdot]
Permeability Computation Results		
Effective Porosity	0.25	[\cdot]
Directional Permeability	$\begin{bmatrix} 4.375 & - & - \\ - & 4.035 & - \\ - & - & 3.439 \end{bmatrix}$	[Darcy]

Sample 9: S3

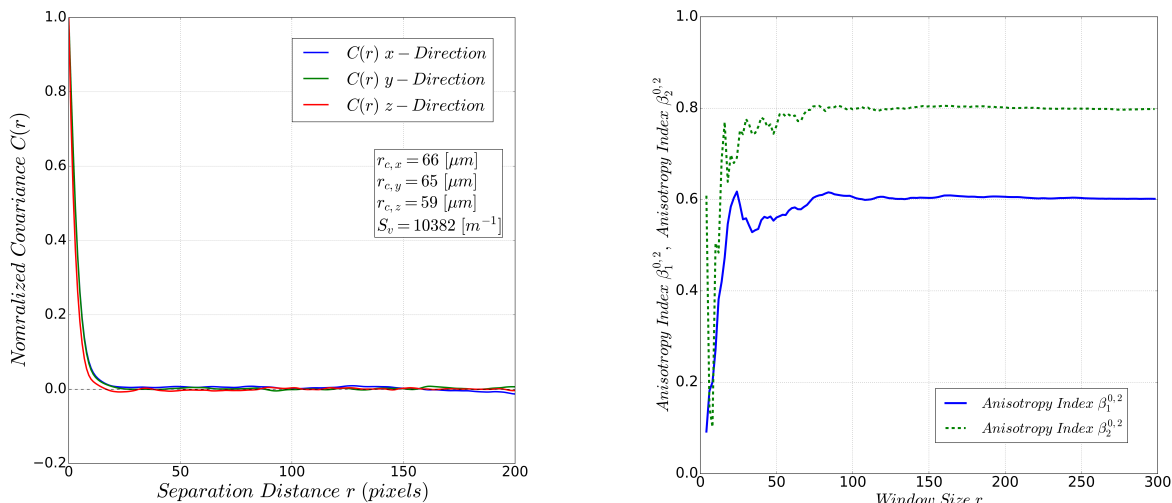
Orthogonal Image Projections:



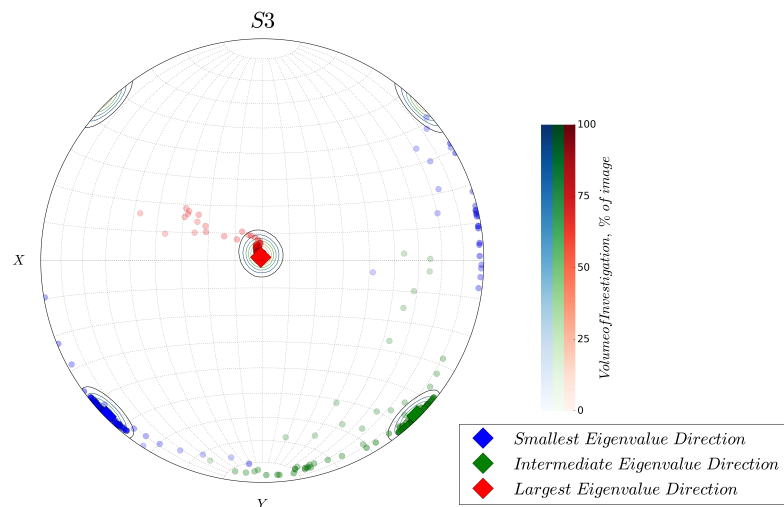
Appendix Figure 32: Orthogonal views of image S3. Views seen from front of sample.

Sample Analysis:

Siliciclastic sandstone sample S3 with numerous distinct angular grains visible. Reduced characteristic pore size in z-direction indicated by covariance and confirmed by permeability estimate. Very early stabilization of anisotropy index $\beta_1^{0,2}$.



Appendix Figure 33: Left: Normalized directional covariance of the S3 sample. Right: Anisotropy indices derived from Minkowski tensor functionals.

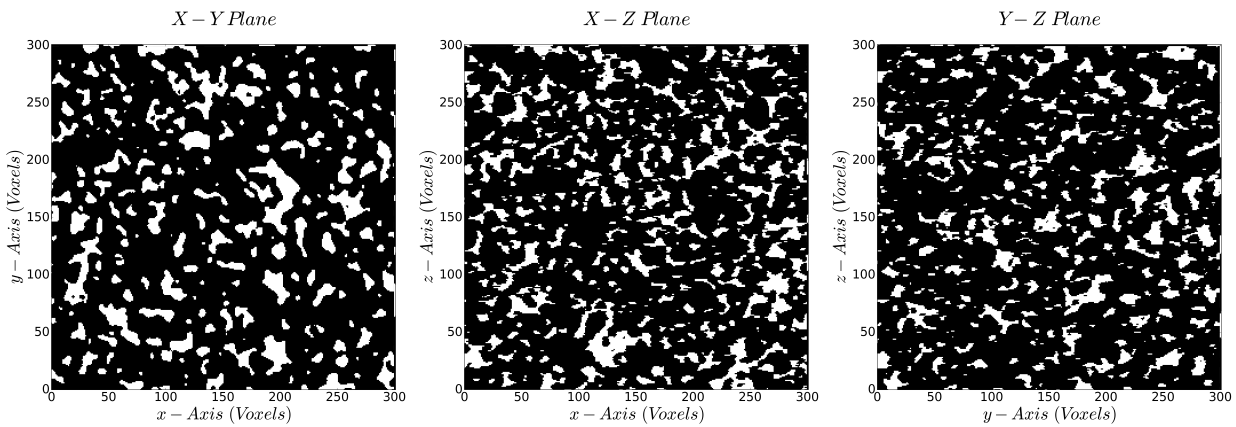


Appendix Figure 34: Stereonet projection of eigenvectors of Minkowski tensor $W_1^{0,2}$ of the S3 sample.

Results Summary		
Image Name	S3	
Rock Type	Sandstone	
Property	Value	Unit
Image Resolution	9.1	[μm]
Image Dimensions	(300, 300, 300)	(Nx, Ny, Nz) [voxel]
Covariance Analysis Results		
Porosity	0.17	[\cdot]
Directional Characteristic Pore Size [$r_{c,x}, r_{c,y}, r_{c,z}$]	66,65,59	[μm]
Average Characteristic Pore Size \bar{r}_c	54	[μm]
Specific Surface Area	10382	[m^{-1}]
Minkowski Tensor Analysis		
Normalized Minkowski Functional $\widehat{W}_1^{0,2}$	$\begin{bmatrix} 0.276 & -0.007 & 0.002 \\ -0.007 & 0.276 & -0.004 \\ 0.002 & -0.004 & 0.447 \end{bmatrix}$	[\cdot]
Normalized Minkowski Functional $\widehat{W}_2^{0,2}$	$\begin{bmatrix} 0.309 & 0 & 0 \\ 0 & 0.307 & 0 \\ 0 & 0 & 0.383 \end{bmatrix}$	[\cdot]
Anisotropy Index $\beta_1^{0,2}$	0.60	[\cdot]
Anisotropy Index $\beta_2^{0,2}$	0.79	[\cdot]
Permeability Computation Results		
Effective Porosity	0.17	[\cdot]
Directional Permeability	$\begin{bmatrix} 0.145 & - & - \\ - & 0.425 & - \\ - & - & 0.110 \end{bmatrix}$	[Darcy]

Sample 10: S4

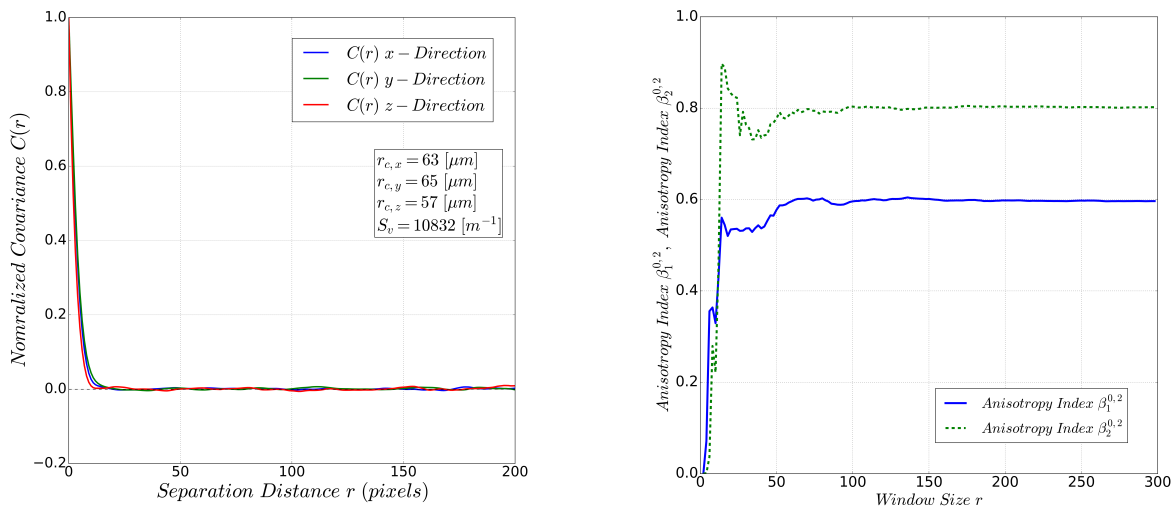
Orthogonal Image Projections:



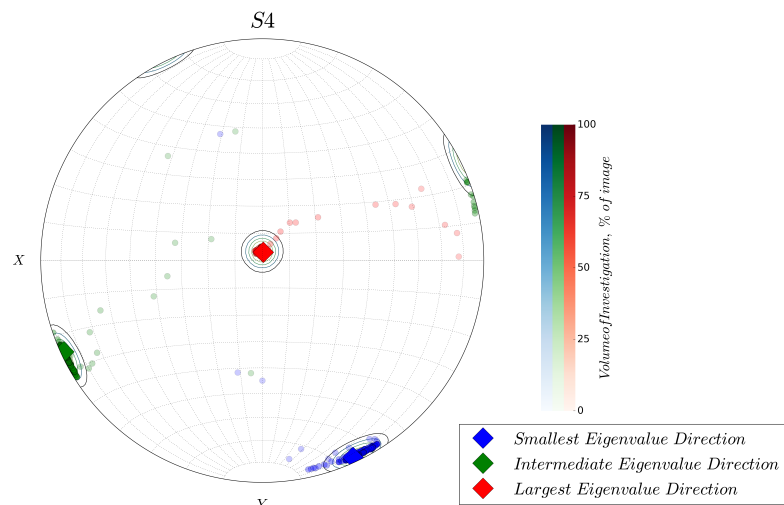
Appendix Figure 35: Orthogonal views of image S4. Views seen from front of sample.

Sample Analysis:

Sandstone sample S4. Significant variation in covariance depending on the direction of measurement. Little or no hole effect can be identified. By visual inspection and based on covariance grains are overlapping. Intrinsic anisotropy at $\beta_1^{0,2}$ can be identified. Stereonet of eigenvectors shows near axis aligned orientation of pore-grain interface across all sample sizes. Permeability lowest in z-direction which correlates with characteristic pore size and Minkowski tensor orientation.



Appendix Figure 36: Left: Normalized directional covariance of the S4 sample. Right: Anisotropy indices derived from Minkowski tensor functionals.

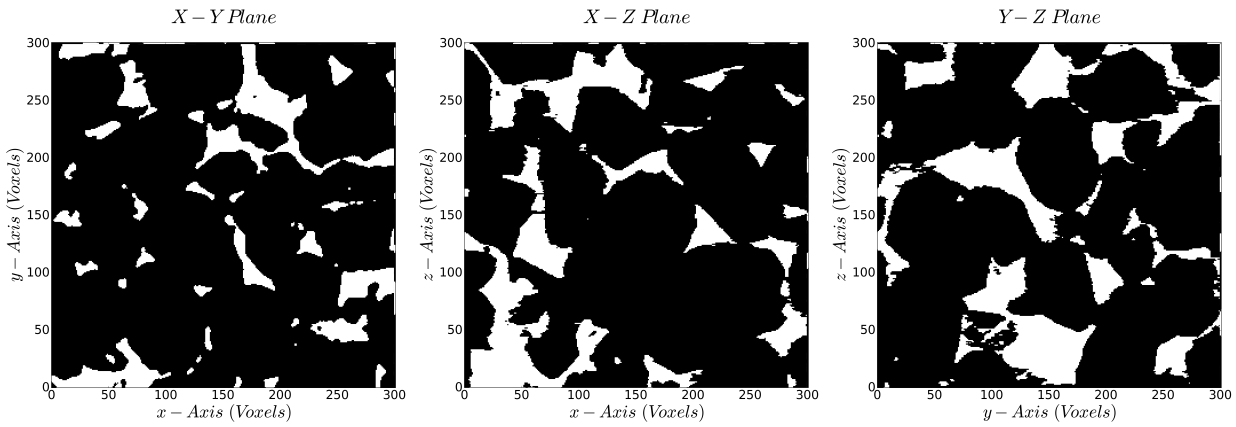


Appendix Figure 37: Stereonet projection of eigenvectors of Minkowski tensor $W_1^{0,2}$ of the S4 sample.

Results Summary		
Image Name	S4	
Rock Type	Sandstone	
Property	Value	Unit
Image Resolution	8.96	[μm]
Image Dimensions	(300, 300, 300)	(Nx, Ny, Nz) [voxel]
Covariance Analysis Results		
Porosity	0.17	[\cdot]
Directional Characteristic Pore Size [$r_{c,x}, r_{c,y}, r_{c,z}$]	63,65,57	[μm]
Average Characteristic Pore Size \bar{r}_c	52	[μm]
Specific Surface Area	10832	[m^{-1}]
Minkowski Tensor Analysis		
Normalized Minkowski Functional $\widehat{W}_1^{0,2}$	$\begin{bmatrix} 0.282 & 0.008 & 0 \\ 0.008 & 0.270 & -0.009 \\ 0 & -0.009 & 0.445 \end{bmatrix}$	[\cdot]
Normalized Minkowski Functional $\widehat{W}_2^{0,2}$	$\begin{bmatrix} 0.314 & 0 & 0 \\ 0 & 0.307 & 0 \\ 0 & 0 & 0.379 \end{bmatrix}$	[\cdot]
Anisotropy Index $\beta_1^{0,2}$	0.59	[\cdot]
Anisotropy Index $\beta_2^{0,2}$	0.80	[\cdot]
Permeability Computation Results		
Effective Porosity	0.17	[\cdot]
Directional Permeability	$\begin{bmatrix} 0.276 & - & - \\ - & 0.292 & - \\ - & - & 0.218 \end{bmatrix}$	[Darcy]

Sample 11: S5

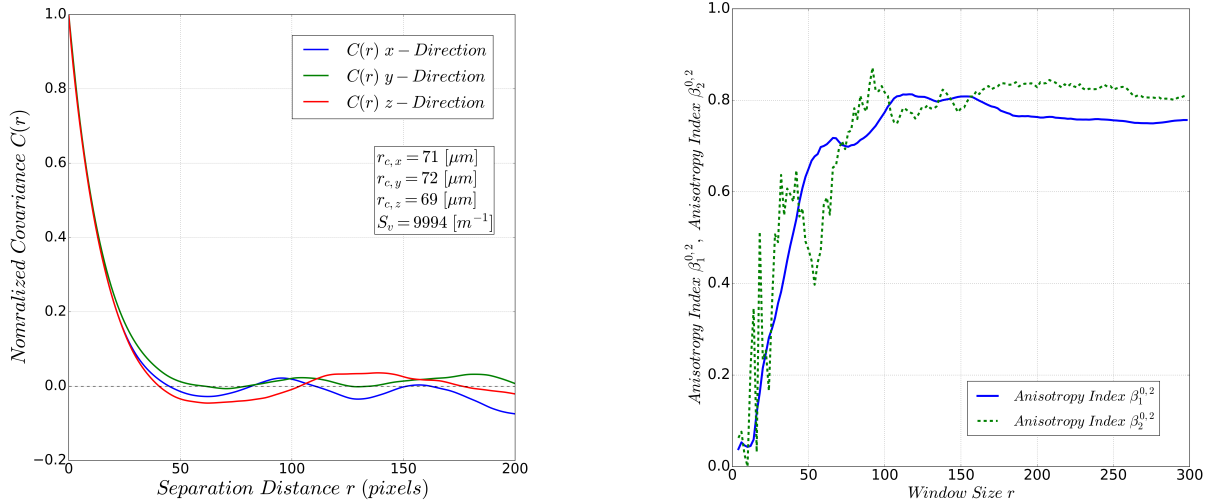
Orthogonal Image Projections:



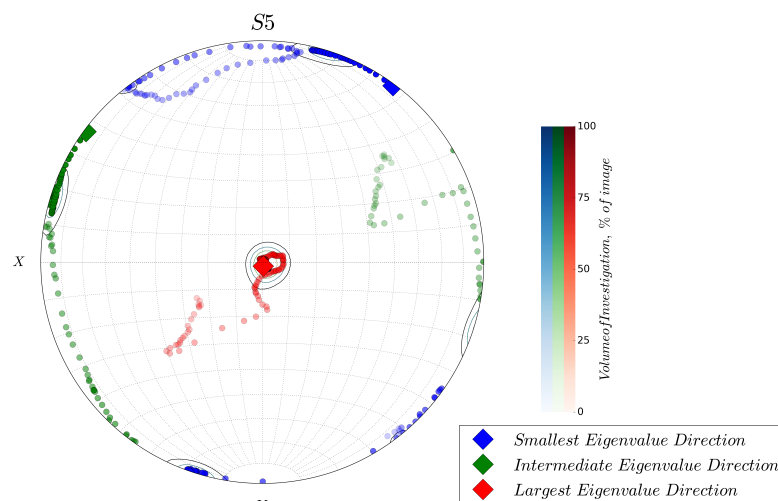
Appendix Figure 38: Orthogonal views of image S5. Views seen from front of sample.

Sample Analysis:

The sample is of sedimentary siliciclastic origin. Large individual grains are distinguishable on the Micro-CT image. Significant hole effect in the covariance indicates that grains are separate and act as hard spheres. Nearly equal characteristic pore sizes. Opposed to the covariance, anisotropy is reported by the Minkowski tensor and is confirmed by the permeability tensor where 10% difference between y and z-direction permeability can be observed. Smallest and intermediate eigenvalues very close therefore associated eigenvectors switch position as REV is reached.



Appendix Figure 39: Left: Normalized directional covariance of the S5 sample. Right: Anisotropy indices derived from Minkowski tensor functionals.

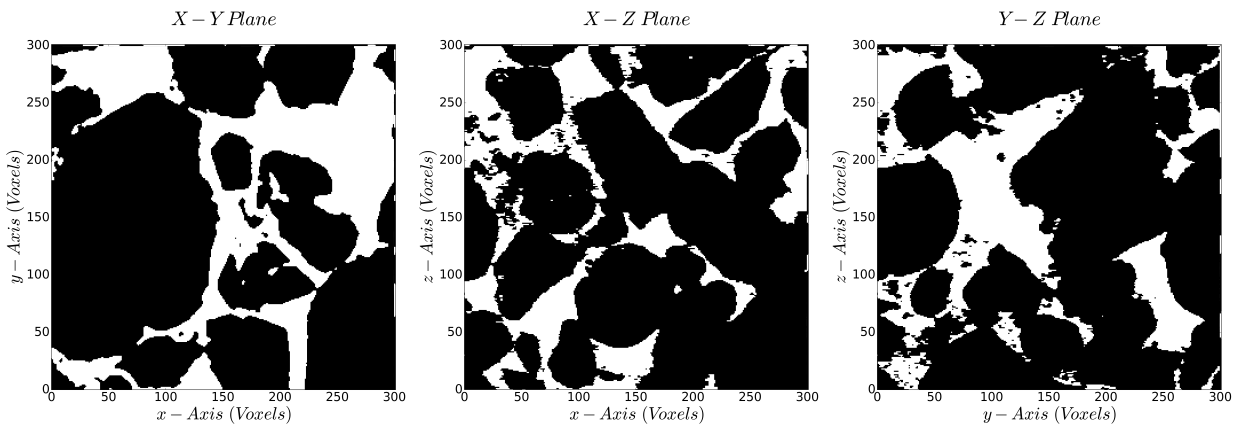


Appendix Figure 40: Stereonet projection of eigenvectors of Minkowski tensor $W_1^{0,2}$ of the S5 sample.

Results Summary		
Image Name	S5	
Rock Type	Sandstone	
Property	Value	Unit
Image Resolution	3.997	[μm]
Image Dimensions	(300, 300, 300)	(Nx, Ny, Nz) [voxel]
Covariance Analysis Results		
Porosity	0.21	[\cdot]
Directional Characteristic Pore Size [$r_{c,x}, r_{c,y}, r_{c,z}$]	71,72,69	[μm]
Average Characteristic Pore Size \bar{r}_c	67	[μm]
Specific Surface Area	9994	[m^{-1}]
Minkowski Tensor Analysis		
Normalized Minkowski Functional $\widehat{W}_1^{0,2}$	$\begin{bmatrix} 0.304 & -0.004 & 0 \\ -0.004 & 0.301 & 0.002 \\ 0 & 0.002 & 0.394 \end{bmatrix}$	[\cdot]
Normalized Minkowski Functional $\widehat{W}_2^{0,2}$	$\begin{bmatrix} 0.310 & 0.008 & -0.004 \\ 0.008 & 0.315 & 0.003 \\ -0.004 & 0.003 & 0.374 \end{bmatrix}$	[\cdot]
Anisotropy Index $\beta_1^{0,2}$	0.76	[\cdot]
Anisotropy Index $\beta_2^{0,2}$	0.81	[\cdot]
Permeability Computation Results		
Effective Porosity	0.21	[\cdot]
Directional Permeability	$\begin{bmatrix} 4.745 & - & - \\ - & 4.938 & - \\ - & - & 4.498 \end{bmatrix}$	[Darcy]

Sample 12: S6

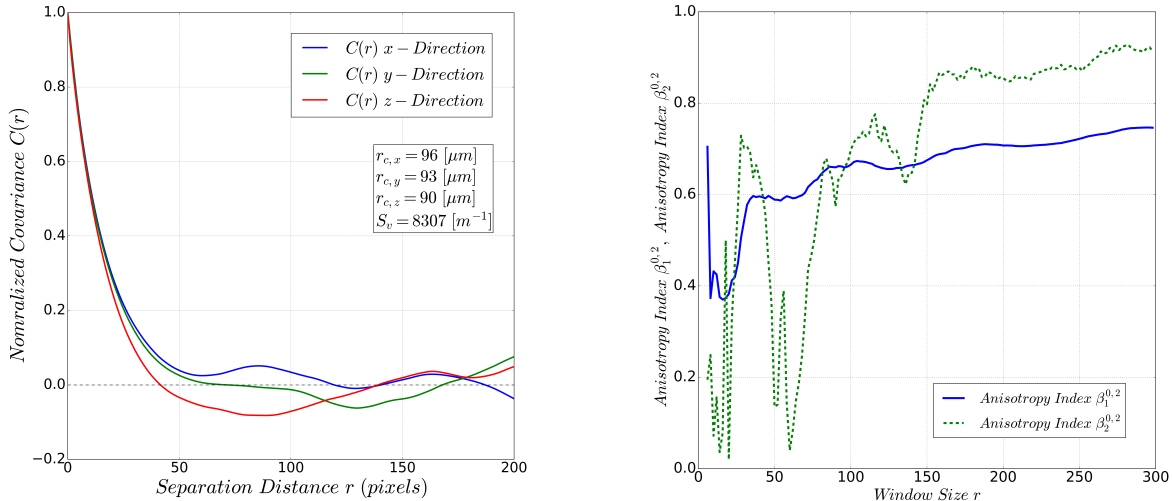
Orthogonal Image Projections:



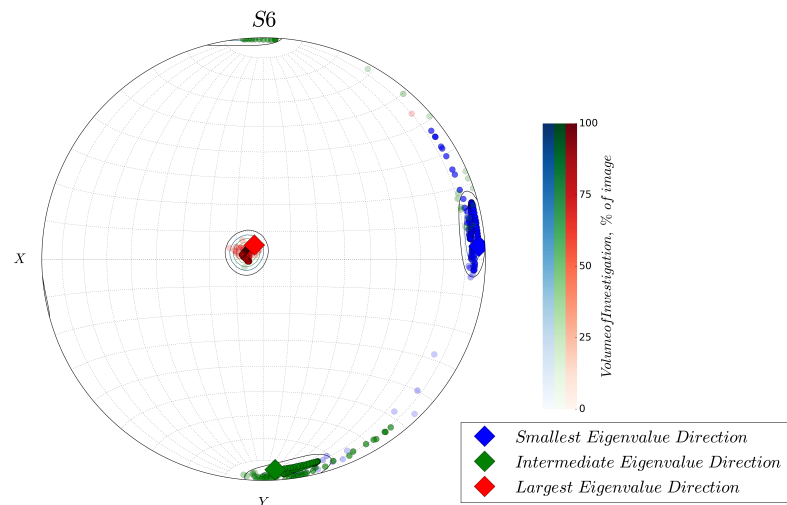
Appendix Figure 41: Orthogonal views of image S6. Views seen from front of sample.

Sample Analysis:

Large fractured sand grains of non-uniform size identifiable on Micro-CT images. Large fluctuations and orientational differences are seen in the estimated covariance. Permeability tensor does not agree with covariance or Minkowski tensor. Permeability is anisotropic at 5% difference between smallest and largest values, but much stronger anisotropy is indicated by both covariance and Minkowski tensor. Anisotropy index does not stabilize to one value indicating that an REV is not reached. The orientation of eigenvectors axis-aligned with little variation.



Appendix Figure 42: Left: Normalized directional covariance of the S6 sample. Right: Anisotropy indices derived from Minkowski tensor functionals.

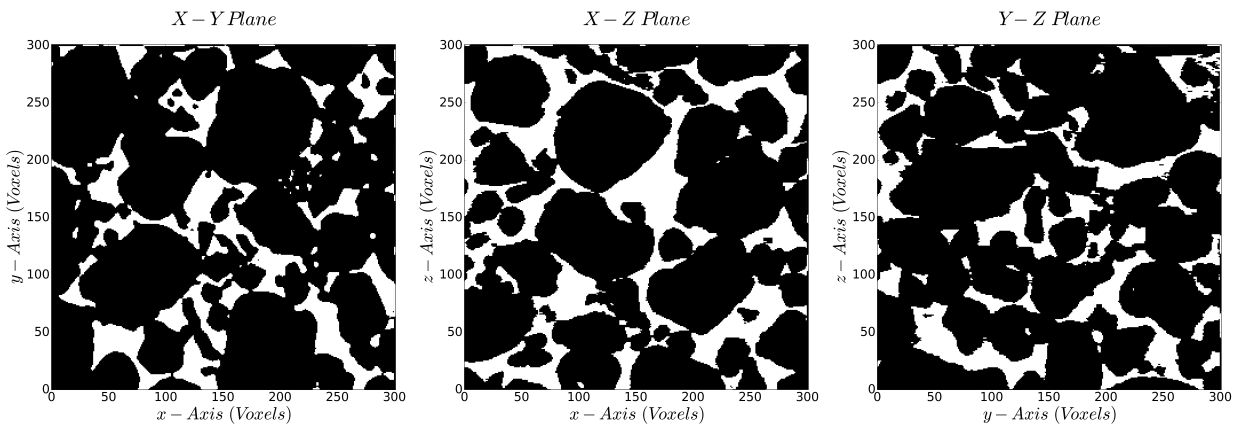


Appendix Figure 43: Stereonet projection of eigenvectors of Minkowski tensor $W_1^{0.2}$ of the S6 sample.

Results Summary		
Image Name	S6	
Rock Type	Sandstone	
Property	Value	Unit
Image Resolution	5.1	[μm]
Image Dimensions	(300, 300, 300)	(Nx, Ny, Nz) [voxel]
Covariance Analysis Results		
Porosity	0.24	[\cdot]
Directional Characteristic Pore Size [$r_{c,x}, r_{c,y}, r_{c,z}$]	96,93,90	[μm]
Average Characteristic Pore Size \bar{r}_c	88	[μm]
Specific Surface Area	8307	[m^{-1}]
Minkowski Tensor Analysis		
Normalized Minkowski Functional $\widehat{W}_1^{0,2}$	$\begin{bmatrix} 0.335 & -0.001 & 0.006 \\ -0.001 & 0.307 & -0.008 \\ 0.006 & -0.008 & 0.396 \end{bmatrix}$	[\cdot]
Normalized Minkowski Functional $\widehat{W}_2^{0,2}$	$\begin{bmatrix} 0.324 & 0.003 & 0.007 \\ 0.003 & 0.328 & 0.005 \\ 0.007 & 0.005 & 0.348 \end{bmatrix}$	[\cdot]
Anisotropy Index $\beta_1^{0,2}$	0.75	[\cdot]
Anisotropy Index $\beta_2^{0,2}$	0.91	[\cdot]
Permeability Computation Results		
Effective Porosity	0.24	[\cdot]
Directional Permeability	$\begin{bmatrix} 11.43 & - & - \\ - & 10.82 & - \\ - & - & 11.09 \end{bmatrix}$	[Darcy]

Sample 13: S7

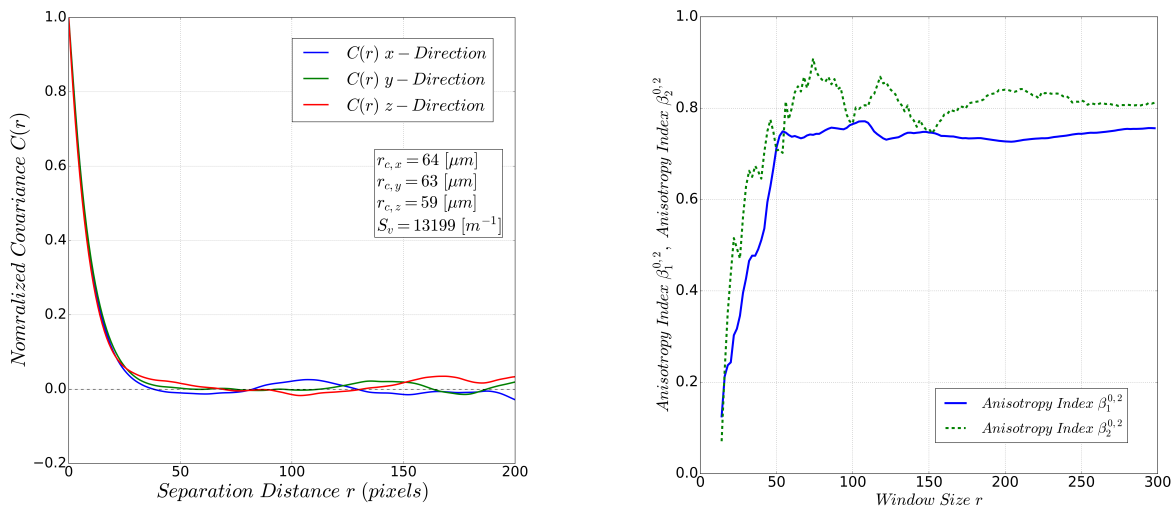
Orthogonal Image Projections:



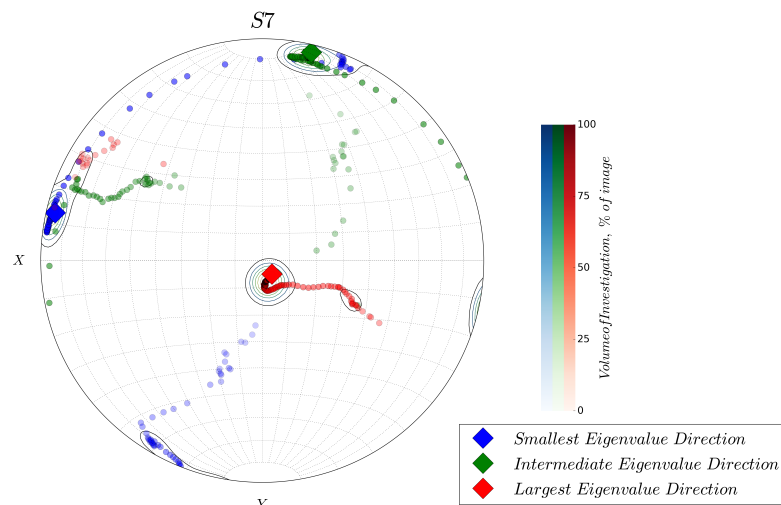
Appendix Figure 44: Orthogonal views of image S7. Views seen from front of sample.

Sample Analysis:

Sandstone consisting of individual angular grains. Variation in characteristic pore size observed for estimated covariance. Anisotropy index $\beta_1^{0,2}$ shows significant anisotropy and no clear stabilisation i.e. this sedimentary rock does not have an intrinsic anisotropy at the image scale. This is also indicated by the covariance as large fluctuations occur with increasing observation distance r . Permeability is smallest in z-direction which is confirmed by Minkowski tensor and covariance.



Appendix Figure 45 Left: Normalized directional covariance of the S7 sample. Right: Anisotropy indices derived from Minkowski tensor functionals.

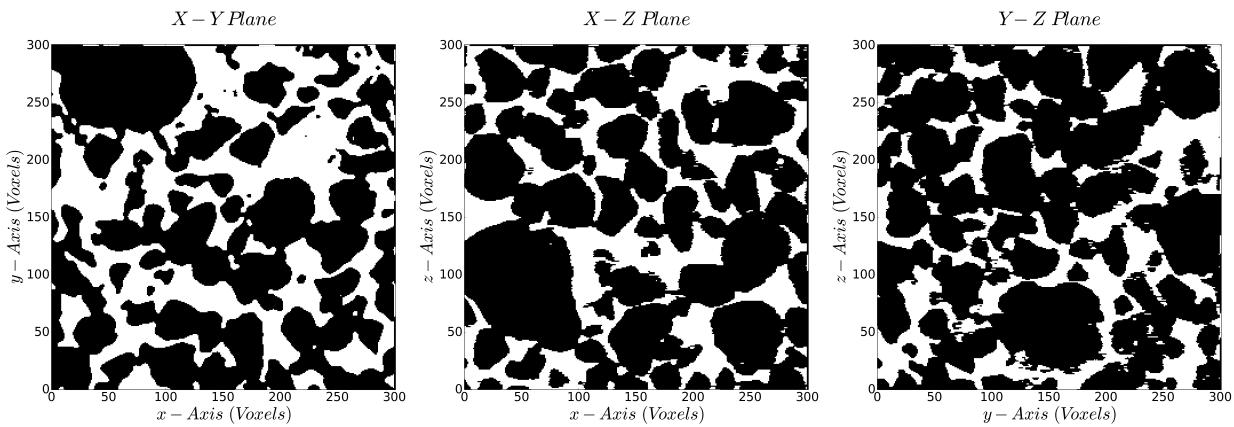


Appendix Figure 46: Stereonet projection of eigenvectors of Minkowski tensor $W_1^{0,2}$ of the S7 sample.

Results Summary		
Image Name	S7	
Rock Type	Sandstone	
Property	Value	Unit
Image Resolution	4.803	[μm]
Image Dimensions	(300, 300, 300)	(Nx, Ny, Nz) [voxel]
Covariance Analysis Results		
Porosity	0.25	[\cdot]
Directional Characteristic Pore Size [$r_{c,x}, r_{c,y}, r_{c,z}$]	64,63,59	[μm]
Average Characteristic Pore Size \bar{r}_c	57	[μm]
Specific Surface Area	13199	[m^{-1}]
Minkowski Tensor Analysis		
Normalized Minkowski Functional $\widehat{W}_1^{0,2}$	$\begin{bmatrix} 0.301 & 0 & 0 \\ 0 & 0.303 & 0 \\ 0 & 0 & 0.396 \end{bmatrix}$	[\cdot]
Normalized Minkowski Functional $\widehat{W}_2^{0,2}$	$\begin{bmatrix} 0.304 & -0.003 & -0.004 \\ -0.004 & 0.323 & 0.003 \\ -0.004 & 0.003 & 0.373 \end{bmatrix}$	[\cdot]
Anisotropy Index $\beta_1^{0,2}$	0.76	[\cdot]
Anisotropy Index $\beta_2^{0,2}$	0.81	[\cdot]
Permeability Computation Results		
Effective Porosity	0.25	[\cdot]
Directional Permeability	$\begin{bmatrix} 7.364 & - & - \\ - & 7.694 & - \\ - & - & 6.117 \end{bmatrix}$	[Darcy]

Sample 14: S8

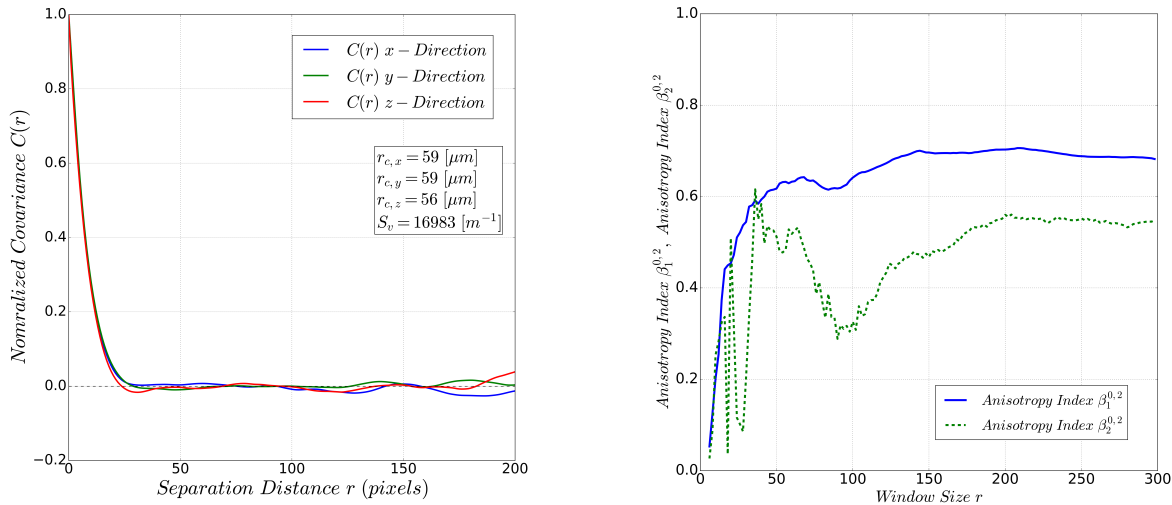
Orthogonal Image Projections:



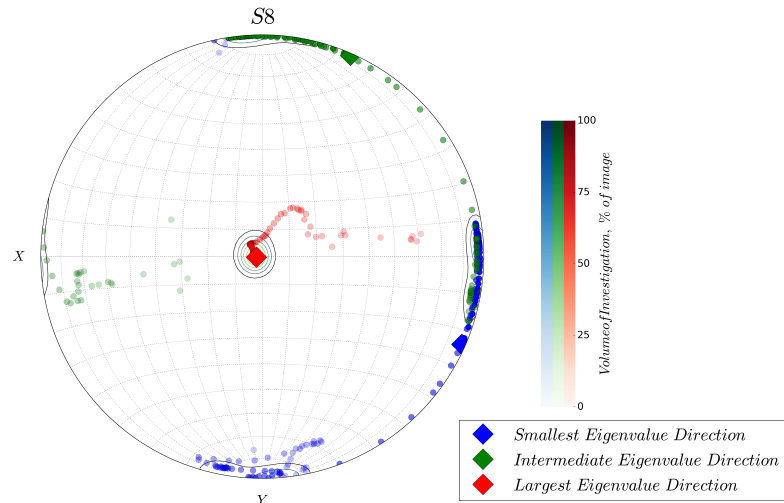
Appendix Figure 47: Orthogonal views of image S8. Views seen from front of sample.

Sample Analysis:

Smooth individual grains observed from Micro-CT image. Covariance estimate in z-direction shows pronounced hole-effect compared to x and y-directions. Anisotropy index difficult to interpret. Possible stabilization at 150 voxels to 200 voxels. Requires sub volume sampling at this scale to confirm. Smallest and intermediate eigenvalues/vectors very close therefore switching in orientation can be observed on stereonet projection.



Appendix Figure 48: Left: Normalized directional covariance of the S8 sample. Right: Anisotropy indices derived from Minkowski tensor functionals.

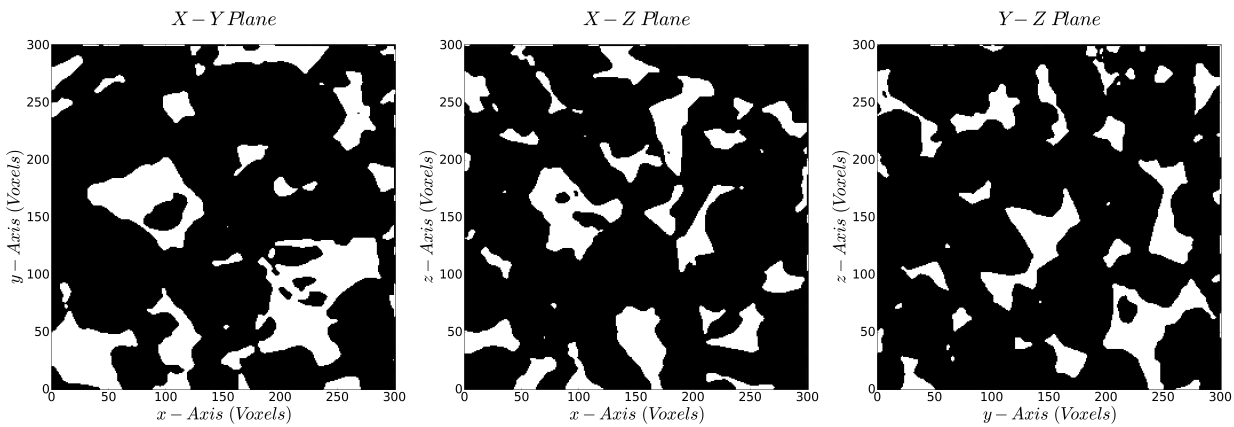


Appendix Figure 49: Stereonet projection of eigenvectors of Minkowski tensor $W_1^{0,2}$ of the S8 sample.

Results Summary		
Image Name	S8	
Rock Type	Sandstone	
Property	Value	Unit
Image Resolution	4.892	[μm]
Image Dimensions	(300, 300, 300)	(Nx, Ny, Nz) [voxel]
Covariance Analysis Results		
Porosity	0.34	[\cdot]
Directional Characteristic Pore Size [$r_{c,x}, r_{c,y}, r_{c,z}$]	59,59,56	[μm]
Average Characteristic Pore Size \bar{r}_c	53	[μm]
Specific Surface Area	16983	[m^{-1}]
Minkowski Tensor Analysis		
Normalized Minkowski Functional $\widehat{W}_1^{0,2}$	$\begin{bmatrix} 0.288 & 0 & 0.005 \\ 0 & 0.289 & 0 \\ 0.005 & 0 & 0.422 \end{bmatrix}$	[\cdot]
Normalized Minkowski Functional $\widehat{W}_2^{0,2}$	$\begin{bmatrix} 0.258 & -0.021 & 0.003 \\ -0.021 & 0.289 & 0.002 \\ 0.003 & 0.002 & 0.452 \end{bmatrix}$	[\cdot]
Anisotropy Index $\beta_1^{0,2}$	0.68	[\cdot]
Anisotropy Index $\beta_2^{0,2}$	0.55	[\cdot]
Permeability Computation Results		
Effective Porosity	0.34	[\cdot]
Directional Permeability	$\begin{bmatrix} 13.24 & - & - \\ - & 13.68 & - \\ - & - & 13.11 \end{bmatrix}$	[Darcy]

Sample 15: S9

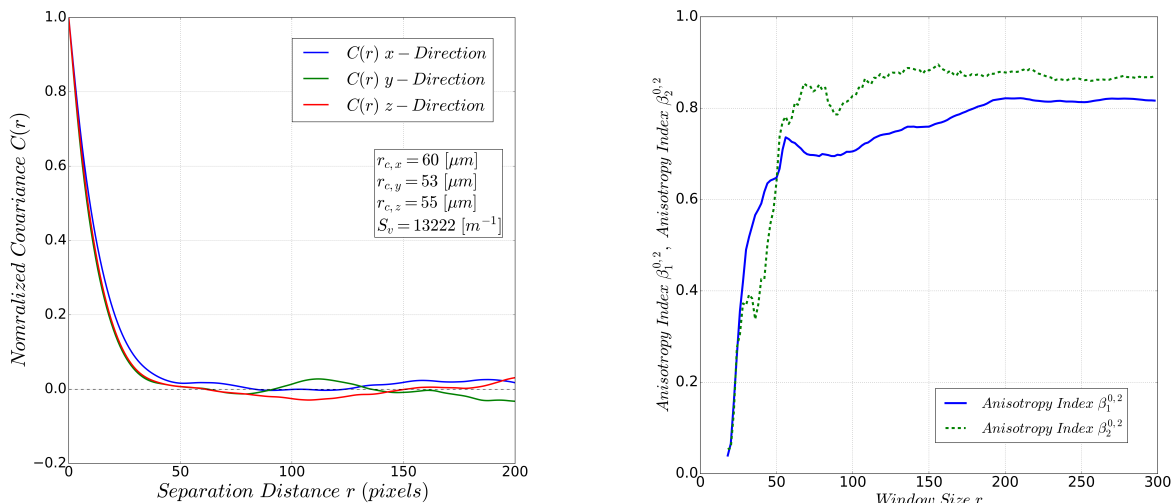
Orthogonal Image Projections:



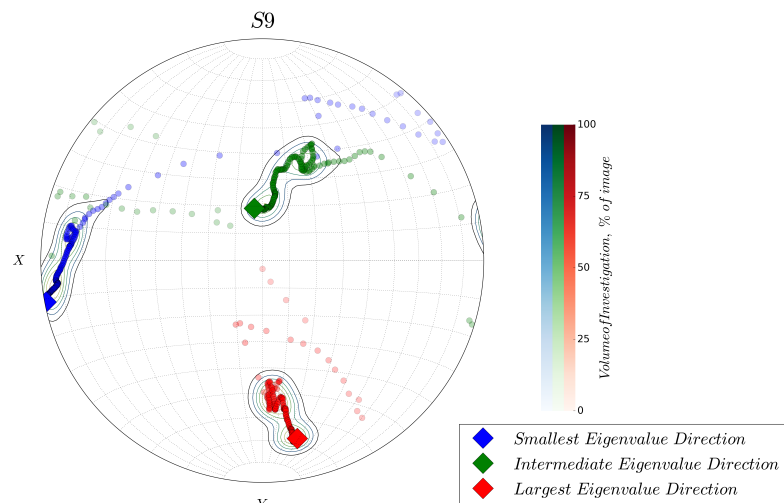
Appendix Figure 50: Orthogonal views of image S9. Views seen from front of sample.

Sample Analysis:

Micro-CT image of sample S9 shows smooth grains with no distinct grain-grain boundaries. Significant variation in estimated covariance. No clear stabilization of the covariance can be observed. The Minkowski tensor shows an intrinsic anisotropy at 0.8 for images greater than 200 voxels edge length. Strong variation in the orientation of eigenvectors can be found. Permeability smallest in z-direction which does not correlate with covariance or Minkowski results.



Appendix Figure 51: Left: Normalized directional covariance of the S9 sample. Right: Anisotropy indices derived from Minkowski tensor functionals.

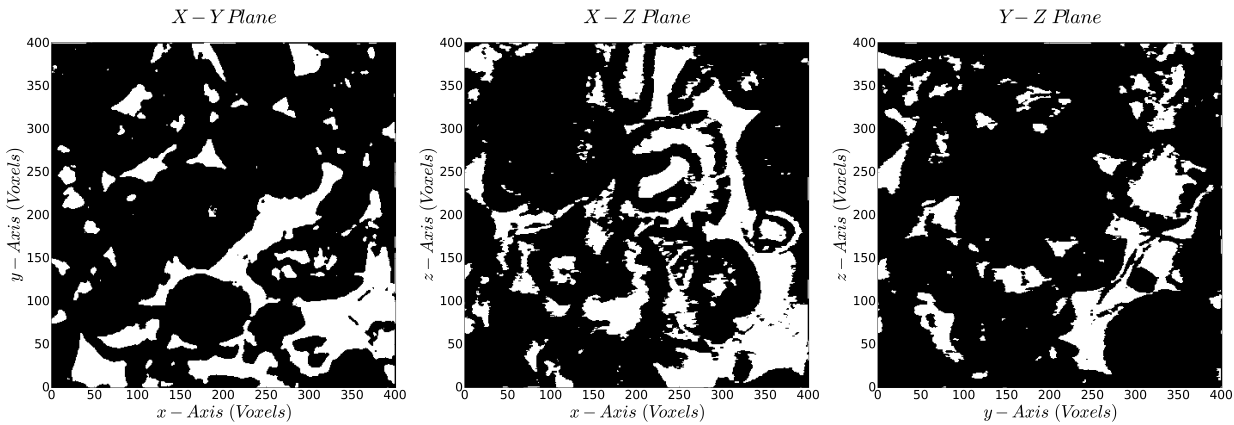


Appendix Figure 52: Stereonet projection of eigenvectors of Minkowski tensor $W_1^{0,2}$ of the S9 sample.

Results Summary		
Image Name	S9	
Rock Type	Sandstone	
Property	Value	Unit
Image Resolution	3.398	[μm]
Image Dimensions	(300, 300, 300)	(Nx, Ny, Nz) [voxel]
Covariance Analysis Results		
Porosity	0.22	[\cdot]
Directional Characteristic Pore Size [$r_{c,x}, r_{c,y}, r_{c,z}$]	60,53,55	[μm]
Average Characteristic Pore Size \bar{r}_c	52	[μm]
Specific Surface Area	13222	[m^{-1}]
Minkowski Tensor Analysis		
Normalized Minkowski Functional $\widehat{W}_1^{0,2}$	$\begin{bmatrix} 0.301 & -0.012 & -0.002 \\ -0.012 & 0.359 & 0.009 \\ -0.002 & 0.009 & 0.339 \end{bmatrix}$	[\cdot]
Normalized Minkowski Functional $\widehat{W}_2^{0,2}$	$\begin{bmatrix} 0.312 & -0.007 & -0.008 \\ -0.007 & 0.351 & 0.006 \\ -0.008 & 0.006 & 0.337 \end{bmatrix}$	[\cdot]
Anisotropy Index $\beta_1^{0,2}$	0.82	[\cdot]
Anisotropy Index $\beta_2^{0,2}$	0.87	[\cdot]
Permeability Computation Results		
Effective Porosity	0.22	[\cdot]
Directional Permeability	$\begin{bmatrix} 2.771 & - & - \\ - & 2.121 & - \\ - & - & 1.868 \end{bmatrix}$	[Darcy]

Sample 16: C1

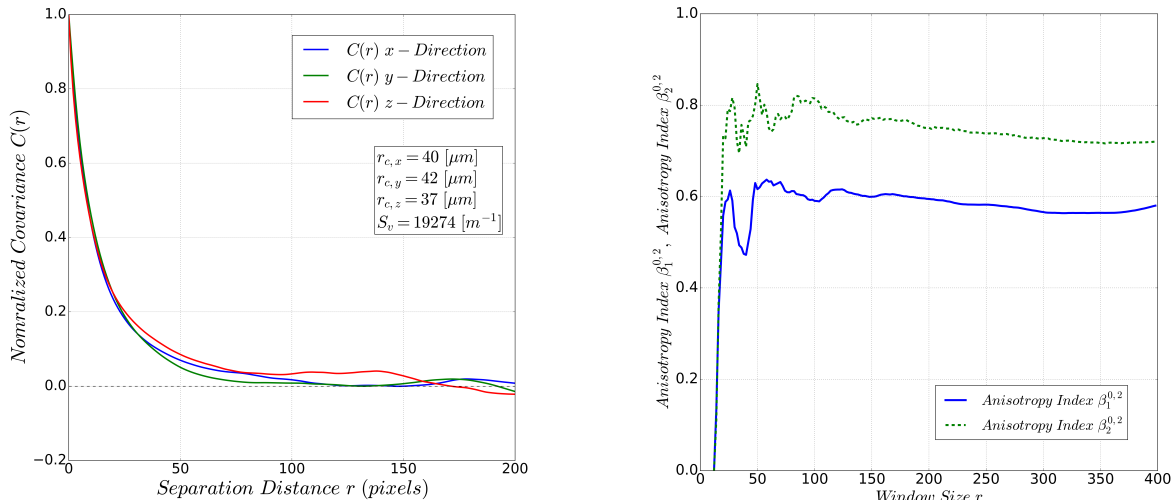
Orthogonal Image Projections:



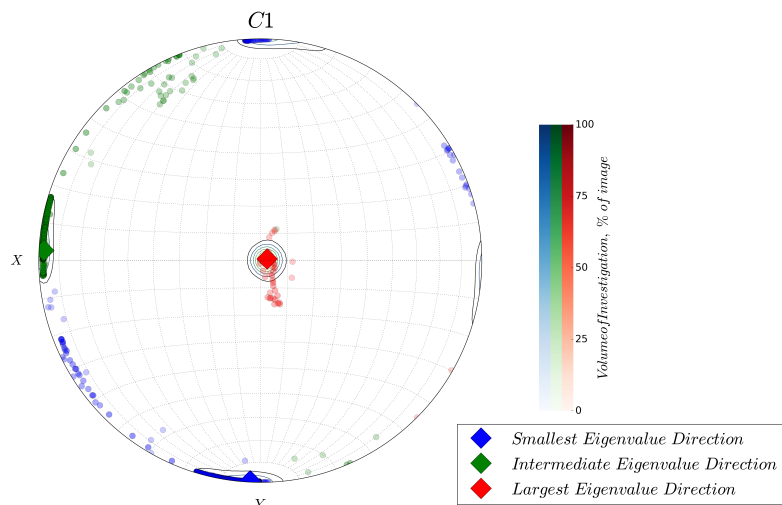
Appendix Figure 53: Orthogonal views of image C1. Views seen from front of sample.

Sample Analysis:

Sample C1 is a limestone sample showing significant inter and intra-granular porosity. Individual shells or molds are identifiable. Strong directional variation in characteristic pore size and no identifiable periodic fluctuations. No stabilization can be seen in the covariance or the anisotropy indices based on the Minkowski tensors. Eigenvector decomposition of Minkowski tensor $W_1^{0,2}$ shows axis aligned orientation distribution of pore-grain interface.



Appendix Figure 54 Left: Normalized directional covariance of the C1 sample. **Right:** Anisotropy indices derived from Minkowski tensor functionals.

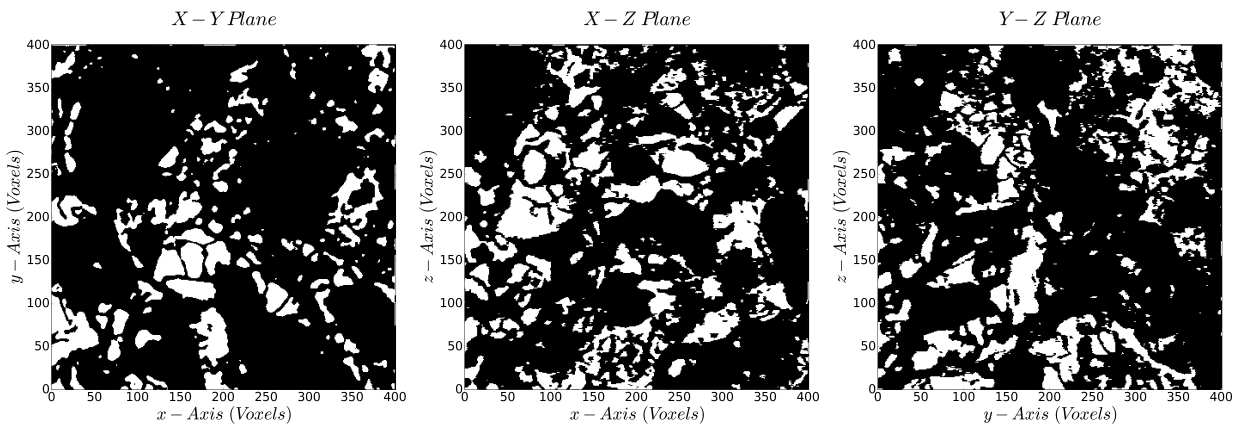


Appendix Figure 55: Stereonet projection of eigenvectors of Minkowski tensor $W_1^{0,2}$ of the C1 sample.

Results Summary		
Image Name	C1	
Rock Type	Carbonate	
Property	Value	Unit
Image Resolution	2.85	[μm]
Image Dimensions	(400, 400, 400)	(Nx, Ny, Nz) [voxel]
Covariance Analysis Results		
Porosity	0.23	[\cdot]
Directional Characteristic Pore Size [$r_{c,x}, r_{c,y}, r_{c,z}$]	40,42,37	[μm]
Average Characteristic Pore Size \bar{r}_c	37	[μm]
Specific Surface Area	19274	[m^{-1}]
Minkowski Tensor Analysis		
Normalized Minkowski Functional $\widehat{W}_1^{0,2}$	$\begin{bmatrix} 0.285 & 0 & -0.007 \\ 0 & 0.263 & 0.002 \\ -0.007 & 0.002 & 0.453 \end{bmatrix}$	[\cdot]
Normalized Minkowski Functional $\widehat{W}_2^{0,2}$	$\begin{bmatrix} 0.306 & 0 & 0 \\ 0 & 0.291 & 0 \\ 0 & 0 & 0.403 \end{bmatrix}$	[\cdot]
Anisotropy Index $\beta_1^{0,2}$	0.58	[\cdot]
Anisotropy Index $\beta_2^{0,2}$	0.72	[\cdot]
Permeability Computation Results		
Effective Porosity	0.23	[\cdot]
Directional Permeability	$\begin{bmatrix} 0.795 & - & - \\ - & 1.488 & - \\ - & - & 1.067 \end{bmatrix}$	[Darcy]

Sample 17: C2

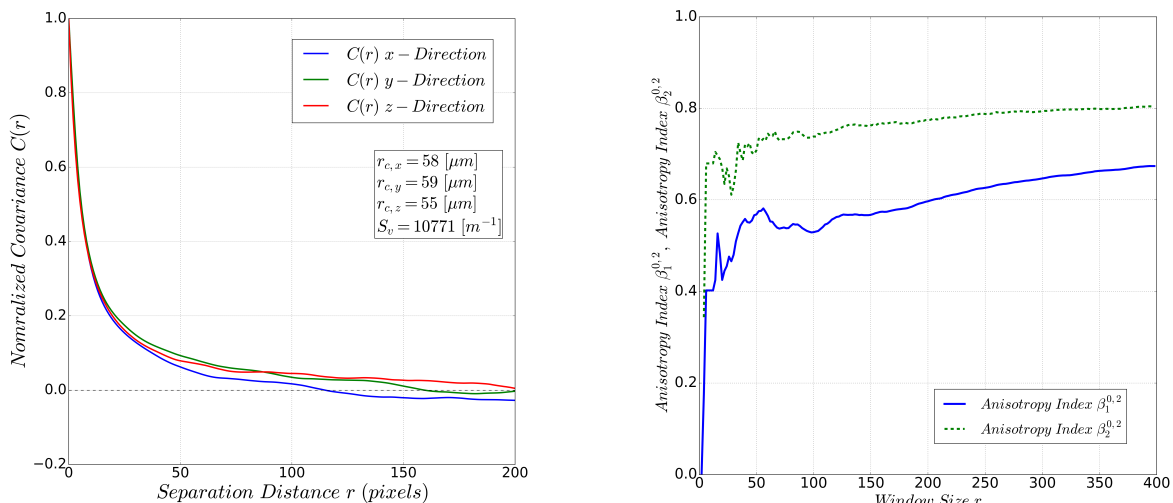
Orthogonal Image Projections:



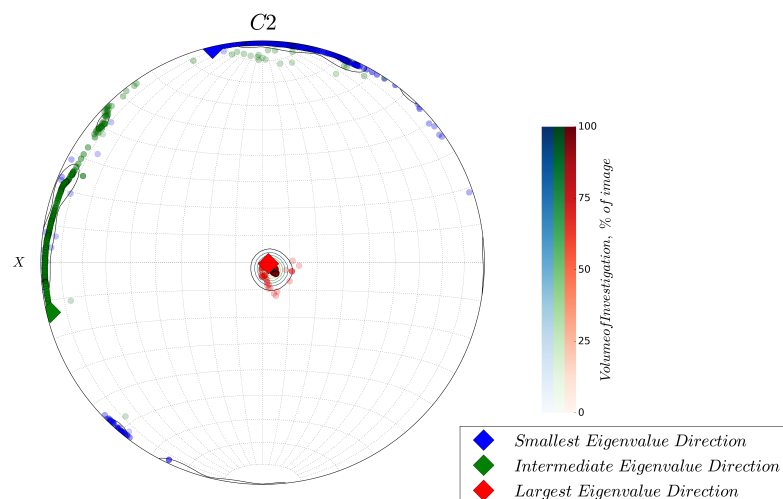
Appendix Figure 56: Orthogonal views of image C2. Views seen from front of sample.

Sample Analysis:

Complex carbonate pore structure with no clear grains or biogenic structures. The covariance shows no periodic fluctuations indicating that no individual grains are present in the material. Similar trends observed in the covariance in the three evaluated directions. Steep increase in anisotropy index indicates highly heterogeneous material that exhibits no intrinsic pore-grain interface anisotropy at the image scale. Low sample permeability that correlates well with covariance and Minkowski tensor evaluation.



Appendix Figure 57 Left: Normalized directional covariance of the C2 sample. **Right:** Anisotropy indices derived from Minkowski tensor functionals.

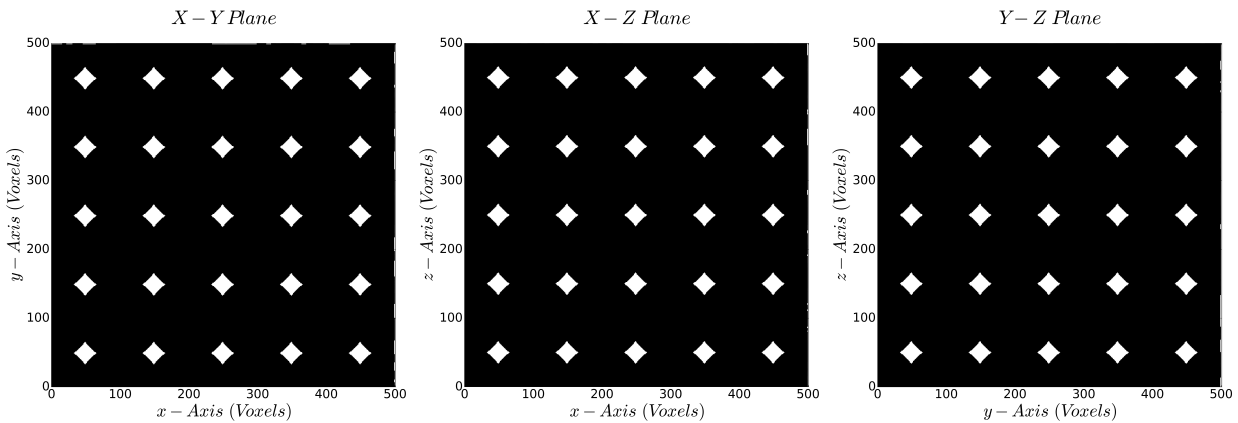


Appendix Figure 58: Stereonet projection of eigenvectors of Minkowski tensor $W_1^{0,2}$ of the C2 sample.

Results Summary		
Image Name	C2	
Rock Type	Carbonate	
Property	Value	Unit
Image Resolution	5.345	[μm]
Image Dimensions	(400, 400, 400)	(Nx, Ny, Nz) [voxel]
Covariance Analysis Results		
Porosity	0.17	[\cdot]
Directional Characteristic Pore Size [$r_{c,x}, r_{c,y}, r_{c,z}$]	58,59,55	[μm]
Average Characteristic Pore Size \bar{r}_c	52	[μm]
Specific Surface Area	10771	[m^{-1}]
Minkowski Tensor Analysis		
Normalized Minkowski Functional $\widehat{W}_1^{0,2}$	$\begin{bmatrix} 0.292 & 0.002 & -0.005 \\ 0.002 & 0.285 & 0.001 \\ -0.005 & 0.001 & 0.423 \end{bmatrix}$	[\cdot]
Normalized Minkowski Functional $\widehat{W}_2^{0,2}$	$\begin{bmatrix} 0.311 & 0 & -0.003 \\ 0 & 0.308 & 0 \\ -0.003 & 0 & 0.382 \end{bmatrix}$	[\cdot]
Anisotropy Index $\beta_1^{0,2}$	0.67	[\cdot]
Anisotropy Index $\beta_2^{0,2}$	0.80	[\cdot]
Permeability Computation Results		
Effective Porosity	0.168	[\cdot]
Directional Permeability	$\begin{bmatrix} 0.039 & - & - \\ - & 0.163 & - \\ - & - & 0.018 \end{bmatrix}$	[Darcy]

Sample 18: Isotropic $r_{1,2,3} = 1.2$

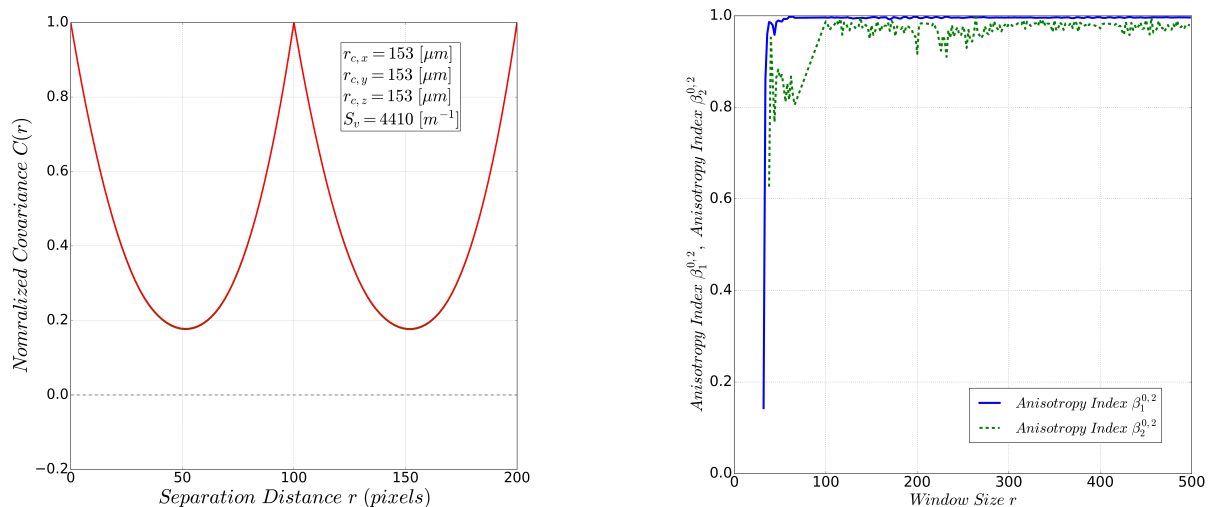
Orthogonal Image Projections:



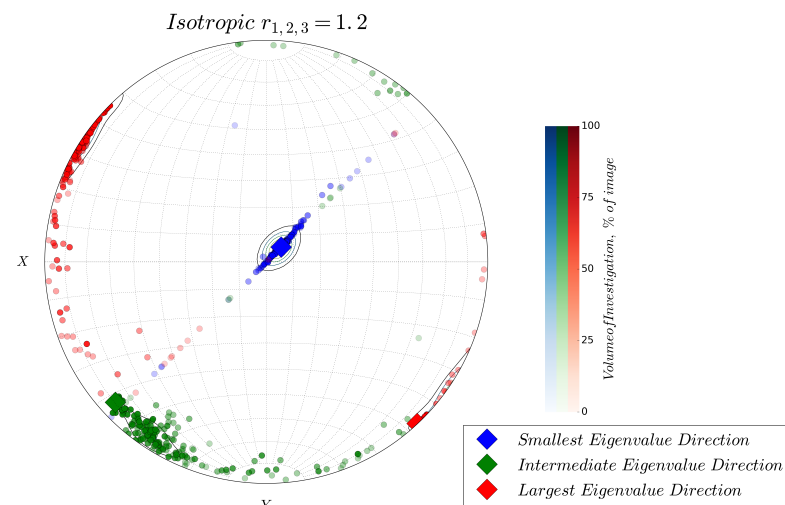
Appendix Figure 59: Orthogonal views of image Isotropic $r_{1,2,3} = 1.2$. Views seen from front of sample.

Sample Analysis:

A parametric model consisting of isotropic spherical grains. The covariance shows a periodic shape with maxima reached at the average separation distance of the grains. Minkowski tensor anisotropy index shows purely isotropic behavior from very small sample size onwards. Numerical permeability shows isotropic behavior and is in good agreement with evaluated measures.



Appendix Figure 60: Left: Normalized directional covariance of the Isotropic $r_{1,2,3} = 1.2$ parametric model. Right: Anisotropy indices derived from Minkowski tensor functionals.

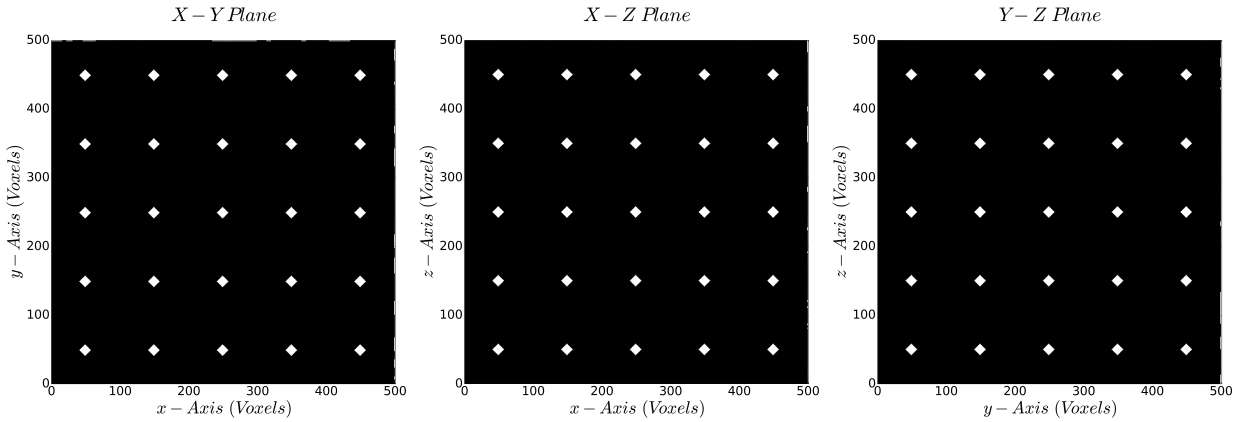


Appendix Figure 61: Stereonet projection of eigenvectors of Minkowski tensor $W_1^{0,2}$ of the Isotropic $r_{1,2,3} = 1.2$ parametric model.

Results Summary		
Image Name	Isotropic $r_{1,2,3} = 1.2$	
Rock Type	Parametric	
Property	Value	Unit
Image Resolution	2.0	[μm]
Image Dimensions	(500, 500, 500)	(Nx, Ny, Nz) [voxel]
Covariance Analysis Results		
Porosity	0.21	[\cdot]
Directional Characteristic Pore Size $[r_{c,x}, r_{c,y}, r_{c,z}]$	153,153,153	[μm]
Average Characteristic Pore Size \bar{r}_c	153	[μm]
Specific Surface Area	4410	[m^{-1}]
Minkowski Tensor Analysis		
Normalized Minkowski Functional $\widehat{W}_1^{0,2}$	$\begin{bmatrix} 0.333 & 0 & 0 \\ 0 & 0.333 & 0 \\ 0 & 0 & 0.333 \end{bmatrix}$	[\cdot]
Normalized Minkowski Functional $\widehat{W}_2^{0,2}$	$\begin{bmatrix} 0.333 & -0.003 & -0.002 \\ -0.003 & 0.333 & -0.002 \\ -0.002 & -0.002 & 0.333 \end{bmatrix}$	[\cdot]
Anisotropy Index $\beta_1^{0,2}$	1.0	[\cdot]
Anisotropy Index $\beta_2^{0,2}$	0.98	[\cdot]
Permeability Computation Results		
Effective Porosity	0.21	[\cdot]
Directional Permeability	$\begin{bmatrix} 8.621 & - & - \\ - & 8.618 & - \\ - & - & 8.623 \end{bmatrix}$	[Darcy]

Sample 19: Isotropic $r_{1,2,3} = 1.3$

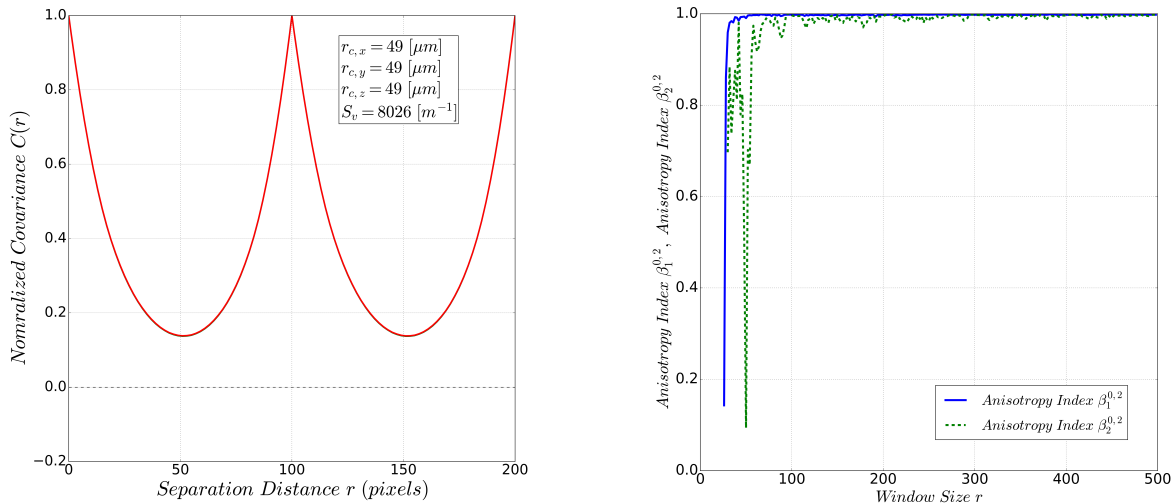
Orthogonal Image Projections:



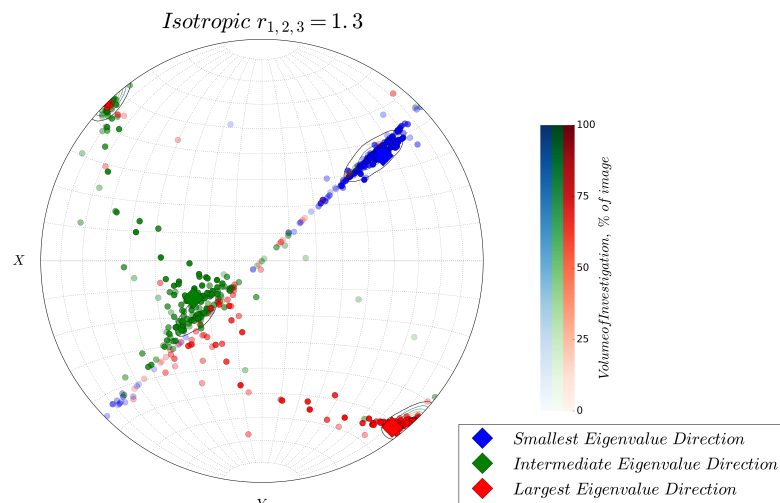
Appendix Figure 62: Orthogonal views of image Isotropic $r_{1,2,3} = 1.3$. Views seen from front of sample.

Sample Analysis:

A parametric model consisting of isotropic spherical grains. The covariance shows a periodic shape with maxima reached at the average separation distance of grains. The Minkowski tensor anisotropy index shows purely isotropic behavior from very small sample size onwards. Numerical permeability shows isotropic behavior and is in good agreement with evaluated measures.



Appendix Figure 63 Left: Normalized directional covariance of the Isotropic $r_{1,2,3} = 1.3$ sample. Right: Anisotropy indices derived from Minkowski tensor functionals.

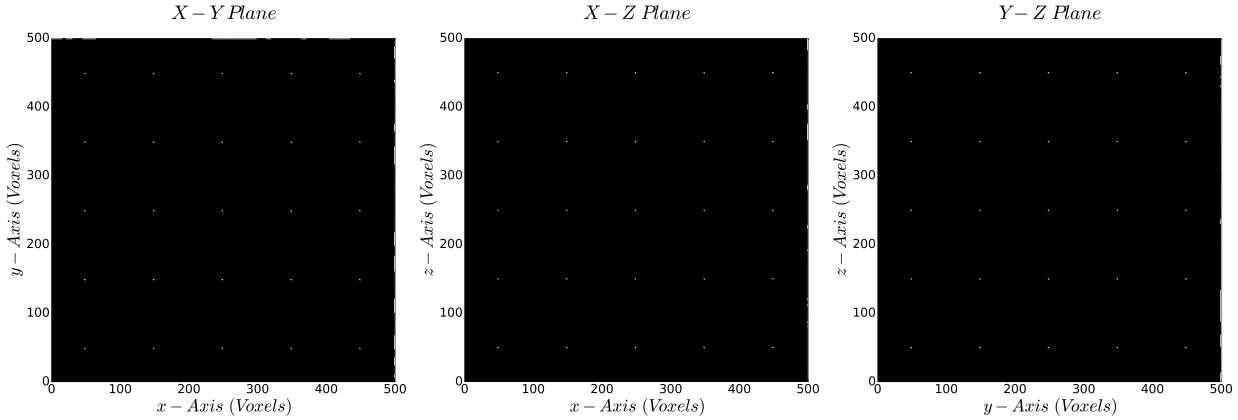


Appendix Figure 64: Stereonet projection of eigenvectors of Minkowski tensor $W_1^{0,2}$ of the sample Isotropic $r_{1,2,3} = 1.3$.

Results Summary		
Image Name	Isotropic $r_{1,2,3} = 1.3$	
Rock Type	Parametric	
Property	Value	Unit
Image Resolution	2.0	[μm]
Image Dimensions	(500, 500, 500)	(Nx, Ny, Nz) [voxel]
Covariance Analysis Results		
Porosity	0.11	[\cdot]
Directional Characteristic Pore Size $[r_{c,x}, r_{c,y}, r_{c,z}]$	49,49,49	[μm]
Average Characteristic Pore Size \bar{r}_c	49	[μm]
Specific Surface Area	8026	[m^{-1}]
Minkowski Tensor Analysis		
Normalized Minkowski Functional $\widehat{W}_1^{0,2}$	$\begin{bmatrix} 0.333 & 0 & 0 \\ 0 & 0.333 & 0 \\ 0 & 0 & 0.333 \end{bmatrix}$	[\cdot]
Normalized Minkowski Functional $\widehat{W}_2^{0,2}$	$\begin{bmatrix} 0.333 & 0 & 0 \\ 0 & 0.333 & 0 \\ 0 & 0 & 0.333 \end{bmatrix}$	[\cdot]
Anisotropy Index $\beta_1^{0,2}$	1.0	[\cdot]
Anisotropy Index $\beta_2^{0,2}$	1.0	[\cdot]
Permeability Computation Results		
Effective Porosity	0.11	[\cdot]
Directional Permeability	$\begin{bmatrix} 0.931 & - & - \\ - & 0.932 & - \\ - & - & 0.944 \end{bmatrix}$	[Darcy]

Sample 20: Isotropic $r_{1,2,3} = 1.4$

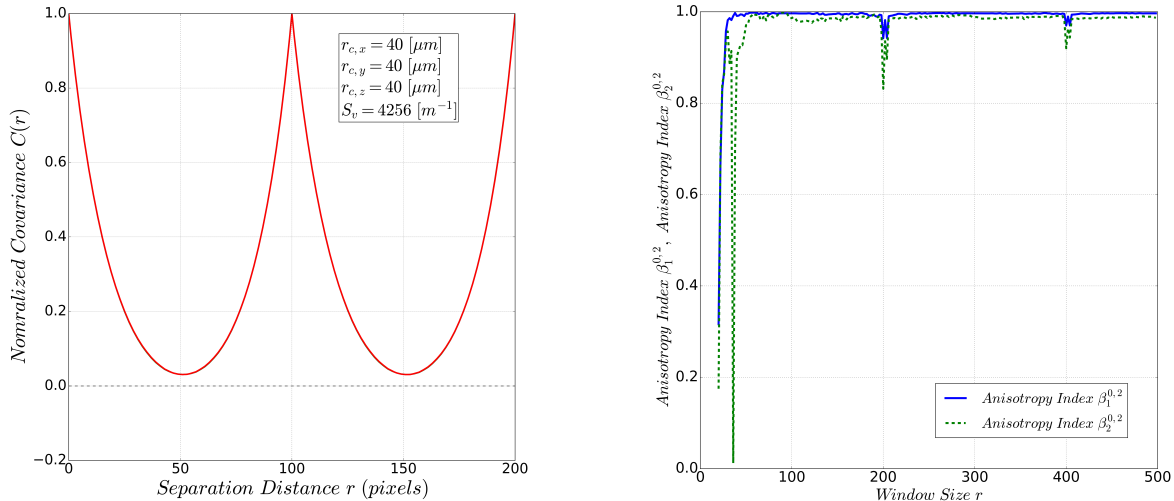
Orthogonal Image Projections:



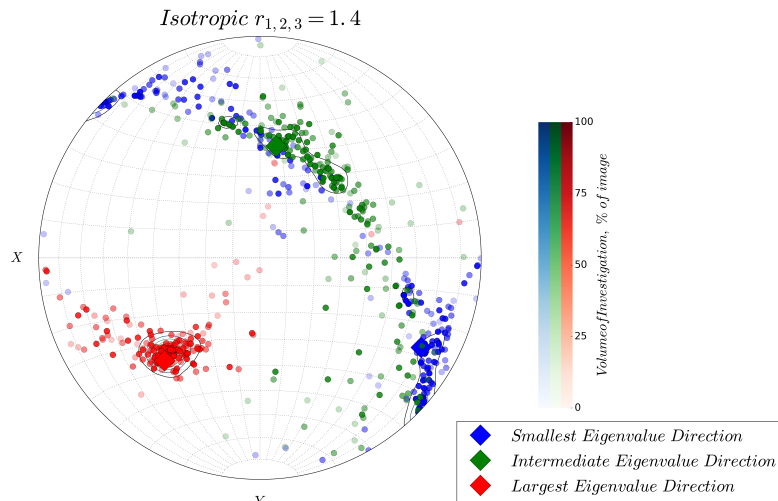
Appendix Figure 65: Orthogonal views of image Isotropic $r_{1,2,3} = 1.4$. Views seen from front of sample.

Sample Analysis:

A parametric model consisting of isotropic spherical grains. The covariance shows periodic shape with maxima reached at the average separation distance of grains. The Minkowski tensor anisotropy index shows purely isotropic behavior from very small sample size onwards. Small fluctuations at 200 and 400 voxels can be attributed mesh dependency effects due to the discrete mesh extraction algorithms. Numerical permeability shows isotropic behavior and is in good agreement with evaluated measures.

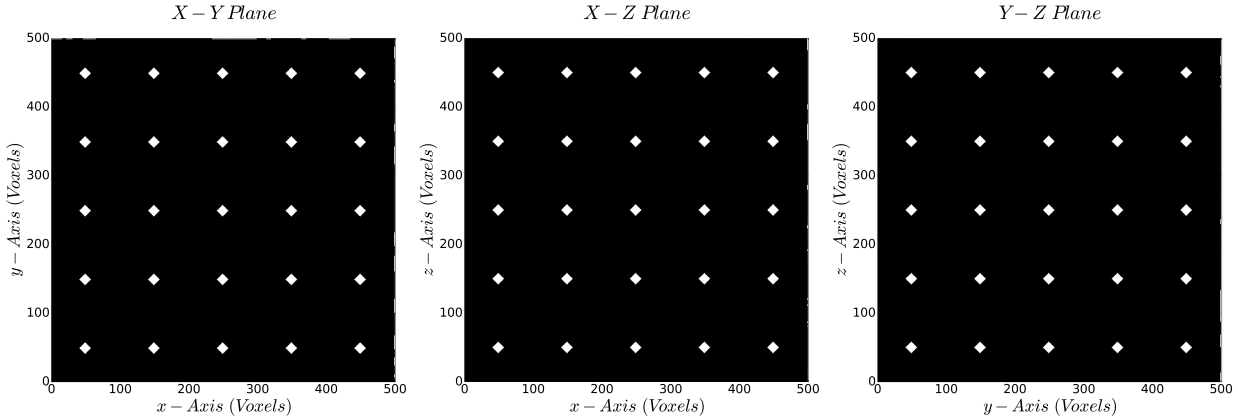


Appendix Figure 66: Left: Normalized directional Covariance of the sample Isotropic $r_{1,2,3} = 1.4$. Right: Anisotropy indices derived from Minkowski tensor functionals.

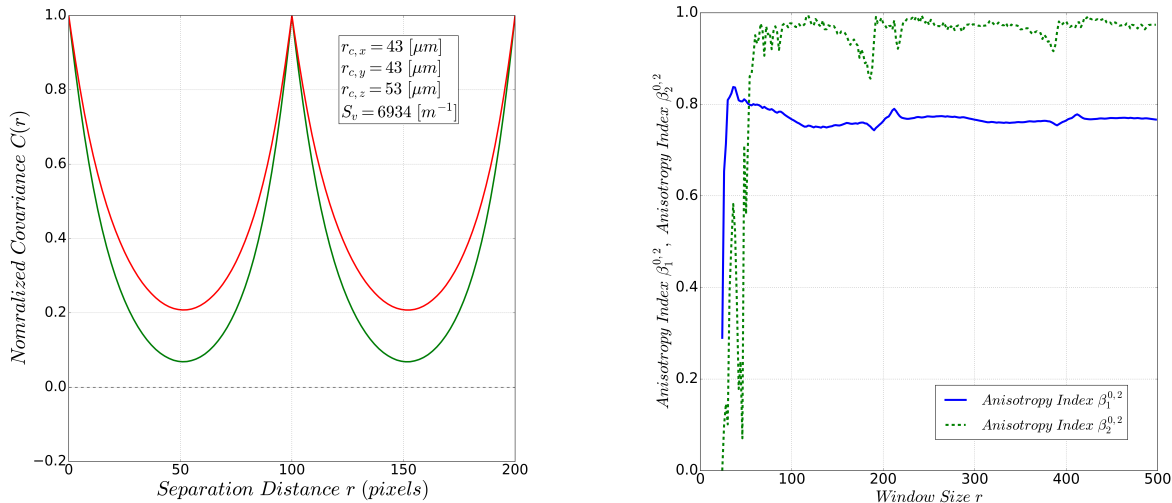
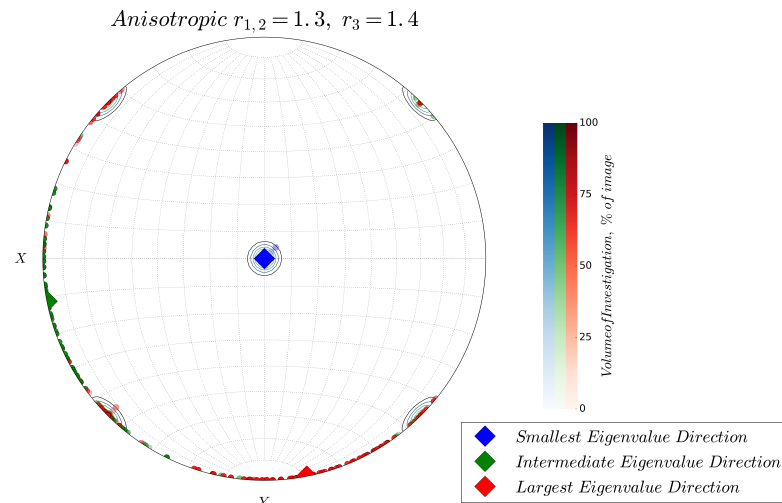


Appendix Figure 67: Stereonet projection of eigenvectors of Minkowski tensor $W_1^{0,2}$ of the sample Isotropic $r_{1,2,3} = 1.4$.

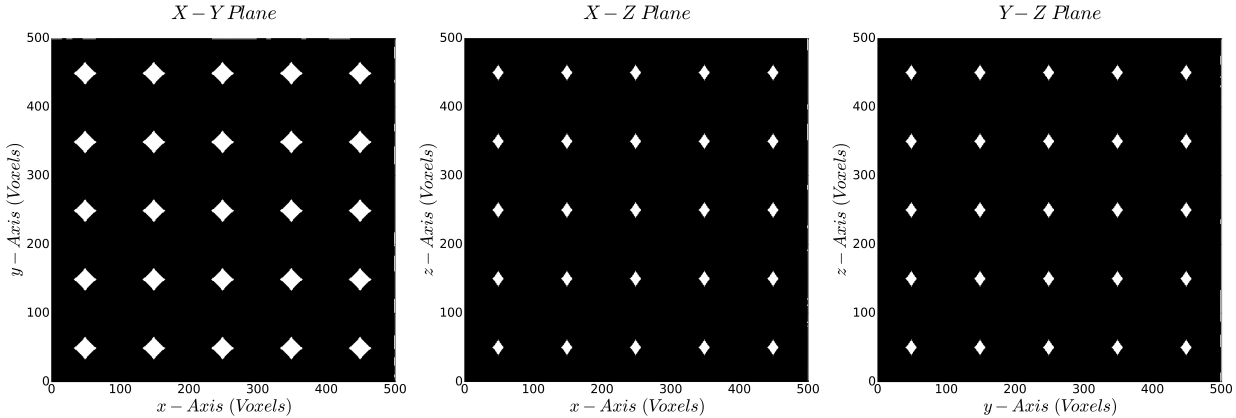
Results Summary		
Image Name	Isotropic $r_{1,2,3} = 1.4$	
Rock Type	Parametric	
Property	Value	Unit
Image Resolution	2.0	[μm]
Image Dimensions	(500, 500, 500)	(Nx, Ny, Nz) [voxel]
Covariance Analysis Results		
Porosity	0.04	[\cdot]
Directional Characteristic Pore Size $[r_{c,x}, r_{c,y}, r_{c,z}]$	40,40,40	[μm]
Average Characteristic Pore Size \bar{r}_c	40	[μm]
Specific Surface Area	4256	[m^{-1}]
Minkowski Tensor Analysis		
Normalized Minkowski Functional $\widehat{W}_1^{0,2}$	$\begin{bmatrix} 0.332 & 0 & 0 \\ 0 & 0.333 & 0 \\ 0 & 0 & 0.333 \end{bmatrix}$	[\cdot]
Normalized Minkowski Functional $\widehat{W}_2^{0,2}$	$\begin{bmatrix} 0.332 & 0 & 0 \\ 0 & 0.332 & 0 \\ 0 & 0 & 0.336 \end{bmatrix}$	[\cdot]
Anisotropy Index $\beta_1^{0,2}$	0.99	[\cdot]
Anisotropy Index $\beta_2^{0,2}$	0.98	[\cdot]
Permeability Computation Results		
Effective Porosity	0.042	[\cdot]
Directional Permeability	$\begin{bmatrix} 0.303 & - & - \\ - & 0.303 & - \\ - & - & 0.303 \end{bmatrix}$	[mD]

Sample 21: Anisotropic $r_{1,2} = 1.3$ $r_3 = 1.4$
Orthogonal Image Projections:

Appendix Figure 68: Orthogonal views of image Anisotropic $r_{1,2} = 1.3$, $r_3 = 1.4$. Views seen from front of sample.
Sample Analysis:

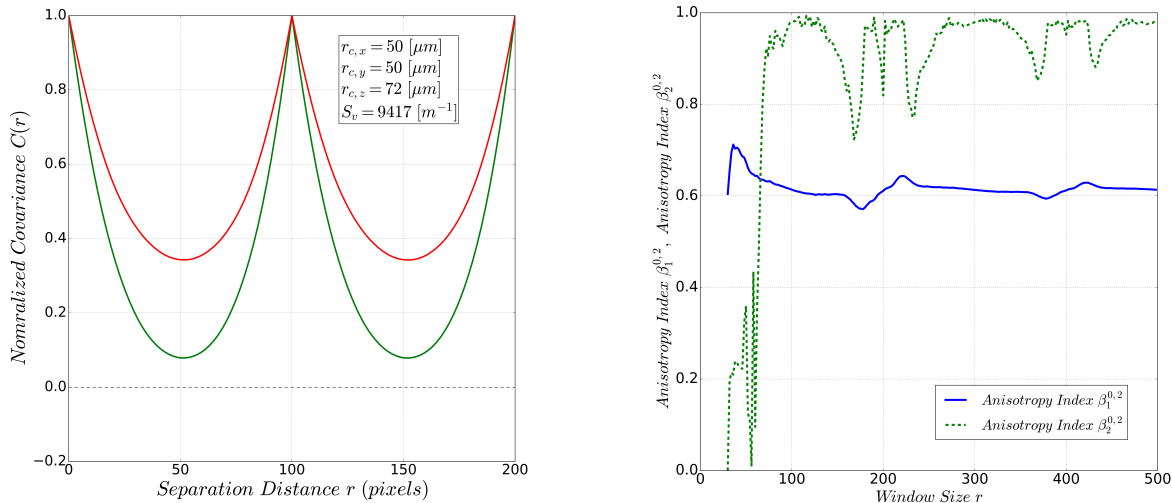
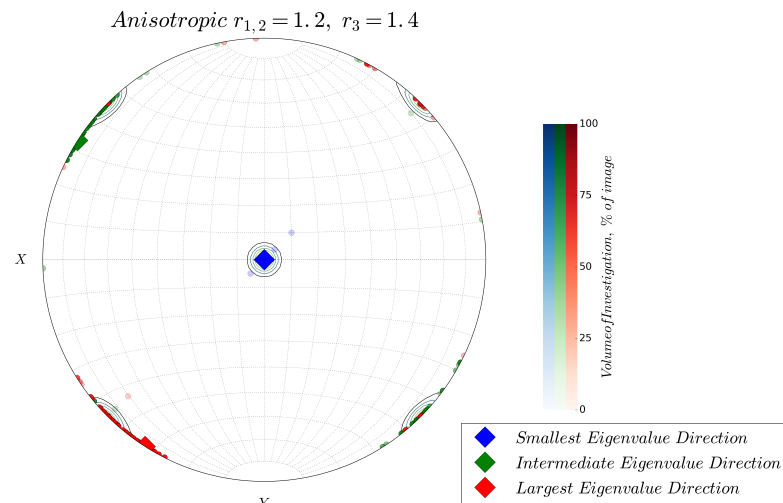
Parametric model of ellipsoidal grains with reduced diameter in the x-y plane. The covariance indicates a larger characteristic pore size in the z-direction which is in good agreement with the model. Reduced diameters in one plane will lead to increased pore size orthogonal to this plane. Numerical permeability estimates correlate with the anisotropy indicated by the covariance and anisotropy indices.


Appendix Figure 69: Left: Normalized directional covariance of the sample Anisotropic $r_{1,2} = 1.3$, $r_3 = 1.4$. Right: Anisotropy indices derived from Minkowski tensor functionals.

Appendix Figure 70: Stereonet projection of eigenvectors of Minkowski tensor $W_1^{0,2}$ of the sample Anisotropic $r_{1,2} = 1.3$, $r_3 = 1.4$.

Results Summary		
Image Name	Anisotropic $r_{1,2} = 1.3, r_3 = 1.4$	
Rock Type	Parametric	
Property	Value	Unit
Image Resolution	2.0	[μm]
Image Dimensions	(500, 500, 500)	(Nx, Ny, Nz) [voxel]
Covariance Analysis Results		
Porosity	0.08	[\cdot]
Directional Characteristic Pore Size $[r_{c,x}, r_{c,y}, r_{c,z}]$	43,43,53	[μm]
Average Characteristic Pore Size \bar{r}_c	44	[μm]
Specific Surface Area	6934	[m^{-1}]
Minkowski Tensor Analysis		
Normalized Minkowski Functional $\widehat{W}_1^{0,2}$	$\begin{bmatrix} 0.361 & 0 & 0 \\ 0 & 0.361 & 0 \\ 0 & 0 & 0.277 \end{bmatrix}$	[\cdot]
Normalized Minkowski Functional $\widehat{W}_2^{0,2}$	$\begin{bmatrix} 0.336 & 0 & 0 \\ 0 & 0.336 & 0 \\ 0 & 0 & 0.328 \end{bmatrix}$	[\cdot]
Anisotropy Index $\beta_1^{0,2}$	0.77	[\cdot]
Anisotropy Index $\beta_2^{0,2}$	0.97	[\cdot]
Permeability Computation Results		
Effective Porosity	0.08	[\cdot]
Directional Permeability	$\begin{bmatrix} 0.130 & - & - \\ - & 0.130 & - \\ - & - & 0.876 \end{bmatrix}$	[Darcy]

Sample 22: Anisotropic $r_{1,2} = 1.2$ $r_3 = 1.4$
Orthogonal Image Projections:

Appendix Figure 71: Orthogonal views of image Anisotropic $r_{1,2} = 1.2$, $r_3 = 1.4$. Views seen from front of sample.
Sample Analysis:

Parametric model of ellipsoidal grains with reduced diameter in the x-y plane. The covariance indicates a larger characteristic pore size in the z-direction which is in good agreement with the model. Reduced diameters in one plane will lead to increased pore size orthogonal to this plane. Numerical permeability estimates correlate with the anisotropy indicated by the covariance and anisotropy indices.


Appendix Figure 72: Left: Normalized directional covariance of the sample Anisotropic $r_{1,2} = 1.2$, $r_3 = 1.4$. Right: Anisotropy indices derived from Minkowski tensor functionals.

Appendix Figure 73: Stereonet projection of eigenvectors of Minkowski tensor $W_1^{0,2}$ of the sample Anisotropic $r_{1,2} = 1.2$, $r_3 = 1.4$.

Results Summary		
Image Name	Anisotropic $r_{1,2} = 1.2$ $r_3 = 1.4$	
Rock Type	Parametric	
Property	Value	Unit
Image Resolution	2.0	[μm]
Image Dimensions	(500, 500, 500)	(Nx, Ny, Nz) [voxel]
Covariance Analysis Results		
Porosity	0.15	[\cdot]
Directional Characteristic Pore Size $[r_{c,x}, r_{c,y}, r_{c,z}]$	50,50,72	[μm]
Average Characteristic Pore Size \bar{r}_c	53	[μm]
Specific Surface Area	9417	[m^{-1}]
Minkowski Tensor Analysis		
Normalized Minkowski Functional $\widehat{W}_1^{0,2}$	$\begin{bmatrix} 0.383 & 0 & 0 \\ 0 & 0.383 & 0 \\ 0 & 0 & 0.235 \end{bmatrix}$	[\cdot]
Normalized Minkowski Functional $\widehat{W}_2^{0,2}$	$\begin{bmatrix} 0.335 & 0 & 0.002 \\ 0 & 0.334 & 0.002 \\ 0.002 & 0.002 & 0.331 \end{bmatrix}$	[\cdot]
Anisotropy Index $\beta_1^{0,2}$	0.61	[\cdot]
Anisotropy Index $\beta_2^{0,2}$	0.98	[\cdot]
Permeability Computation Results		
Effective Porosity	0.15	[\cdot]
Directional Permeability	$\begin{bmatrix} 1.3645 & - & - \\ - & 1.369 & - \\ - & - & 7.557 \end{bmatrix}$	[Darcy]